Fundamentals of Spectroscopic and Spectrometric Cellular Analysis

A thesis submitted to The University of Manchester for the degree of Doctor of Philosophy in the Faculty of Engineering and Physical Sciences

2011

Edward R J Jackson

School of Chemical Engineering and Analytical Science

Contents

Final word count: 31415

Abbreviations

AILES	Advanced Infrared Line Exploited for Spectroscopy
BPH	Benign Prostatic Hyperplasia
CDK	Cyclin Dependent Kinase
DFA	Discriminant Function Analysis
DMEM	Dulbecco's Modified Eagle's Medium
DPBS	Dulbecco's Phosphate Buffered Saline
DNA	Deoxyribonucleic Acid
EDTA	Ethylenediaminetetraacetic acid
EMSC	Extended Multiplicative Signal Correction
FACS	Fluorescence Activated Cell Sorting
FCS	Foetal Calf Serum
FTIR	Fourier Transformed Infrared spectroscopy
HPLC	High Performance Liquid Chromatography
KeV	Kiloelectron Volt
LMIG	Liquid Metal Ion Gun
MALDI	Matrix assisted Laser Desorption Ionisation
PBS	Phosphate Buffered Solution
PCA	Principal Component Analysis
PIN	Prostatic Intraepithelial Hyperplasia
PSA	Prostate Specific Antigen
RMieS	Resonant Mie Scattering
RNA	Ribonucleic Acid
RPMI	Roswell Park Memorial Institute (culture media)
SEM	Scanning Electron Microscopy
SISSI	Source for Imaging and Spectroscopic Studies
SMIS	Spectroscopy and Microscopy in the Infrared region using Synchrotron Radiation
TNM	Tumour Node Metastasis
ToF-SIMS	Time of Flight Secondary Ion Mass Spectrometry
WHO	World Health Organisation

The University of Manchester
Faculty of Engineering and Physical Sciences

ABSTRACT OF THESIS submitted by Edward Robert James Jackson
For the degree of Doctor of Philosophy
and entitled Fundamentals of Spectroscopic and Spectrometric Cellular Analysis

Date of submission 24/01/2011

Time-of-flight secondary ion mass spectrometry (ToF-SIMS) in principle has the capability to detect and localise complex chemistry on the sub-cellular scale. Robust sample preparation protocols are therefore of great importance when attempting to preserve the natural biochemistry and architecture of biological specimens and extract meaningful information. It is likely that the optimum methodology will depend on the nature of the sample, and the goal of the analysis. The following study focussed on the preparation of cancer cells for ToF-SIMS analysis. Air drying, freeze fracturing, freeze drying and cytospinning-based preparation techniques and variations thereof were evaluated. Using image contrast, assessing spectra for the gain, or loss of native and non-native cellular species and the ratio of inorganic to organic ion yields, the investigation provides a systematic evaluation of the features of each preparation technique. This study then employed the optimum methods to determine the influence of the various phases of the cell cycle on classification of ToF-SIMS spectral data. A number of cell types, both cancerous and non-cancerous in G1, S and G2/M growth phases are separated by anticancer drug treatment and FACS (fluorescence activated cell sorting) and subjected to ToF-SIMS analysis. The results indicate that ToF-SIMS can detect surface biochemical changes induced by the cell cycle. Importantly it is also capable of detecting subtle alterations in cellular chemistry caused by anticancer drugs. Furthermore, the ToF-SIMS data was compared to results obtained from synchrotron sourced FTIR microspectroscopy to provide a more robust complementary analysis and support chemical evidence gathered.

Declaration

No portion of the work referred to in this thesis has been submitted in support of an application for another degree or qualification of this or any other university or other institute of learning.

Copyright Statement

Acknowledgements

I would like to thank Dr Nicholas Lockyer and Dr Peter Gardner for their excellent support and supervision. I am particularly grateful for the opportunities I was given to travel and work abroad during my studies. I would also like to thank Professor John Vickerman for giving me the opportunity to present my work at an international conference and the EPSRC for funding my PhD.

I would like to thank the other members of the SARC and Gardner groups for their help and guidance, the Paterson Institute for cancer research and Salford University.

Finally, I would like to thank Teresa and Konrad for their amazing friendship and personal support that helped me through the toughest parts of my PhD.

Chapter 1: Introduction

The following thesis follows a discovery based, holistic approach to examine the development of chemically based methods to understand and characterise cancer and chemotherapeutic agents at a cellular level.

The succeeding chapter introduces theory relevant to the investigation. Cancer and cell biology will be introduced; spectrometric and spectroscopic concepts will be discussed; and, finally, statistical methods explained.

1.1 Cancer

Cancer, today, still remains one of the most feared causes of death. After cardiovascular disease, a mortality rate of about 12.4 million cases per year makes cancer a leading cause of death worldwide (figure 1.1) [1]. Out of those deaths, lung cancer was the most common cancer in men and breast in women [1]. The following will discuss, broadly, cancer epidemiology and aetiology; tumour nomenclature, detection, diagnosis and prognosis; and, finally, model cell lines and cell biology will be introduced.

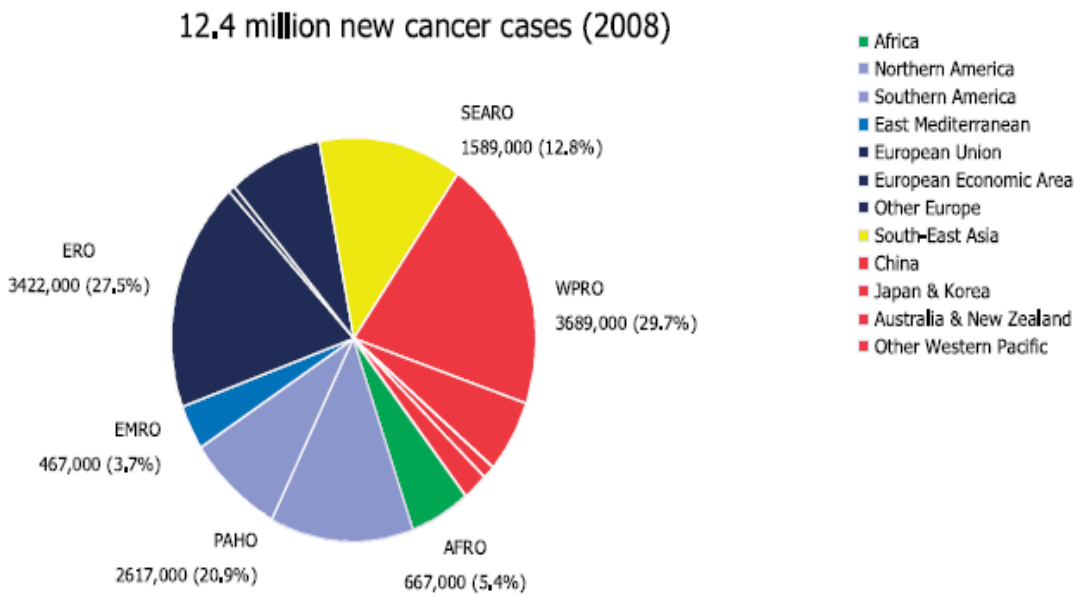

Figure 1.1. Distribution of Global Cancer burden by World Health Organisation Region. Reproduced from [1]

1.1.1 Cancer epidemiology

Several forms of cancer vary significantly in incidence, prevalence and mortality rate between populations (figure 1.1) [2,3]. It seems that every form of cancer is rare in some location and the incidence of cancer in immigrants from these areas soon meets the level of the host population [4]. This observation lead cancer epidemiologists to believe most forms of the disease are, in principle, preventable. This trend ruled out genetic explanations for the global differences in cancer incidence and brought forward ideas relating to lifestyle choice and the environment [2]. The following will introduce some of the factors commonly addressed by cancer epidemiologists, a more exhaustive list of discussions is provided elsewhere by the International Agency for Research on Cancer (IARC) [1].

1.1.1.1 Carcinogenic effects of tobacco

The carcinogenic effect of tobacco was probably the most noteworthy discovery in the history of cancer epidemiology [2]. The risk of cancer increases significantly with smoking, including cancer of the lung, oral cavity, nasal cavity and nasal sinuses, pharynx, larynx, oesophagus, stomach, pancreas, liver, urinary bladder, kidney and uterine cervix, and myeloid leukaemia [1]. Furthermore, the incidence of lung cancer increases rapidly among those who are frequently exposed to second hand smoke - often termed as “passive smoking” [1]. Recent estimates suggest the incidence of smoking related cancers to be higher in more affluent regions as the consumption of cigarettes started earlier in these places. Similarly, the incidence of smoking related cancers in males is greater than in females as women began to smoke several years after men [1]. Interestingly, the detrimental effects of smoking have different consequences between populations [2]. For example, in China, smoking leads to more deaths from liver cancer than cardiovascular disease [5].

Despite recent changes in the composition of cigarettes, tobacco smoke still remains the most common source of carcinogens in humans [1]. Out of the 4800 compounds found in cigarette smoke, 69 are thought to be carcinogenic [6]. The

most harmful agents are carbon monoxide, nicotine, nitrogen oxides, nitrosamines, hydrogen cyanide, volatile aldehydes, aromatic hydrocarbons and alkenes. Of these, aromatic hydrocarbons and nitrosamines are the most destructive.

Smokeless tobacco products such as chewing tobacco or snuff are – despite the lack of burning – also carcinogenic. Smokeless tobacco is used widely in Asia, Africa, Northern America and Nordic European Countries [1]. There are over 30 carcinogens in smokeless tobacco including similar compounds to tobacco smoke [1]. Furthermore, smokeless tobacco use exposes the person to the highest human exposure to nitrosamines [1].

Continued exposure to the carcinogenic compounds in tobacco can lead to DNA damage and disrupt mechanisms involved with cellular repair, which eventually leads to cancer [1,6].

1.1.1.2 Diet and obesity

The large number of foods and their many ingredients presents a complex problem for dietary epidemiologists [2]. Nevertheless, epidemiological observations have successfully identified nutritional deficiencies responsible for diseases such as pellagra, blindness, scurvy and spina bifida [7]. Such strong associations have yet to be made with cancer due to the complexity of the disease and, frequently, conflicting information [2,7]. For example, the daily intake of calcium has been marked as an important factor in reducing the probability of colon cancer in prone individuals [7]. Contrastingly, however, it has also been found that too much dietary calcium (>600mg/day) can increase the risk of prostate cancer [8]. It is believed that Calcium is involved in the regulation of vitamin D synthesis, more specifically, the down-regulation of the anti-proliferative effects of the vitamin [8]. As with many dietary factors, difficulties in quantifying calcium intake have compounded investigations. It is therefore, unclear how serious such investigations can be taken [7,8,9]. Similar problems have lead to the rise and fall in popularity of many “anticancer”

compounds, such as beta-carotene and folate [7]. It is important to note the efficacy of these compounds probably also depends on the synergistic influence of other natural components of the food [7]. Thus far, no single compound contained within food shows a strong, reliable association with the prevention, or induction of cancer [2,7].

As a general rule, western diets can be linked to higher risks of cancers, such as prostate and colon cancer [8]. The higher intake of fats, processed meats and red meats that characterizes the western diet is thought to be largely responsible [8]. In particular, the methods, by which, the food is prepared and cooked, may be important for the disease. For example, high temperature cooking methods, such as charcoal grilling and frying, can produce potent mutagenic heterocyclic amines [9].

More recently, links have been found between obesity and cancer. The world cancer report produced by the IARC suggests that obesity is contributing "significantly" to increasing cancer incidences [1]. It is believed that approximately 5% of all cancers in Europe are caused by obesity and could possibly be prevented if levels were reduced [2].

1.1.1.3 Viruses, parasites and bacteria

Another important advance in cancer epidemiology characterized pathogens capable of inducing carcinogenesis [2]. For example, DNA from a certain phylogenetic subgroup of human papillomaviruses (HPVs) has been detected in around 99.7% of cervical cancers [10]. This suggests the link between HPV and cervical cancer is the strongest ever reported for a specific cause of cancer, which could be greatly reduced by vaccination [10].

Other pathogens responsible for increasing the risk of cancer include *Helicobacter pylori*, a bacterium that can cause stomach cancer; the hepatitis-C virus (HCV), linked with liver cancer; and, many others [1,2].

1.1.1.4 Hormones and growth factors

It is clear that androgens play a pivotal role in the development and maintenance of both male and female reproductive organs and in the treatment of the relevant cancers. For example, surgical or medical castration has proven as an effective means of treating patients with metastatic prostate cancer [8]. This is probably due to the fact that the prostate is necessary for the conversion of testosterone to dihydrotestosterone, both of which have been linked to the induction of prostate cancer in rats [8,9]. As briefly mentioned previously, vitamin D – another steroid hormone – has potent antiproliferative, pro-apoptotic, and pro-differentiative effects on prostate cancer cells [9]. Synthesised primarily in response to dermal sunlight exposure, vitamin D is also believed to have chemopreventative effects and inhibit tumour growth [9].

Steroid hormones are known to modulate the production and biological action of growth factors [11]. It is not surprising therefore, that insulin-like growth factors (IGFs) have been associated with prostate cancer. These polypeptides are intimately involved with cancer cell proliferation, differentiation, and apoptosis [8]. It is thought that IGFs may be an important link between the western lifestyle and a higher incidence of prostate cancer [8]. Essentially, the consumption of large amounts of fats stimulates the production of excessive IGF, thus providing the conditions, in which prostate cancer could proliferate [8].

Interestingly, the western lifestyle is also associated with increased breast cancer risk. It seems that the western diet in particular, induces menarche at a younger age and post menopausal obesity, which raises endogenous oestrogen levels [2]. Increased levels of endogenous hormones, such as oestrogen, are believed to play a pivotal role in the development of several cancers of the female reproductive organs [1,2].

1.1.1.5 Genetic factors

Genetic influences are widely considered to be accountable for several cancers [1,2]. Familial clustering of some forms of cancer is thought to be predominantly

due to genetic susceptibility, including: the combined or individual influences of both highly and weakly penetrant genes; and, genetic variations in the synthesis and metabolism of hormones, carcinogen metabolism, DNA repair, and inflammation pathways [1,2,9]. However, inconclusive results have often led to the dismissal of these alone [2,9]. It is more likely that a complex relationship between genetic factors and environmental influences is responsible for the pathogenesis of prostate cancer [2,9].

1.1.2 Cancer classification

Unfortunately, for vertebrates to live long lives, cells must continuously divide for development, maintenance and repair. To do so, vertebrates have evolved ways of inducing cell proliferation when needed, while suppressing clonal autonomy. However, when these processes fail, cancer is the inevitable result [12]. Cancer is a general term used to describe one of the 200 various types of disease causing malignant neoplasms [3]. These are diseases in which the incessant proliferation of somatic cells kills by invading, overthrowing and corroding normal tissues [12]. The dividing cells form masses, or tumours, of undefined structure which can be characterised as either solid or diffuse, according to the tissue or cell of origin [3].

1.1.2.1 Solid tumours

Solid tumours form in tissues and are predominantly made up of neoplastic proliferating cells with a covering, or “stroma” of connective tissue and a blood supply [3]. Solid tumours can be classified as either benign, in-situ, or malignant according to the nature of their bulk of cells. The least aggressive, benign, tumours remain localized and grow slowly, only causing damage through obstruction or pressure [3]. Similarly, *in situ* tumours can be defined by the absence of invasion; remaining localised. These tumours usually develop, and remain, in epithelium (figure 1.2) [13]. However, if the tumour gains the capacity to invade the basement membrane and destroy the supporting mesenchyme (figure 2) they can be described as malignant [3,13].

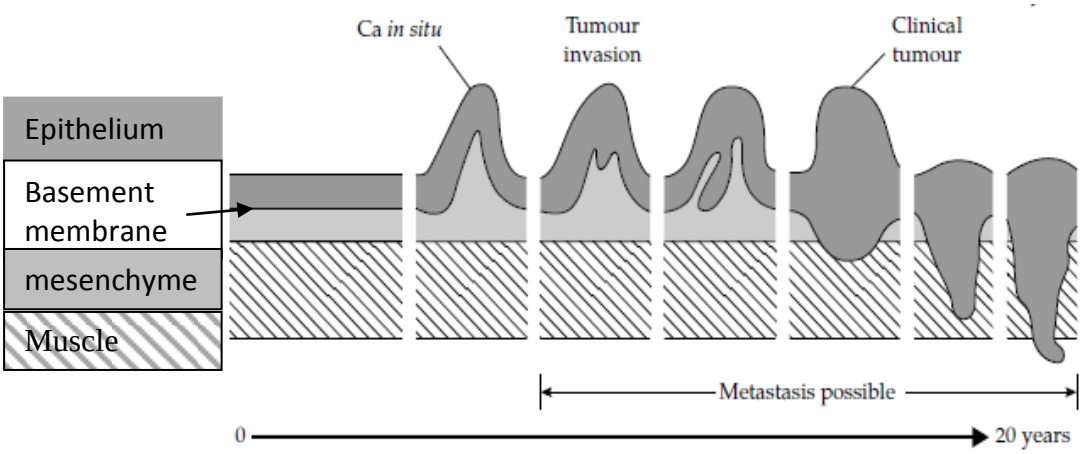

Figure 1.2. Schematic of tumour development adapted from [13].

Malignant tumours can form in any tissue and, when large enough, are able to recruit their own blood supply – a process known as angiogenesis - by stimulating the growth of blood vessels [14]. Furthermore, by penetrating the newly formed blood vessels, tumour cells may be carried to distant sites to produce secondary tumours, also known as metastases [13]. Fortunately, only around 1% of the released cells go on to form metastases as many are broken down by the immune system [15].

The precise nomenclature of solid tumours is based on the generic tissue of origin, such as mesenchyme or epithelium; the specific tissue of origin, e.g. liver or lung; whether it is benign or malignant; if known, the cell of origin; and, finally, the pattern of growth [13]. Malignant tumours, for example, use the prefix *carcinoma* for tissue originating in the epithelium, or *sarcoma* for those of connective tissue, or mesenchyme. If the tumour formed in fat mesenchyme, for example, it would be a *liposarcoma*. For further examples see table 1.1.

Tissue	Cell type	Benign tumour	Malignant tumour
Epithelium			
Skin	Squamous epithelium	Squamous cell papilloma	Squamous carcinoma
Prostate	Prostate epithelium	Adenoma	Adenocarcinoma
Mesenchyme			
Fat	Adipocytes	Lipoma	Liposarcoma
Bone	Osteocytes	Osteoma	Osteosarcoma
Haemato-lymphoid			
Immune system	Lymphoid cells		Hodgkin lymphoma
Central Nervous System			
Meninges	Meningothelial cells	Meningioma	Anaplastic meningioma

Table 1.1. Examples of nomenclature of common tumours adapted from [13].

1.1.2.2 Diffuse tumours

As with solid tumours, haematological malignancies, or diffuse tumours, as sometimes termed, can be broadly divided into groups, in this case, Leukaemias and lymphomas [13]. Leukaemias involve the abnormal proliferation of white blood cells into the bone marrow, peripheral blood and organs [3]. These can be classified according to the cell of origin (myeloid or lymphoid) and pace of the disease (acute or chronic) [3,13]. As the name suggests, acute leukaemias generally progress much faster than chronic forms [3]. Finally, the suffixes –cyt and -blast are used to indicate the maturity of the cells. For example, acute lymphocytic and acute lymphoblastic leukaemias refer to mature and immature cells respectively [3].

Lymphomas arise from cells of the lymphoid system and are grouped as Hodgkin's or non-Hodgkin's types [13]. Hodgkin's lymphomas originate from B lymphocytes and non-Hodgkin's types encompass a wide range of diseases better described elsewhere [13].

1.1.3 Detection, diagnosis and prognosis

Currently, the detection, diagnosis and assessment of the severity of cancer (prognosis) require the use of a combination of various techniques. Preoperative screening techniques are used to detect the disease and postoperative methods are used to diagnose and determine the best modality of treatment to be offered, if required [16].

Interestingly, there is presently a certain amount of controversy surrounding some screening methods [16,17]. Screening tests can produce false positives, which could result in unnecessary emotional stress and other expensive tests. On the other hand, tests can also produce false negatives, which can be dangerous if the cancer is undetected [17]. Finally, there is the danger of detecting "insignificant cancer", which could never grow enough to cause any symptoms. In such cases mismanagement of the disease can be more damaging than the cancer itself [16]. Consequently, only a few screening tests are thought to be consistent enough for routine use [17]. Some of these are presented in more detail below.

1.1.3.1 Preoperative diagnostic modalities

Screening

Before any screening method the doctor will use pre-screening guidelines to assess whether the patient is at risk of cancer [17]. The guidelines include recommendations based on demographic data such as sex, race, age, family history etc [17].

Probably the most commonly used screening method in men is the prostate-specific antigen test [17]. Prostate-specific antigen, or PSA, as often abbreviated, is a serine protease (34 kDa) produced by the prostatic epithelium. Involved in the lysis of the seminal coagulum – formed following ejaculation [18] – this analyte is present in all men with functioning prostate glands [19]. Typically, normal PSA levels will range from 0-4 ng/ml in a man free of significant prostatic disease [20]. The correlation between elevated PSA levels and prostate cancer was first made by the Roswell Park group in 1982 [21]. Subsequently, PSA has become one of the best markers for a cancer today. However, it should be noted that elevated PSA levels can also occur for non-malignant reasons such as: benign prostatic hyperplasia (BPH), prostatic intraepithelial neoplasia (PIN), prostatitis and physical manipulation of the prostate. If undetected a false positive in this case could lead to unnecessary biopsy, which is also concomitant with certain risks [16,17].

In women, a commonly used screening method is the Papanikolaou (Pap) smear test to detect cervical cancer [22]. Invented by George Papanikolaou, this involves the collection of exfoliated cells from the cervix and vagina, which are then placed on a microscope slide, stained and inspected for abnormalities [17,22].

Other less complicated tests can be carried out at home. These include, for example, examination of the testes to help detect testicular cancer and breasts to detect breast cancer [17].

Imaging techniques

Imaging techniques play an important role in diagnosing, staging (discussed later) and evaluating the course of treatment for patients with cancer [23]. Therefore, it is unsurprising that many imaging methods such as: ultrasonography, computed tomography (CT), magnetic resonance imaging (MRI) and various nuclear techniques, have been adapted to this application.

Ultrasonography is one of the most common techniques used. Essentially, it is a non-invasive ultrasound-based imaging technique used to visualize the internal architecture of the area of interest [24]. Importantly, due to the ease of application and low cost of the procedure, it has not only become useful for the diagnosis and staging of cancer, but has also become a vital tool for screening [24].

Computed tomography is an x-ray based technique used to produce three dimensional images of parts of the body based on their ability to absorb x-rays. However, it is difficult to detect cancer in areas such as the prostate because the attenuation of prostatic carcinoma, BPH and the normal prostate are very similar [25]. This problem can be dealt with through the administration of intravenous contrast agents [25]. CT has proven useful in the detection of the extracapsular spread of cancers by assessing irregularities in tissue margins and changes in the density of surrounding fat tissues [25]. Furthermore, CT is able to detect skeletal metastases [23].

MRI is another extremely versatile technique capable of multiplanar, high resolution imaging. At present MRI can be used in a similar way to CT but carries less risk as x-rays are not used, unlike CT scans [23]. It is clear however, that MRI has much more room to evolve and has already seen great benefits, for example, from the development of endorectal and pelvic-surface coils instead of the traditional body coil [26].

Nuclear techniques used for imaging generally involve the use of a radioisotopic tracer designed to target a specific physiological event. For example, bone scintigraphy employs technetium-99m (^{99m}Tc); an element which is used during the remodelling of the bone that is necessary during tumour growth. Images can then be acquired over the whole skeleton to show “hot spots” due to metastases [27]. Other similar techniques include: positron emission tomography, that uses fluorodeoxyglucose labelled with ^{18}F; and,

immunoscinitgraphy, which combines a highly specific antibody – aimed at a cell surface antigen – with an isotope suitable for imaging [27].

1.1.3.2 Postoperative diagnostic methods

Predominantly, biopsies are used to confirm the diagnosis of malignancy following one or more of the previously mentioned preoperative diagnostic modalities. It is also possible, however, to assess the severity of the disease; providing guidance on which course of treatment, if any, to take.

The most widespread histopathological method, used to assess the severity of a tumour, is grading. The most famous of these techniques was introduced by Gleason for assessing prostate cancer [28]. Very simply, these methods utilise optical microscopy to examine the glandular architecture of a tissue sample obtained via biopsy [28]. Once examined, the sample will obtain a score between two and ten; ten being the most severe case. However, this technique, by its very nature, can lack reproducibility as the grading can vary between pathologists [29]. It is therefore unsurprising that inadequate predictions as to the natural history of tumours are frequently made, often leading to mismanagement of the disease.

Combining the results obtained from both preoperative and postoperative diagnostic modalities, clinicians are able to accurately stage the disease according to the TNM (Tumour/Node/Metastases) system (table 1.2) [30].

Stage	Pathology
T0	No evidence of primary tumour.
Tis or Cis	Tumour or cancer in situ.
T1-4	Increasingly advanced cancer stages.
Nx	Adjacent lymph nodes could not be assessed.
N0	Exhibits no metastases.
N1,2,3	Increasing spread to lymph nodes. A higher number is associated with greater spread
M 0,1,x	Distant metastases not present (0), present (1) or isn't clear (x)

Table 1.2. Summary of TNM cancer staging system. Adapted from [30].

Importantly, TNM staging relies heavily on collaborations between pathologists and clinicians. Consequently, diagnosis can often depend on the opinions of a group of people, which, as previously stated can often lead to mismanagement of the disease [29]. Associated with these mistakes are heavy emotional and financial costs [19]. It is thought that developing physical and spectrometric analytical techniques – such as Time-of-Flight Secondary Ion Mass Spectrometry (ToF-SIMS), Infrared and other related techniques – to analyse single cells and mono-layers of cells will eventually provide accurate and repeatable methods to be used for the analytical diagnosis of the severity of cancer.

1.1.4 Cancer cell lines

Cell lines are essentially permanently established cultures of cells that have the ability to proliferate indefinitely. They are able to override telomere erosion – via chemical or viral transformations – and pass the Hayflick limit [31]. This limit would normally restrict their capacity to divide to around 52 divisions, before they become senescent [31]. Each cell line will represent the tumours, from which, they are derived. However, it should not be ignored that the growth conditions of cultured cell lines are not as subtly regulated as they are *in vivo*. Consequently, variations in the cells growth patterns could occur. That aside, there is no evidence to suggest they are genetically altered in culture. For this reason, they are able to provide valuable information about cancer without wasting precious tissue samples.

1.1.5 The cancer cell cycle

The unregulated proliferation that characterises cancer, or rogue, cells is the result of the evasion or negation of restriction mechanisms that control normal clonal autonomy [32]. The following will introduce the cell cycle and regulatory systems, briefly, highlighting the factors contributing to deregulated proliferation.

1.1.5.1 The cell cycle

The series of coordinated events required for DNA replication and cell division can be described as the cell cycle (figure 1.3) [33]. All proliferating cells pass through a cycle of four distinct phases: G_1 is the first gap phase, which is used to manufacture enzymes necessary for DNA synthesis; S phase is the second stage, during which DNA is synthesised; G_2 is the second gap phase needed to produce RNA and proteins for mitosis; and finally, M phase, or mitosis describes the 4 stage process of cell division – well described elsewhere [34].

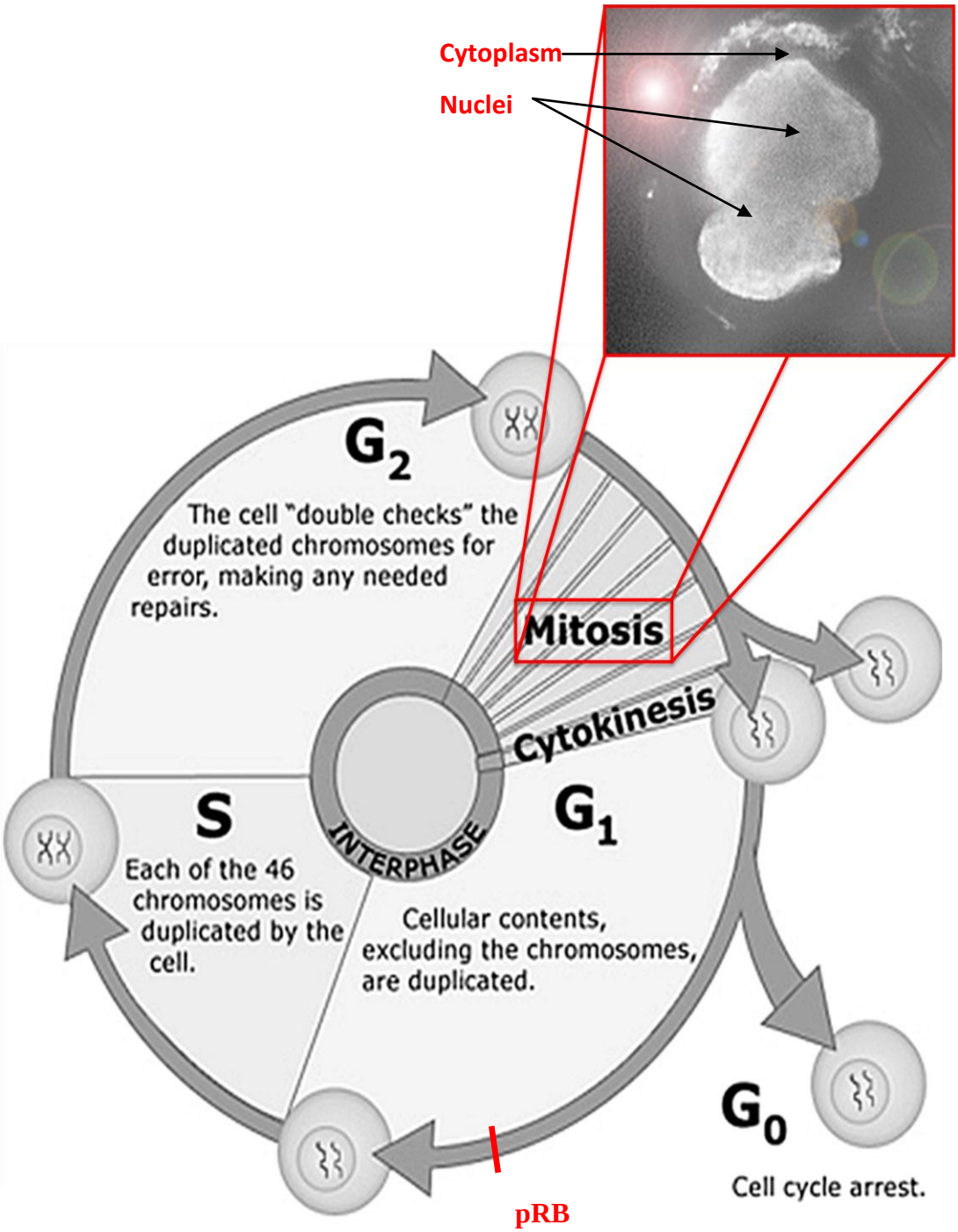

Figure 1.3. Schematic of the cell cycle adapted from [35] and fluorescence image of dividing cells during mitosis.

1.1.5.2 Cell cycle regulation

Normally, non-cancerous somatic cells remain in a non-cycling, or quiescent state of 2n DNA content; often described as a fifth gap phase (G_0). Entry into the cell cycle can only occur upon receipt of various chemical signals known as mitogens [32]. These protein based social cues prevent the onset of proliferation

outside of an appropriate social context [32]. Cell proliferation is further constrained by the presence of a retinoblastoma protein (pRB) regulated transition point towards the end of G_1 (figure 1.3) – a point which most cells only reach after prolonged exposure to mitogens [32].

The proliferative effects of the mitogens are gated by a web of inhibitory growth factors – such as the interferons and transforming growth factors – which has to be overcome for cell cycle entry to occur [32,36]. Acting as potent anti-proliferative agents, these pleiotropic signalling factors act, in part, by suppressing phosphorylation of pRB. This is achieved through the inhibition of cyclin-dependent Kinases (CDKs) and suppression of the transcription factor, and proto-oncogene, c-myc. A more informed discussion of c-myc can be found in references [32,37].

The proliferative potential of normal cells is restrained further by pathways that lead to denucleation of progeny cells, also known as terminal differentiation [38]. Continuous proliferation is only observed in stem cells, which undergo slow, infrequent divisions to replenish specialised cells and maintain the turnover of normal regenerative organs [32,38].

Finally, those cells that do overcome all of the aforementioned inhibitory mechanisms face major obstacles to their continued expansion. Their dependence on trophic factors and physical barriers of epithelial tissue prevent further expansion and evasion [32].

1.1.5.3 Deregulated proliferation

As previously stated, cancer and the cell cycle are fundamentally linked by the fact that cell cycle machinery controls proliferation, and cancer is a disease characterised by the evasion, or negation, of the mechanisms that restrict proliferation [33].

Probably the most important or common defects, resulting in the inception of cancer are related to pRB [33]. This is an important check point in the cell cycle, more specifically, late G_1 phase (figure 1.3). Defects in this pathway are numerous, however, commonly, the RB gene is deleted or the cyclin dependent kinases responsible for the phosphorylation – and inactivation – of pRB are deregulated [32,33].

It is important to reiterate that the reasons for the onset of cancer are too numerous to cover in this thesis. For more in-depth reviews see Evan and Vousden [32] and Collins *et al.* [33].

1.1.6 Cell physiology

Since the purpose of the following investigation is to investigate mammalian cancer cells it is important to briefly describe the structures that are likely to be responsible for the biochemistry observed. Due to the nature of the analytical techniques used however, it is only appropriate to discuss the gross chemistry of the cell as this dominates spectra. Therefore, only larger organelles will be discussed including: the cell membrane, endoplasmic reticulum, Golgi apparatus and nucleus.

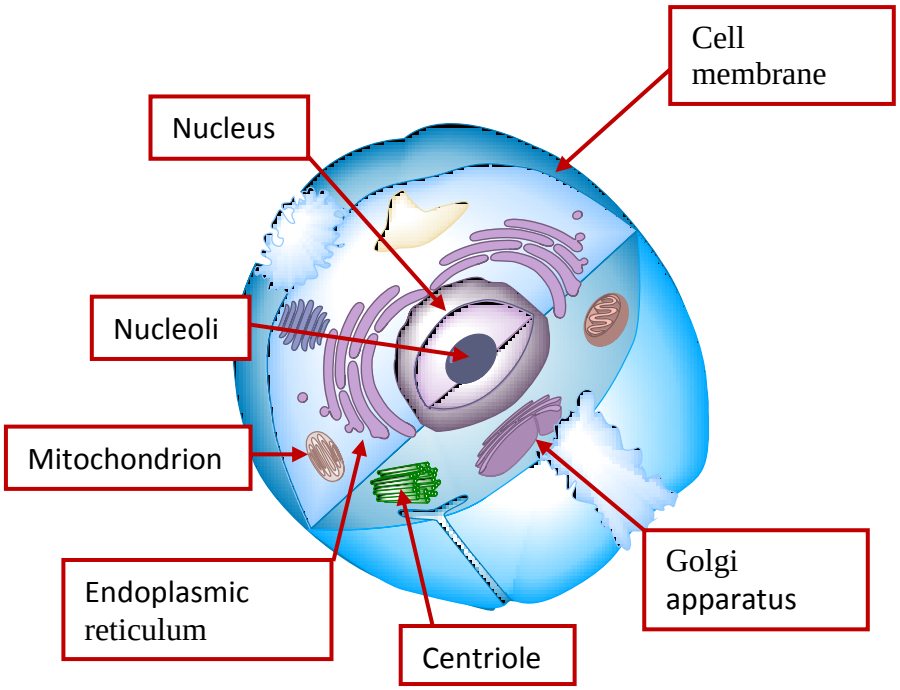

Figure 1.4. Schematic of a mammalian cell.

1.1.6.1 Biological membranes

Cell membranes encapsulate the cell and maintain the essential differences between the intra- and extracellular environments (figures 1.4 and 1.5) [39]. The membrane contains a series of specialised proteins that allow the passage of certain solutes; transmit information in response to environmental cues, allowing the cell to change its behaviour accordingly; provide structural links; or, synthesise ATP (figure 1.5) [39]. It should be noted that there are many other roles of membrane bound proteins that are often specific to certain cell types [39].

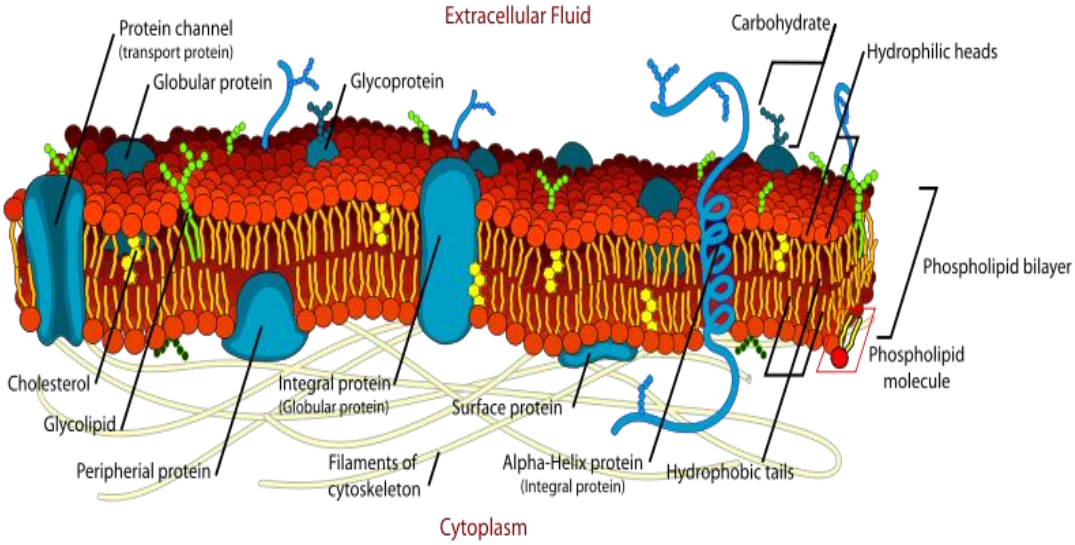

Figure 1.5. Schematic of the cell membrane. Reproduced from [40].

All biological membranes share a basic 5nm thick structure: each is comprised of a thin film of noncovalently bound lipids and proteins [39]. This allows for the fluid structure – originally proposed by Singer and Nicholson (Figure 1.5) [41] - such that the majority of the molecules within the membrane are able to move around laterally [39]. Phospholipid molecules are arranged with their hydrophobic, aliphatic tails pointing towards each other, while their hydrophilic polar head groups form the inner and outer surfaces of the membrane (figure 1.5 and 1.6) [39]. The majority of these phospholipids all share the same phosphoglyceride backbone with differing ionic heads and saturated, or unsaturated, fatty acid tail groups (e.g. figure 1.6) [39]. Commonly, the outer layer of the membrane is made up of phosphocholines (e.g. figure 1.6), whereas

the inner part consists of mainly phosphatidylethanolamine, phosphatidylserine, and phosphatidylinositol to name a few [42].

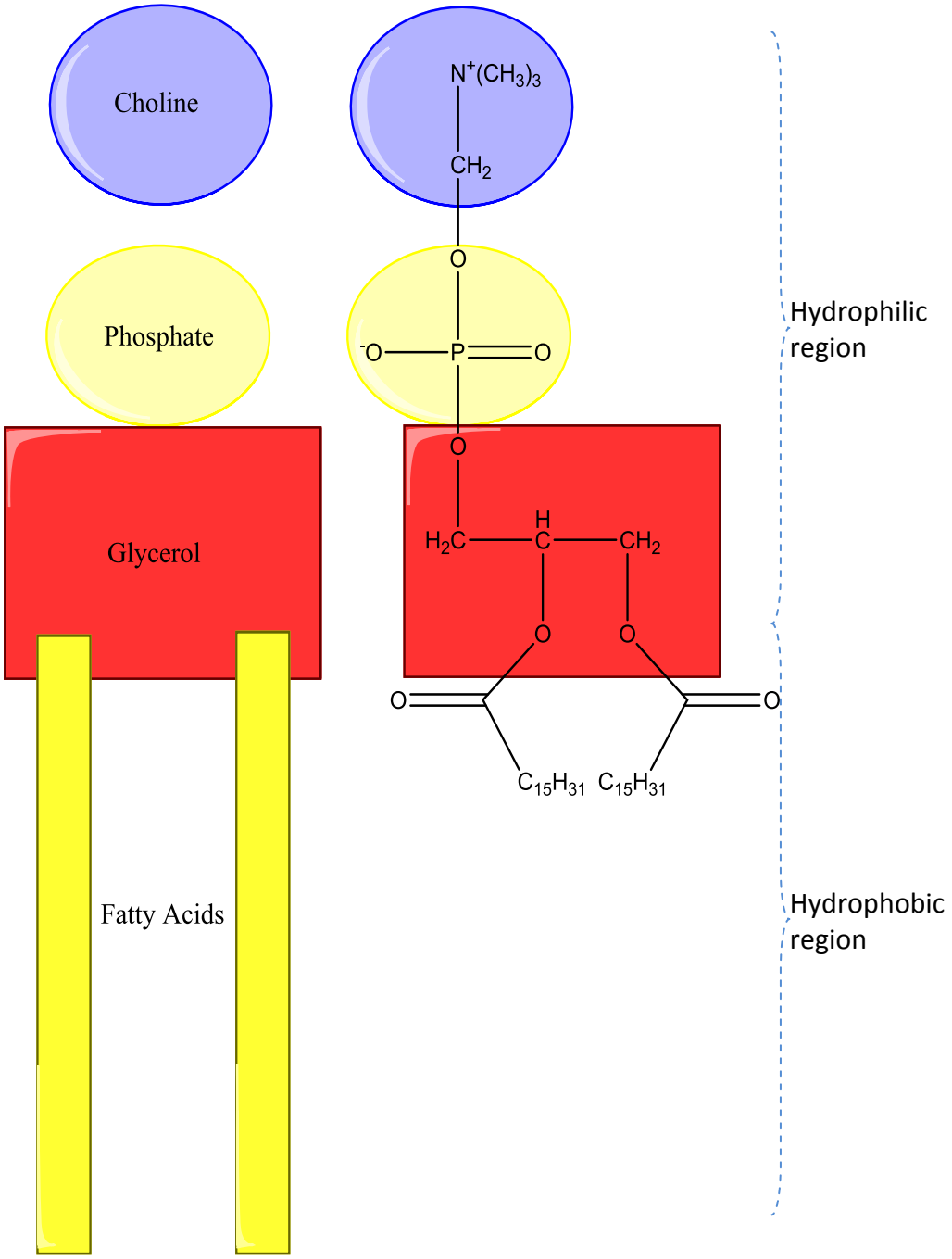

Figure 1.6. Schematic and Structure of 1,2-dipalmatoyl-sn-glycer-3-phosphocholine (DPPC).

The membrane is not just made up of proteins and phospholipids. There are also glycolipids, sphingolipids such as sphingomyelin – derived from serine – and cholesterol (figure 1.7). Cholesterol is particularly important as it can change the permeability of the membrane [39]. The polar head group (figure 1.7) of cholesterol is positioned next to the head group of a phospholipid. Consequently, the rigid, steroid rings partially immobilize the neighbouring regions of fatty acid chain [39]. In doing this, cholesterol makes the membrane less fluid therefore decreasing permeability to small water-soluble molecules [39]. Furthermore, it also prevents possible phase transitions as the hydrocarbon chains are unable to come together and crystallise [39].

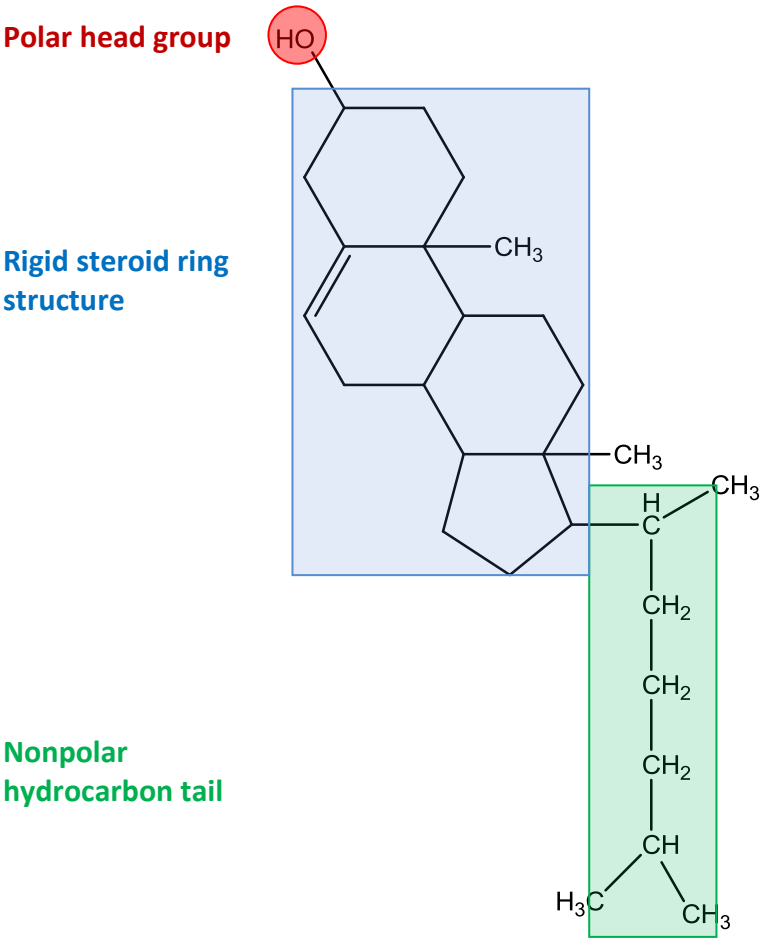

Figure 1.7. Structure of cholesterol

Most of the molecules present within the cell membrane are also present, in varying concentrations, within the membranes of other organelles (table 1.3).

These lipids together constitute a large part of the membrane, however, there are many physiologically important lipids in much lower concentrations well described elsewhere [39,42].

Lipid	Liver cell	Red blood cell	Mitochondrion	Endoplasmic reticulum
Cholesterol	17	23	3	6
Phosphatidylethanolamine	7	18	25	17
Phosphatidylserine	4	7	2	5
Phosphatidylcholine	24	17	39	40
Sphingomyelin	19	18	0	5
Glycolipids	7	3	Trace	Trace
Others	22	13	21	27

Table 1.3. Major Lipid compositions of different membranes as a percentage of total lipids by weight. Reproduced from [39].

1.1.6.2 Endoplasmic reticulum and Golgi apparatus

The endoplasmic reticulum (ER) (figure 1.4) is a labyrinth of flattened compartments and tubules made out of a membrane similar to that which encapsulates the cell, as described in section 1.1.6.1 [39]. These form a single internal space, or lumen, known as the endoplasmic reticulum cisternal space [43]. The endoplasmic reticulum membrane is essentially a selectively permeable connection between the cytoplasm, cisternal space and the nucleus [43]. Accounting for up to 60% of all cellular membrane, it is divided into two morphologies. The rough endoplasmic reticulum (RER) is generally comprised of flattened compartments [43]. The outer surfaces of the compartments are covered with ribosomes that synthesise proteins to be embedded in membranes; impounded in internal compartments; or, exported or secreted from the cell [43]. These proteins are first transported into the cisternal space for completion and then often onto the Golgi apparatus (figure 1.4) –

responsible for sorting molecular traffic - for further modification and allocation [43]. The smooth endoplasmic reticulum (SER) is a more tubular structure and is chiefly responsible for the synthesis of lipids, detoxification of poisons and assembly of glycogen for carbohydrate metabolism [43]. Furthermore, the SER stores calcium used to trigger muscle contractions and assemble the cytoskeleton. Due to these functions, cells specializing in detoxification, or muscle cells, for example, will have a much larger ER [43].

1.1.6.3 The nucleus

The nucleus houses most of the genetic material, in the form of DNA, in a eukaryotic cell [44]. Occupying around 10% of the cell volume, the nucleus is surrounded by nuclear envelope, which is continuous with and of similar construction to the membrane of the ER (see 1.1.6.1) [39,43,44]. This envelope helps to maintain the integrity of the genetic material only allowing molecules in and out through large pores [44]. The nucleus is structurally supported by a series of internal filaments, known as lamina, and a meshwork of external filaments [44].

1.2 Secondary Ion Mass Spectrometry (SIMS)

Secondary ion mass spectrometry, or SIMS, as commonly abbreviated, is a surface analysis technique. Mass spectra of ionised surface particles, or secondary ions – emitted, or sputtered, via high energy (KeV) primary ion beam bombardment – can be obtain for a wide range of materials [45].

The subsequent section will provide an overview of the most important theories and fundamental processes associated with the SIMS experiment.

1.2.1 Secondary ion formation

The impingement of high energy primary ions upon a sample surface sets off a cascade of events, through which their energy is transferred. Very simply, these events consist of desorption, or sputtering, as sometimes termed, and ionisation processes [45]. Several attempts have been made to theorize as to the

mechanics of secondary ion formation, the most popular of which, will be discussed in the following section.

1.2.1.1 Sigmund's linear cascade theory

The simplest way of describing the sputtering process is through Sigmund's linear cascade model of hard spheres [46]. The theory suggests that the impingement of a primary ion beam (typically between 10 and 40KeV), onto a surface, will result in a cascade of elastic collisions between the atoms of the solid – within approximately 30Å of the surface (figure 1.8). Some of these collisions will return to the surface resulting in the emission, or sputtering, of atoms and atom clusters as represented pictorially in figure 1.8 [45]. The amount of sputtering is related to the density, mass and surface binding energy of the material [45].

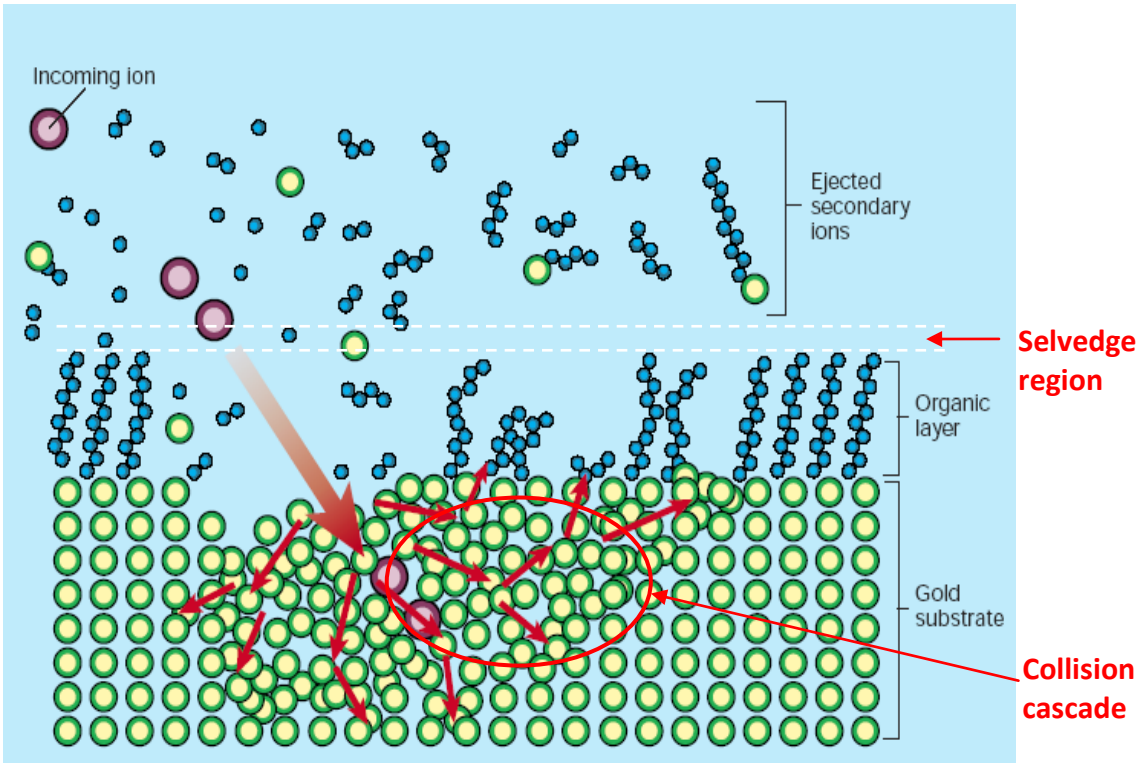

Figure 1.8. The sputtering process. Adapted from [47].

Sigmund's theory is, however, reliant upon several criteria:

- Only two atoms collide at any one time.
- Sputtering occurs at small particle current and fluence; excluding conditions where excessive heating and sample damage occur.
- Electronic excitation sputtering is ignored, which may be valid for high energy primary ion beams, but at lower energies electronic interactions between target atoms and incident particles should not be dismissed [45].

Sigmund's theory, therefore, is more suited for simple materials such as simple organic layers on atomic substrates as illustrated in figure 1.8. It does not take into account bonding or vibrational excitation, so is essentially descriptive of a stack of individual atoms. To understand secondary ion formation within complex organic systems, much more intricate models are required such as the molecular dynamics simulations of Garrison *et al.* [e.g. 49]. In this particular example self-assembled monolayers of *n*-alkaniothiolates on a substrate of Au(111) were modelled. The sputtering yields that were gained, following low energy (500eV) argon bombardment, were close to experimental data [49]. Importantly, computer modelling has served as a way of visualising the sequence of events that lead to the liberation of secondary ions and their relationship with surface chemistry. This example visualises the collision cascades responsible for the emission of intact molecules, occasionally attached to gold substrate atoms – as also illustrated by figure 1.8 [47,49]. Furthermore, smaller fragments have been shown to form as a result of direct primary ion impact and further fragmentation above the sample surface after emission [49]. These models, however, do not take into account ionization.

1.2.1.2 Ionization models

Originally developed for cluster ion formation from oxide surfaces, the nascent ionization model suggests that prior to sputtering, rapid electronic transitions occur [50]. Through these transitions, ions are neutralised before they are ejected from the surface. Secondary ions, therefore, are thought to occur due to

the “non-adiabatic dissociation of sputtered nascent ion molecules” above the surface [50]. In simple terms, this suggests that energy is transferred between the ion beam and sample, leading to the dissociation of neutral molecules.

A second, frequently used theory is the desorption ionisation model as proposed by Cooks and Busch [51]. Cooks and Busch propose that vibrational excitation plays an important role in the emission of cluster or molecular ions from organic materials. Essentially, large numbers of neutral molecules are desorbed, but must be ionised before they can be detected. Ionisation is thought to occur through a low energy process such as cationisation after desorption has occurred [48]. This can occur through two types of reaction: fast ion/molecule reactions or electron ionisation in the selvedge region – the intermediate pressure region between the sample surface and vacuum (figure 1.8); and, unimolecular fragmentation in the vacuum – related to the primary ion beam energy [45].

1.2.1.3 The SIMS equation

The intricacies of sputtering and secondary ion formation are still not entirely understood. What is clear though is the relationship between the number of secondary ions, the sample and the experimental conditions. This is exemplified by the following equation, known as the SIMS equation:

(1.1) $$I_m = I_p Y_m \alpha^+ \vartheta_m \eta$$

Where I_m is the secondary ion current of species m; I_p is the primary particle flux; Y_m is the average number of molecules or atoms ejected from the sample per incident ion, or, sputter yield; $\alpha^{\pm}$ is the ionisation probability to positive or negative ions; ϑ_m is the fractional concentration of the chemistry of species m in the surface layer; and, finally, η is the transmission of the analysis system [45].

The above equation can be used to calculate the secondary ion yield of a sample when subjected to static SIMS (discussed later) analysis. However, it should be noted that the sample's immediate chemical environment can also affect the secondary ion yield through altering the ionisation probability - a phenomenon known as the matrix effect.

1.2.2 Dynamic and Static SIMS

Static conditions are specifically designed to maintain the integrity of the surface layer while recording a complete spectrum [52]. Given a surface consisting of 10^{15} atoms/cm^2, a static SIMS experiment would aim to target 1% of these to minimise damage to sample layers beneath the surface to preserve the molecular structure of the sample. The maximum primary ion dose for such an experiment should be no greater than 1 x 10^{13} ions/cm^2, otherwise known as the static limit [53]. Organic samples, however, usually require a more delicate approach, being more susceptible to damage. It is therefore usual to operate well below the static limit (10^{12} ions/cm^2) [45].

Dynamic SIMS requires high primary ion flux densities, to deliberately increase the damage done by the impinging ion beam. Consequently, the sample is consumed and fewer molecular ions are desorbed, yielding mostly elemental ions [53].

1.2.3 Imaging ToF-SIMS

To create an image using ToF-SIMS the primary ion beam is rastered across the sample surface; recording a spectrum for every pixel. In this way, it is possible to map molecules by selecting peaks within those spectra and creating images to illustrate the localization. The ability to create high resolution images, using ToF-SIMS, was acquired through certain, key developments.

The time-of-flight mass analyser – discussed later in more detail – is widely considered as one of the most integral imaging components. The ToF's "quasi-parallel" ion detection allows multiple masses to be detected at any one time [54]. The use of a pulsed primary ion beam allows for greater chemical

specificity by helping to define the start and arrival times of the secondary ions for the accurate determination of secondary ion flight times and therefore m/z. The user is also able to either run experiments with high mass resolution (shorter pulses) or high spatial resolution (longer pulses) [54].

The production of secondary molecular ions is equally as important a factor as the use of a time-of-flight tube; able to influence both the resolution and quality of a chemical image [55]. The key parameter governing secondary ion production is the choice of primary ion beam. Recently, it has become apparent that polyatomic or molecular projectiles such as Au_3^+, C_{60}^+, Bi_3^+ etc are capable of improving secondary ion yields, and therefore, sensitivity. Furthermore, cluster ion bombardment has made it possible to obtain molecular information at depth - in certain materials – while avoiding damage accumulation [56]. Of the polyatomic primary ion beams, C_{60}^+ is the most exciting. Dramatic increases in yield (10^3 to 10^4) accompanied by a significant fall in sub-surface sample damage have been observed using this projectile. This also allows one to expose the sample to greater fluences of primary ions beyond the static limit, further increasing signal levels. This combination of higher yields and increased primary ion impacts has led to a gain in sensitivity to retrieve molecular information [56]. This is particularly important for low concentrations of analytes and/or small pixel sizes.

1.3 Fourier transform infrared spectroscopy (FTIR)

Part of the broad spectrum of electromagnetic radiation, infrared spans the low energy, red region of 13000 to 10 cm^{-1}, or wavelengths from 0.78-1000 μm [57]. The subsequent section provides an introduction to important infrared theory.

1.3.1 Infrared absorption theory

A sample's absorption of infrared is presented as either wavelengths (λ) or wavenumbers ($\tilde{\nu}$). Wavenumber refers to the number of repeating wave units in a length of 1 cm; therefore, it is directly proportional to frequency, and, the energy of IR absorption [57]. Conversely, the wavelength – the distance between

two equivalent points on successive waves - is inversely proportional to frequency and associated energy. The two can be interconverted by the following equation [57]:

(1.2) $\tilde{\nu}\ (\mathrm{cm}^{-1}) = [1/\ \lambda\ (\mu\mathrm{m})] \times 10^4$

Infrared spectra generally consist of wavenumber or wavelength on the x-axis and absorption, or percentage transmittance, on the y-axis. Transmittance (*T*) can be defined as the ratio of the intensity of the radiant power emerging from the sample (*I*) to the intensity of the incident radiation (I_0) and can be related to absorbance (*A*) by the following [58]:

(1.3) $A = \log_{10}(1/T) = -\log_{10}T = -\log_{10}I/I_0$

1.3.1.1 Vibrational spectroscopy

All atoms in molecules vibrate continuously. If the frequency of the vibration is equal to the IR radiation frequency, the molecule will absorb the radiation [57]. A molecule consisting of *N* atoms will have 3*N* degrees of freedom, corresponding to motions along the three Cartesian coordinates (x, y, and z) [58]. Three of these degrees describe translational motion and three represent rotational motions [57]. This leaves 3*N* – 6 degrees of freedom, to describe the number of vibration modes in a non-linear molecule. Linear molecules, however, only have 2 rotational degrees of freedom thus leaving 3*N*-5 degrees of freedom [57].

Predominantly, molecular vibrations are made up of various types of stretching and bending (figure 1.9). Bending modes involve a change in bond angle between two atoms, whereas stretching modes are associated with a change in interatomic distances (figure 1.9).

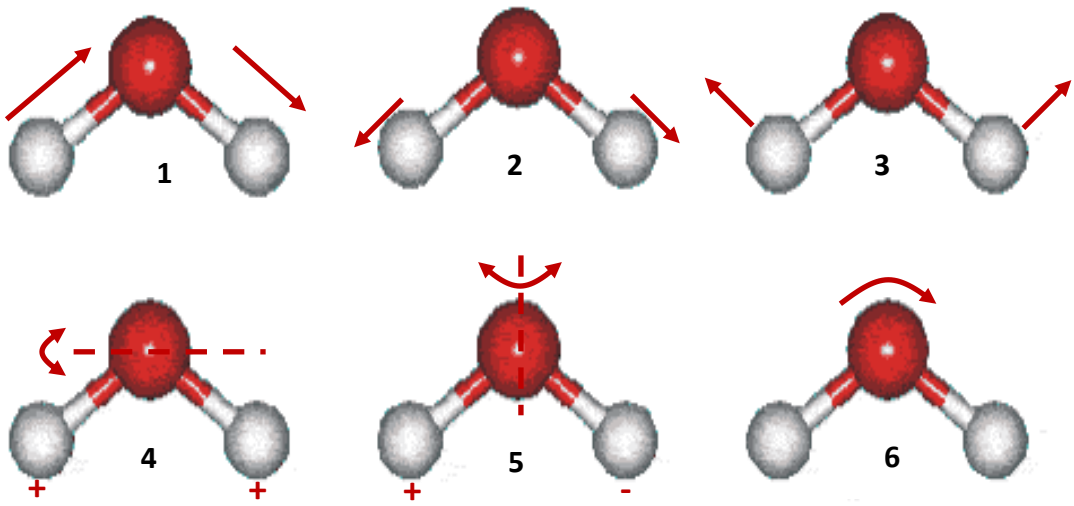

1. Asymmetric stretch.

2. Symmetric stretch.

3. In-plane bending or scissoring.

4. Out-of-plane bending or wagging.

5. Out-of-plane bending or twisting.

6. In-plane bending or rocking.

Only true if the red atom is bonded to something. E.g a CH_2 group in a hydrocarbon

Figure 1.9. Major vibrational modes. Adapted from [59].

1.3.1.2 Group frequencies

Functional groups within a molecule produce bands in the IR spectrum at specific, narrow frequency ranges. It is therefore possible to use the IR spectrum to determine the presence or absence of certain functionalities for the structural elucidation of an unknown compound [57]. The fingerprint region (~800 – 1400 cm^{-1}) is of particular importance when identifying an unknown compound. It includes contributions from many complex vibrations, which, provides a "fingerprint" for a compound [57].

The group frequencies in the spectrum can be affected by certain factors, which are mostly related to altering bond stiffness. For example, the presence of hydrogen bonding can result in a reduction in bond stiffness with an associated lowering of the stretching frequency and absorbance. This is particularly

noticeable with an O-H stretching absorption, which will appear as a much broader peak at a lower frequency if hydrogen bonded. Other factors may also include steric, inductive or resonance effects from various substituents, which can cause bond stiffening and increases in the frequency of vibration [60]. Probably the most important factor that can affect the intensity of absorption is the dipole moment. This is because absorptions only occur for a vibration that causes a change in dipole moment. Symmetrical molecules, for example, show little or no absorption, as vibration across the centre of symmetry does not lead to a change in dipole moment.

1.3.1.3 Beer-Lambert law

The use of FTIR for quantitative analysis is based upon the Beer-Lambert law, which is as follows:

(1.4) $$A = \varepsilon \, l \, c$$

Where ***A*** is the absorbance; ***ε*** is the extinction coefficient, also known as the molar absorptivity (cm^{-1} mol^{-1} dm^3); ***l*** is the path length (cm); and ***c*** is the concentration (moles dm^{-3}).

However, for this equation to be true the sample must be at a concentration of less than 0.01M. This is because electrostatic interactions can form between molecules in close proximity; high concentration can change the refractive index; light can be scattered by particulates; and, finally, shifts in chemical equilibria, as a function of concentration, can occur. This will have implications for cellular analysis, however, a novel correction algorithm (discussed later in section 2.1.1.) will be employed to correct spectral artefacts caused by non-Beer-Lambert absorptions.

1.4 Principal Component Analysis

More and more multivariate statistics are being utilised to explore analytical data and extract meaningful information, as patterns in such information rich procedures can be hard to find. Principal component analysis (PCA) - used in this investigation - weighs all of the available variables to provide the maximum discrimination between data. In other words, it aims to reduce the dimensionality of data [61,62].

PCA results in a mathematical transformation of data to give a scores matrix of column vectors, with the same number of rows as the original data matrix; and, a loadings matrix of row vectors with as many columns as the original data matrix (figure 1.10). The first vectors from each of these matrices are often referred to as eigenvectors of the first principal component. To create the principal components - assuming the data is continuous and normally distributed - PCA elucidates a linear combination of variables (a component), capturing as much of the variation as possible (figure 1.10) [61,62]. In other words, principal components are vectors in *n*-dimensional space with each variable in the analysis representing an axis. This is then repeated to introduce a second component, unrelated and orthogonal to the first, to account for as much of the remaining variation as possible (figure 1.10). This procedure is then repeated until the number of components is equal to the number of variables [61,62]. In the case of ToF-SIMS and FTIR the components are most likely related to chemical differences between samples.

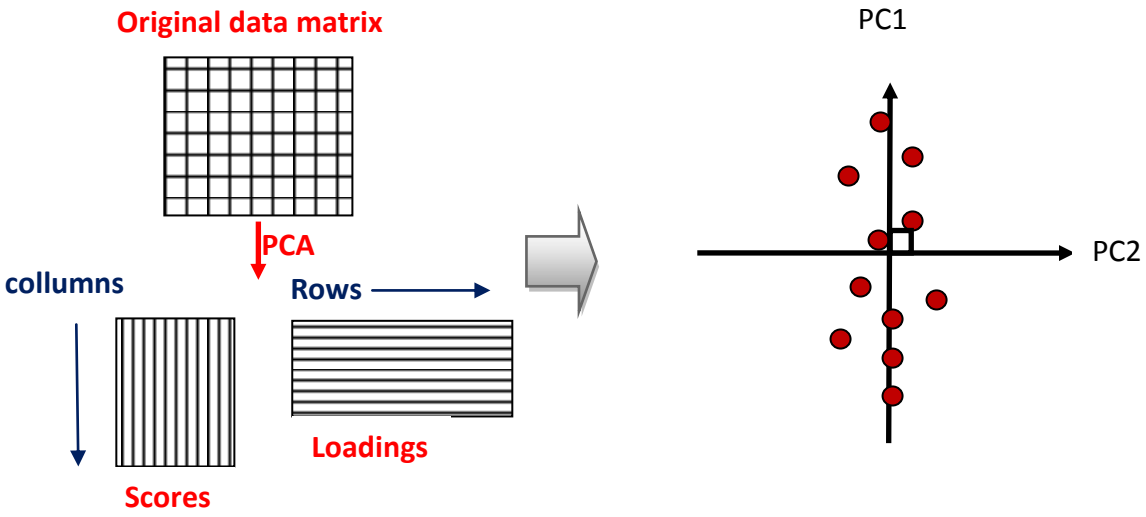

Figure 1.10. Schematic representation of the PCA process. Adapted from [63].

In this way, the total variance is unchanged, but redistributed so the largest amount of variance is assigned to the first component and the second largest to the second etc [61,62]. The first three of these have high eigenvalues (related to a large separation of group means) and are able to satisfactorily describe the data set. These components can then be used as vectors to create a two or three-dimensional space (or plot), onto which each variable is projected (figure 1.11). The positioning for each variable is dependent upon its weighting upon each component [61,62].

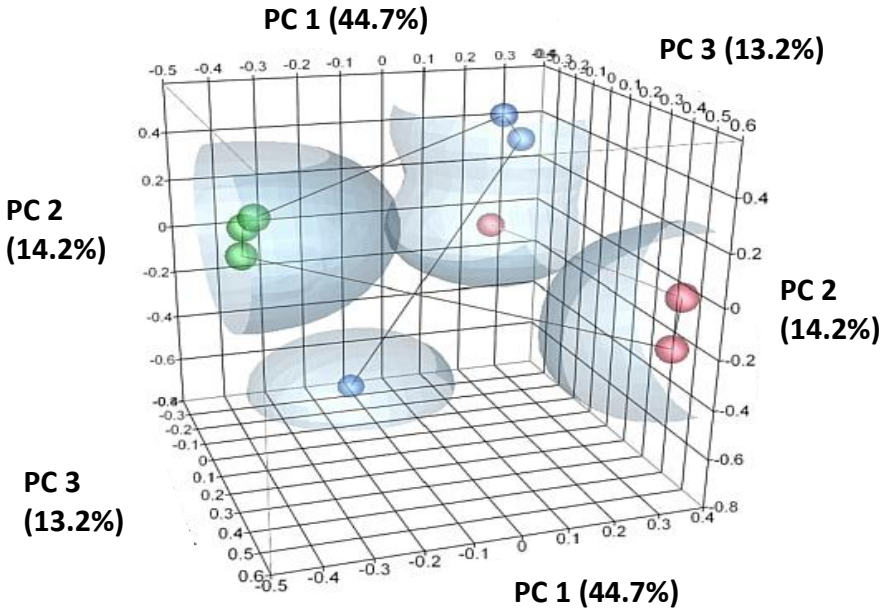

Figure 1.11. Example of a 3-dimensional PCA scores plot. Highest variance described by Principal component 1, then 2 etc. Taken from [64].

References

[1] IARC. Introduction: Needs and Prospects for Cancer Control. In: *Word Cancer Report*. International Agency for Research on Cancer (2008) Chapter 1.1 p7-20 ISBN 978 92 832 0423 7

[2] J. Peto. *Nature.* 411 (2001) p390-395

[3] J. Roboz. Relevant concepts of cancer medicine and biology. In: *Mass spectrometry in cancer research.* CRC press LLC (2002) Chapter 3 p81-105. ISBN 0-8493-0167-X

[4] R. Doll and R. Peto. *Journal of the National Cancer Institute.* 66 (1981) p1191-1308

[5] B.Q. Liu, R.Peto, Z.M. Chen, J. Boreham, Y.P. Wu, J.Y. Li, C.Campbell and J.S. Chen*. British Medical Journal.* 317 (1998) p1411-1422

[6] D. Hoffman, I. Hoffman and K El-Bayoumy. *Chemical Research in Toxicology.* 14 (2001) p767-790

[7] F.L. Meyskens, Jr and E. Szabo. *Cancer Epidemiology, Biomarkers and Prevention.* 14 (2005) p1366-1369

[8] H. Gronberg. *Lancet.* 361 (2003) p859-864

[9] A.W. Hsing and Chokkanlingham. *Frontiers in Bioscience.* (2006) p1388-1413

[10] J.M.M. Walboomers, M.V. Jacobs, M.M. Manos, F.X. Bosch, J.A. Kummer, K.V. Shah, P.J.F. Snijders, J.Peto, C.J.L.M. Meijer and N. Muñoz. *Journal of Pathology.* 189 (1999) p12-19

[11] K Griffiths and M Morton. Aspects of the cell biology of prostate cancer. In: *Prostate cancer pathology, diagnosis and treatment*. Cambridge University Press. (2000) Chapter 4 p51-74. ISBN 1-85317-422-X

[12] G.I. Evan and K.H. Vousden. *Nature.* 411 (2001) p342-348.

[13] L.M. Franks and M.A. Knowles. What is cancer? In: *Introduction to the cellular and Molecular Biology of Cancer.* Oxford University Press (2005) Chapter 1 p1-25 ISBN 0-19-856853-3

[14] G. Bergers and L.E. Benjamin *Nature Reviews Cancer.* 3 (2003) p401–410

[15] L Weiss. Metastatic Inefficiency. In: *Principles of Metastases*. Academic Press: USA (1985) p134–159.

[16] M.R. Jarmulowicz. The role of pathology in biopsy, diagnosis and management of prostate cancer. In: *Prostate cancer pathology, diagnosis and treatment.* Cambridge University Press. (2000). Chapter 2 p17-33. ISBN 1-85317-422-X

[17] M.G. Fury. The Merk Manuals Online Medical Library. http://www.merck.com/mmhe/sec15/ch181/ch181c.html (2006). Visited on 14/06/2010.

[18] M Robert and C Gagnon. *Cell and Molecular Life Sciences.* 55 (1999) p944-960

[19] J Siegal and M.K. Brawker. Prostate specific antigen. In: *Prostate cancer pathology, diagnosis and treatment.* Cambridge University Press. (2000). Chapter 8 p121-141. ISBN 1-85317-422-X

[20] Beckman Coulter. http://www.beckmancoulter.com/products/testdetail/access/psa.asp (2010). Visited on 14/06/2010.

[21] Roswell Park Cancer Institute. http://www.roswellpark.org/giving/impact/discovery-and-cures/beyond-psa-test (2010). Visited on 14/06/2010.

[22] G.N. Papanicolaou and H.F. Traut. *American Journal of Obstectrics and Gynecology*. 42 (1941) p193-206.

[23] J Saad, S.S. Sandu and A Watkinson. Computed tomography and magnetic resonance imaging in the management of prostate cancer. In: *Prostate cancer pathology, diagnosis and treatment.* Cambridge University Press. (2000). Chapter 10.2 p169-187. ISBN 1-85317-422-X

[24] H Watanabe and M Kojima. The role of transrectal ultrasound in prostate cancer and its use in biopsy. In: *Prostate cancer pathology, diagnosis and treatment.* Cambridge University Press. (2000). Chapter 9 p143-155. ISBN 1-85317-422-X

[25] J.M. Price and A.J. Davidson. *Urological Radiology.* 1 (1979) p39-42

[26] M.L. Scheibler, M.D. Schnall, H.M. Pollack, R.E. Lenkinski, J.E. Tomaszewski, J.A. Wein, R Whittington, W Rauschning and H.Y. Kressel. *Radiology*. 189 (1993) p339-352

[27] J Buscome and A Hilson. Nuclear medicine in prostate cancer. In: *Prostate cancer pathology, diagnosis and treatment.* Cambridge University Press. (2000). Chapter 10.1 p156-167. ISBN 1-85317-422-X

[28] D.F. Gleason. Histological grading and clinical staging of prostate carcinoma. In: *Urological pathology - the prostate.* Lee and Febiger. (1977). p171-197

[29] J.B Lattouf and F Saad. *British Journal of Urology International.* 90 (2002) 694-699

[30] National Cancer Institute. http://www.cancer.gov/cancertopics/factsheet/Detection/staging (2004). Accessed on 14/06/2010.

[31] J.W. Shay and W.E. Wright. *Nature Reviews Molecular Cell Biology*. 1 (2000) p72-76

[32] G.I. Evan and K.H. Vousden. *Nature*. 411 (2001) p342-348

[33] K. Collins, T. Jackson and N.P. Pavletich. *Proceedings of the National Academy of Sciences* USA. 94 (1997) p2276-2778

[34] J. Roboz. Relevant concepts of cancer medicine and biology. In: *Mass spectrometry in cancer research.* CRC press LLC (2002) Chapter 13 p81-105. ISBN 0-8493-0167-X

[35] The university of Leicester virtual genetics education centre. http://www.le.ac.uk/ge/genie/vgec/he/cellcycle.html (2009). Visited on 16/06/2010.

[36] H.A. Coller. *Nature Reviews Molecular Cell Biology.* 8 (2007) p667-670.

[37] J. Gearhart, E.E. Pashos and M.K. Prasad. *New England Journal of Medicine*. 357;15 (2007) p1469-1472

[38] C.E. Gagna, H.R. Kuo, E. Florea, W. Shami, R. Taormina, N. Vaswani, M. Gupta, R. Vijh and W.C. Lambert. *The Journal of Histochemistry and Cytochemistry*. 49;7 (2001) p929-930.

[39] B. Alberts, A. Johnson, J. Lewis, M. Raff, K. Roberts and P. Walter. Membrane structure. In: *Molecular biology of the cell*. Garland Science (2002) Chapter 10 p583-614. ISBN 0-8153-4072-9

[40] The University of New South Wales Cell Biology. http://cellbiology.med.unsw.edu.au/units/science/lecture0803.htm. Accessed on 29/06/2010.

[41] S.J. Singer and G.L. Nicholson. *Science*. 175 (1972) p720-731

[42] G.L. Patrick. The why and the wherefore: drug targets. In: *An introduction to medicinal chemistry.* Oxford University Press (2005) Chapter 2 p8-23. ISBN 0-19-927500-9

[43] B. Alberts, A. Johnson, J. Lewis, M. Raff, K. Roberts and P. Walter. Intracellular compartments and protein sorting. In: *Molecular biology of the cell*. Garland Science (2002) Chapter 12 p659-710. ISBN 0-8153-4072-9

[44] B. Alberts, A. Johnson, J. Lewis, M. Raff, K. Roberts and P. Walter. DNA and chromosomes. In: *Molecular biology of the cell*. Garland Science (2002) Chapter 4 p191-234. ISBN 0-8153-4072-9

[45] J C Vickerman. ToF-SIMS An overview. In: *ToF-SIMS surface analysis by mass spectrometry*. IM publications (2001) Chapter 1. p1-41 ISBN 1 901019 03 9

[46] P.Sigmund. Sputtering measurements. In: *Sputtering by particle bombardment.* Springer-verlag (1981) p 9. ISBN 978-3-540-44500-5

[47] D.G. Castner. *Nature* 422 (2003) p129-130

[48] J.C. Vickerman. Molecular surface mass spectrometry by SIMS. In: *Surface analysis – the principal techniques 2nd Edition*. John Wiley and Sons, Ltd (2009) Chapter 4 p113 -205. ISBN 978-0-470-01763-0

[49] K.S.S. Liu, C.W. Yong, B.J. Garrison and J.C. Vickerman. *Journal of physical chemistry B* 103 (1999) p3195

[50] W. Gerhard and C. Plog. *Physica B: condensed matter*. 54 (1983) p59-70

[51] R.G. Cooks and K.L. Busch. *International journal of mass spectrometry* and ion physics. 53 (1983) p111-124

[52] A. Benninghoven. *Surface Science*. 299/300 (1994) p246-260

[53] D. McPhail and M. Dowsett. Dynamic SIMS. In: *Surface analysis – the principal techniques 2nd edition*. John Wiley and Sons, Ltd (2009) Chapter 5 p207-268. ISBN 978-0-470-01763-0

[54] A. Benninghoven, B. Hagenhoff and E. Niehuis. *Analytical Chemistry*. 65 (1993) pA630 – A640

[55] M.L. Pacholski and N Winograd. *Chemical reviews.* 99 (1999) p2977-3006

[56] A. Wucher. *Applied surface science.* 252 (2006) p6482-6489

[57] C.P.S. Hsu. Infrared spectroscopy. In: *The handbook of instrumental techniques for analytical chemistry*. Prentice Hall (1997) Chapter 15 p247-283. ISBN 0131773380

[58] P.R. Griffiths and J.A. de Haseth. *Fourier transform infrared spectrometry 2nd edition*. John Wiley and Sons (2007) ISBN 978-0-417-19404-0

[59] Water structure and science. http://www.lsbu.ac.uk/water/vibrat.html. Accessed on 6/07/2010.

[60] E. Gazi. PhD thesis, University of Manchester Institute of Science and Technology (UMIST). (2004)

[61] B.G. Tabachnick and L.S. Fidell. Principal components and factor analysis. In: *using Multivariate Statistics.* Pearson: USA, (2001) Chapter 13 p 582-600 ISBN 9780205465255

[62] C. Dytham. The tests 3: tests for data exploration. In: *Choosing and Using Statistics, A Biologist's Guide.* Blackwell Publishing (2003) Chapter 9 p200 ISBN 1-4051-0243-8

[63] R.G Bereton. *Chemometrics Data Analysis for the Laboratory and Chemical Plant.* Wiley. 2003 ISBN 978-0-471-48978-8

[64] Microarray-Analytik, University of Heidelberg. http://www.umm.uni-heidelberg.de/inst/zmf/affymetrix/datenanalyse_e.html. Accessed on 7/7/2010.

Chapter 2: Literature review

Following the introduction to relevant theory in the preceding chapter, biological applications of spectrometric and spectroscopic techniques will be discussed and corresponding literature reviewed. In doing so, this section will aim to provide the rationale behind this study, concluding with aims and objectives.

2.1 FTIR spectroscopic bioanalysis

Fourier transform infrared spectroscopy has undergone intensive research and development into a diagnostic tool, largely due to its high-throughput and non-destructive analysis of a wide range of samples [1]. As explained earlier in section 1.3, the technique relies on the fact that functional groups within a sample will produce spectra specific to those biochemical species. The resulting "fingerprint" can be used to characterize the species present [2]. Through the characterization of biomolecules such as proteins, lipids, carbohydrates and nucleic acids, spectral indicators of diseases such as breast, ovarian and cervical cancer have been found [3].

Predominantly, research into FTIR based disease diagnosis has concentrated on the mid-IR region of around 4000-600 cm^{-1}. This part of the spectrum produces the fundamental vibration, as opposed to the overtone or harmonic, and yields the most information [1]. Within this region there are further subdivisions that can be utilised to study a particular type of molecule more effectively. For example, the 3050-2800 cm^{-1} region is best suited to observe CH_2 and CH_3 stretching vibrations from fatty acids [1].

2.1.1. Cancer diagnosis and FTIR

Early and/or rapid diagnosis of cancer is of utmost importance to ensure therapeutic intervention is most effective. Despite the efficacy of the various available diagnostic modalities – as described in section 1.1.3-, cancer remains a leading cause of death worldwide [4]. Consequently, there is a large impetus behind related investigations. Many FTIR studies have been carried out on DNA,

cell lines and tissues from healthy and diseased volunteers [e.g. 5,6,7]. Discriminations between healthy, benign and malignant ovarian tissues [8]; identifications of micrometastases [9]; and, classifications of cancer cell lines have all been possible with FTIR [10]. The following section will discuss a pertinent selection of these in more detail.

The analysis of various benign and malignant prostate cancer cell lines and tissue samples, by Gazi *et al*., has suggested a method for differentiating between benign and malignant cells [11]. Using the ratio of the peak areas of glycogen (1030 cm^{-1}) and phosphate (1080 cm^{-1}) vibrations, alongside FTIR imaging, this group found it may be possible to map malignancies within tissue [11]. Furthermore, through the use of linear discriminant analysis (LDA) Gazi *et al.* were able to correlate FTIR spectra of prostate cancer biopsies with Gleason grade, and tumour stage [12].

Another separate investigation by Malins *et al.* achieved similar results using slightly different parts of the spectrum. Analysis of the phosphate and C-O of the phosphodiester deoxyribose structure region (1174-1000 cm^{-1}), coupled with weak NH vibrations in the 1499-1310 cm^{-1} region, suggests progression from normal to malignant prostate tissue involves structural changes [7]. Malins *et al.* reported that these spectra were largely a result of prostate DNA, and the mutagenic structural alterations were due to hydroxyl radicals [7]. Subsequently, this group furthered their DNA study to reveal early indicators of tumour formation [13].

Equally as important as identifying cell types are the studies that are able to reveal the utility, efficacy and mechanisms, by which, novel chemotherapeutic agents work [e.g. 14,15,16]. For example, FTIR investigations into oubain – a novel anticancer agent – by Gasper *et al.* have been able to provide vital information about the biochemical signatures expressed following exposure to the drug [15]. More recently, the same group continued by investigating the effects of drug concentration on these chemical signatures [16]. This was

achieved by treating one set of prostate cancer cells with a concentration of oubain that inhibited cell growth by 50% (IC_{50} value) and another at ten times this value [16]. FTIR analysis of the two sets of cells showed different biochemical responses, proving concentration to be an important parameter when attempting to elucidate drug mechanisms [16].

Despite the relevance of literature detailing important cancer cell related studies, it is also important to acknowledge studies into more fundamental aspects of cancer cell biology. To truly make use of such an adaptable technique more detailed metabolomic studies must be done along with further characterization of biomolecules and cellular processes [1,17,18]. A particularly relevant example is the study of the cancer cell cycle; important, not only because of the biochemical changes that occur during maturation, differentiation and development; but also due to morphological changes [19]. Using FTIR microspectroscopy, coupled with principle component and artificial neural network analysis, Boydtson-White and colleagues [20] investigated the HeLa cell cycle. The investigation demonstrated that FTIR spectra can be correlated with a cells biochemical age – previously determined by immunohistochemical staining [20]. This investigation predominantly used changes in the position of the amide I and II bands to classify cell cycle phase. It is likely, however, that chemical changes alone were not responsible for the spectral changes seen here. Spectral artefacts associated with single cell analysis and changes in morphology are more than likely responsible for these differences. This is highlighted by the fact that the group only discussed the 1800-900 cm^{-1} region of their spectra, which would suggest they were unable to correct for these artefacts sufficiently to use the full spectral range. Another potential weakness of their investigation is the co-addition of 64 interferograms, which is low for single cell work using a globar sourced spectrometer. This may have caused unsatisfactory signal to noise ratios, particularly when analysing single cell nuclei. The study discussed later, for example, (see chapter 5) co-added 512 interferograms using a synchrotron sourced spectrometer. Poor signal to noise would lead to a much less robust interpretation of second

derivative spectra as noise is amplified by this process. The group did however employ a smoothing algorithm to attempt to counter this.

It is well known that infrared spectra are subject to influences from physical and biochemical differences. These physical differences can include properties such as density and size [21]. It is important to account for these if one is to recover a true absorption spectrum. Mohlenhoff *et al.* highlighted this problem by demonstrating spectral changes as a result of sample density, in this case, cell nuclei [22]. This group found denser samples exhibited non-Beer-Lambert absorptions, which caused changes in the intensity of the phosphate region of spectra [22]. Such differences could easily be misinterpreted as chemical changes. In this particular case loss of transmission was thought to be responsible, however, nuclei can also cause Mie-type scattering [21]. This phenomenon occurs when the size of the scattering particle is equal to, or slightly smaller than the wavelength of the incident radiation [21]. This results in baseline oscillations in the spectrum and can distort both the intensity and position of absorption bands as shown in figure 2.1 [21]. This problem is compounded further by “anomalous dispersion”; another spectral distortion often seen in spectra of single cells, again due to Mie scattering [21]. Fortunately, algorithms are now becoming available to remove the broad oscillations in the baseline and the dispersion artefact, both of which derive from resonant Mie scattering (figure 2.1) [23]. Probably the first capable of providing reliable absorption spectra is that of Bassan *et al.*, as illustrated in figure 2.1(c) [23].

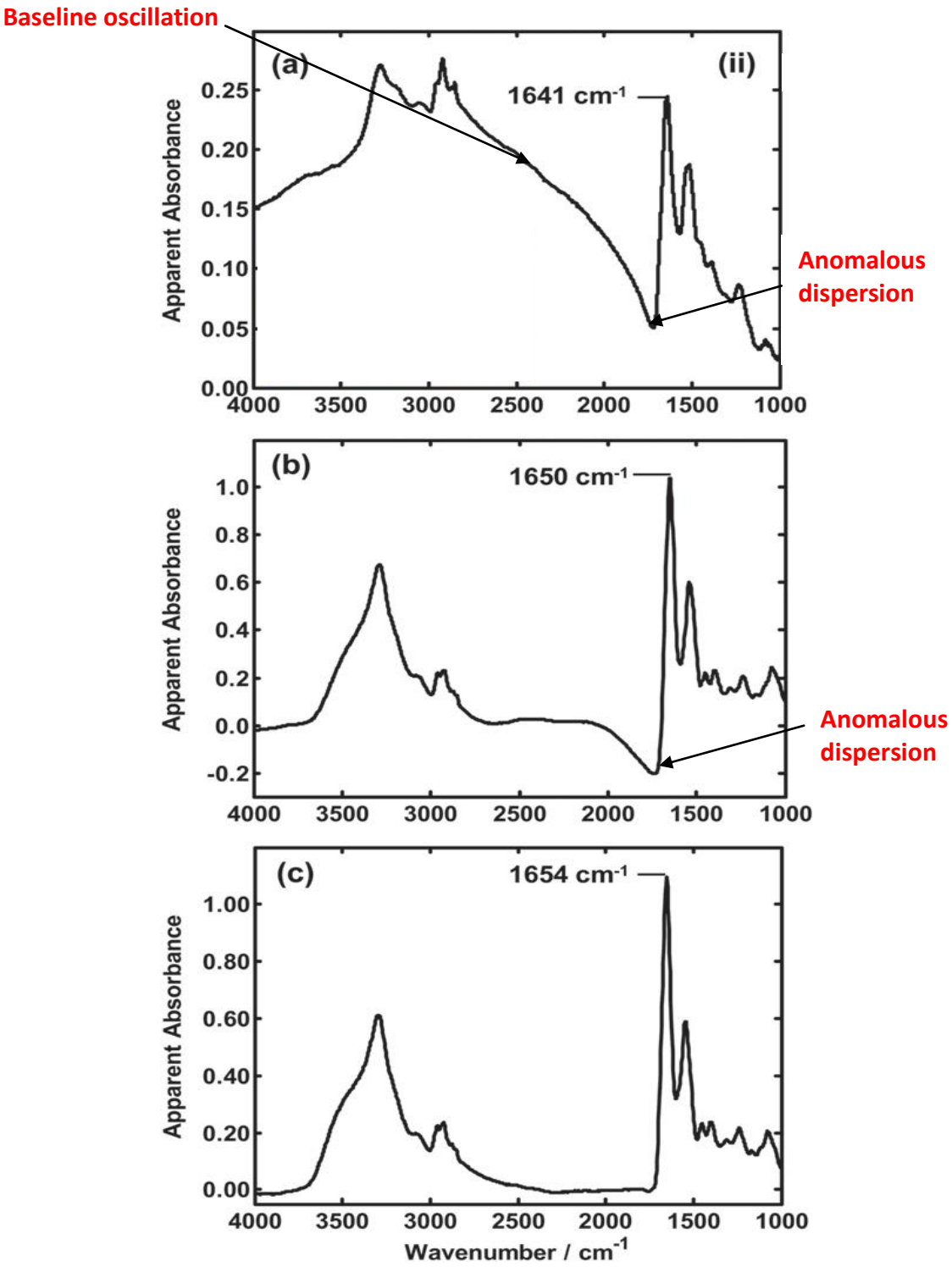

Figure 2.1. IR spectrum of a small cell (a), corrected IR spectrum using old algorithm with anomalous dispersion still present (b) and corrected spectrum using new RMieS-EMSC algorithm (c). Adapted from [23].

2.2 ToF-SIMS analysis of biological specimens

It is important to recognize the many advantages of FTIR, such as: fast, reproducible data acquisition; minimal sample preparation; and, the possibility of a less reductionist, holistic analysis [1]. However, it should also be noted that FTIR is not as sensitive or specific as techniques such as ToF-SIMS; therefore studies involving both techniques, particularly those incorporating the two techniques together [e.g. 6] are of particular personal interest.

The following will concentrate on the analysis of biological cells including novel sample preparation techniques related to cellular analysis; the role of ToF SIMS in biomedical research; and, cancer based studies.

2.2.1 Sample preparation

Time-of flight secondary ion mass spectrometry is capable of elemental and molecular analysis of complex chemistry on the sub-cellular scale [24]. However, the high vacuum requirement of SIMS prevents the analysis of live cells because of their water content. Robust sample preparation protocols are therefore critical in preserving the biochemical architecture of biological samples and extracting meaningful information [25,26,27]. After reviewing much of the literature there appears to be two distinct types of methodology for the preparation of biological samples. These can be broadly classed as drying protocols and frozen hydrated protocols.

Originally developed for SEM studies, drying protocols essentially aim to preserve the biochemical structure of the specimen after water removal, which is unavoidable under high vacuum conditions. These typically involve drying under e.g. argon or freeze drying. Before drying, fixation, either chemically (with e.g. formalin) or physically (by cryofixation), is necessary to prevent the initiation of autolytic pathways and general cell degradation which would be evident in SIMS images as redistributions of diffusible ions e.g. Na^+ and K^+ - discussed later in more detail [25]. Commonly, investigations into drying protocols have tended to centre around optimising the reagents and conditions needed to successfully

preserve the cellular architecture [25,28]. Recently, such studies investigating drying protocols have begun to utilise a combination of complementary techniques to evaluate the effect of each procedure on the cell before SIMS analysis [25]. These include SEM [25,27], fluorescence imaging [26,27] and interference reflection microscopy (IRM) [25] to name a few. Furthermore, there is increasing interest in washing the sample prior to SIMS analysis to remove unwanted inorganic species, as they can lead to ion suppression effects. A multimodal study involving SIMS, SEM and IRM by Malm *et al.* has provided an excellent review of washing steps. The study concluded that an ammonium formate wash prior to cryofixation and freeze drying is most suitable for the general removal of contaminating salts. Additionally, glutaraldehyde fixation may also preserve more fine membrane structures [25]. However, while this study provided an excellent report on relatively gross cellular architecture and chemistry it does not discuss the effect on specific analytes that are present in low concentrations.

Frozen hydrated protocols, have also received a lot of interest possibly due to the fact that chemical fixatives, and the drying procedure, can potentially distort chemical specificity. For example, the cellular cytoplasm can spill out of the cell if dried too intensely [28]. Moreover, analysing the cells frozen retains intracellular water; providing a much more chemically accurate specimen. Yet, the presence of too much atmospheric water can cause problems as ice crystals can form on, and cover, the frozen sample surface – a problem that can be overcome using freeze fracturing [26,27,29]. With this approach surface water is fractured off by freezing the sample between two substrates in liquid nitrogen cooled liquid propane (-185 °C) and then fracturing one off the top to reveal frozen hydrated cells underneath. This can also cause problems as the cells are often randomly torn apart by the fracturing process. Recently, however, a spring-loaded fracture device has been developed for ToF-SIMS to add more reproducibility to the fracture process [29]. In contrast to normal fracture experiments the fracture occurs in the analysis chamber and the top substrate is not discarded so if cells are torn apart the material is not lost [29]. This also

minimises the risk of contamination as the fracture occurs under the ultra high vacuum of the surface analysis chamber [29].

Freeze fracturing has also been well investigated by Chandra *et al*. using dynamic SIMS in combination with SEM and fluorescence microscopy to reveal a high degree of cellular preservation [27]. Interestingly, this study suggests there may be a degree of signal enhancement due to the presence of a thin layer of water, which could further complicate the quantification of cellular chemistry, but also improve yields of analytes present in low quantities. To avoid this, the sample can be dried *in vacuo* after fracturing [27]. It should also be recognised that this particular group pioneered the use of quantifying intracellular potassium, using SIMS, to validate preparatory protocols by determining whether the cell was fixed in a living state [30]. Intracellular potassium can be used to determine whether cells were fixed in the living state because the potassium/sodium gradient across the cell membrane is maintained at around 10:1 with active ion pumping. Therefore, the detection of higher levels of potassium inside the cell would indicate fixation of the cell in a living state [30].

From the literature, it is apparent that the optimum preparation protocol probably depends on the nature of the sample, the type of instrument used, and the aim of the analysis. For example, 70% ethanol fixation can be used to remove lipid membranes and expose intracellular proteins for analysis, if required [28]. Furthermore, for all diffusible ion localization studies, strict cryogenic practices are most appropriate [25]. As previously shown, various different preparation protocols have been adopted [25,26,27,28,29]. However, none, as yet, have been reported for the preparation of non-adherent cells directly from suspension.

2.2.2 ToF-SIMS in biomedical research

The development of the polyatomic primary ion source, as previously described in section 1.2.3, increased the amount of information obtainable from the high mass end of spectra of organic analytes from whole cells. Consequently, ToF-

SIMS was adopted into the field of lipid research and has been successfully used, for example, to localize sphingomyelin within cholesterol domains in membrane monolayers [31]. Furthermore, Ostrowski *et al*. [32] and Kurczy *et al.* [33] suggest that ToF-SIMS can be used to investigate physical changes in membrane structure. For the purpose of this review however, which - as previously stated - will concentrate on studies of whole cells, more detailed explanations of membrane studies can be found elsewhere: Prinz *et al*. [34]; Ostrowski *et al.* [35]; Heien *et al.* [36] etc.

An important drug-cell interaction based study involved the use of *Candida glabrata* – a type of yeast commonly present in human infections – to investigate clofazimine [40]. Used as a strong antibiotic, the investigation was aimed at determining as to where clofazimine would interact with the cell. The group used a 15 KeV Au^+ primary ion beam to analyse frozen hydrated, clofazimine doped cells. They found that clofazimine (m/z 473-475$^+$) was present in the spectra of cells whose cell walls were complete, i.e. unfractured (figure 2.2). This was determined by localizing ions indicative of the cell wall, such as the head group of the membrane phospholipid dipalmatoyl-phosphatidylcholine (DPPC) (m/z 184$^+$) [40].

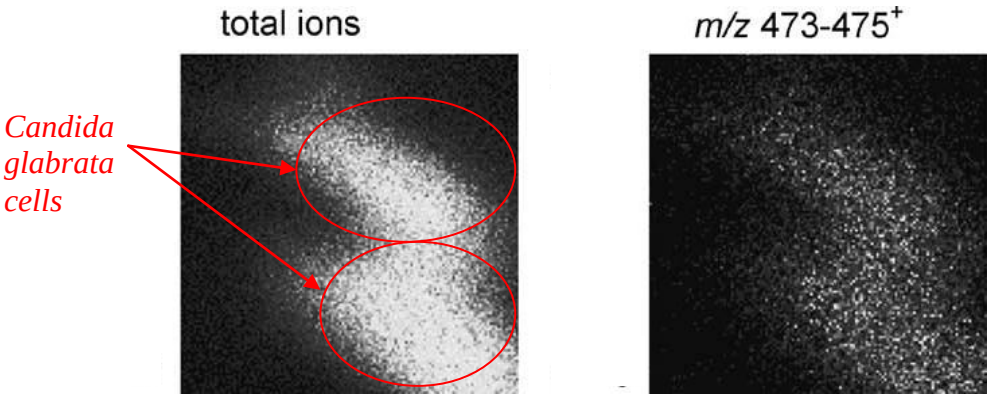

Figure 2.2. Localization of clofazimine (40 µm X 40 µm field of view). Adapted from [41].

It was, therefore, concluded that clofazimine was retained by the cell wall. This was attributed to chitin, a biosorptive molecule, well known for interacting with chlorinated compounds - like clofazimine [41].

2.2.2.1 ToF-SIMS in cancer research

Today, through extensive research, SIMS is becoming an important tool; not only for the development of novel chemotherapeutic agents, but also for the diagnosis and prognosis of cancer. Much of the literature pertaining to this area - as with the previously discussed biomedical applications - describes the use of SIMS to map certain ions within cancer cells or tissue sections. However, increasingly, studies are focussing on the use of multivariate, interdisciplinary techniques to characterize the various cellular differences associated with carcinogenesis.

A significant part of the literature on this subject has been provided from dynamic SIMS studies. A particularly active group in this area; Chandra and colleagues have provided the basis for many of the more recent investigations. After adapting various cryogenic techniques to SIMS [42], they have been able to productively apply dynamic SIMS to cancer research. Investigations of various inorganic ions, in cancerous (MCF-7) and normal (MCF-10A) breast cell lines, revealed differences in the ratios of nuclear and cytoplasmic calcium concentrations [43]. Following this, as part of the same investigation, the same group then progressed on to investigate cellular distributions of calcium after drug treatment [43].

More relevant to this particular report, however, are static SIMS studies. Through this method atomic, and, molecular information can be obtained, which is extremely useful when identifying biological compounds within cellular systems. In a similar way to Chandra and colleagues etc, Chehade *et al.* employed ToF-SIMS to examine the biodistribution of a radioactively labelled drug, which targeted melanoma cells [44]. They were able to localize the drug to the cytoplasm of melanoma cells, tumour infiltrating macrophages and normal melanocytes.

Quong *et al.* investigated genotoxic heterocyclic amines - produced during certain cooking methods [45]. The most important of these amines is 2-amino-1-

methyl-6-phenylimidazo[4,5-*b*]pyridine (PhIP). The group was able to analyse the distribution of this carcinogen in human breast cancer cells; using ToF-SIMS and a dye, specific to the outer leaflet of the cell membrane, to do so [45]. This particular study was heavily reliant on the ability of ToF-SIMS to obtain molecular information, specifically, from large membrane molecules. Furthermore, and more importantly, Fartmann *et al.* demonstrated the ability of static SIMS to examine molecular distribution, without the addition of dyes or isotopic labels [46].

Recently, and most interestingly, ToF-SIMS was applied to investigate the effects of hederacolchiside A1 (Hcol-A1) – a novel chemotherapeutic agent [47]. The group utilized a range of techniques to assess the ability of Hcol-A1 to permeabilize human melanoma cell membranes. Principally, ToF-SIMS was used to monitor the interaction of the compound with cholesterol and phospholipids. Through the use of imaging ToF-SIMS, the group illustrate the destruction of the cell after prolonged Hcol-A1 exposure (figure 2.3); imaging cholesterol ions, Hcol-A1 ions, and phospholipid ions, to do so (figure 2.3)[47].

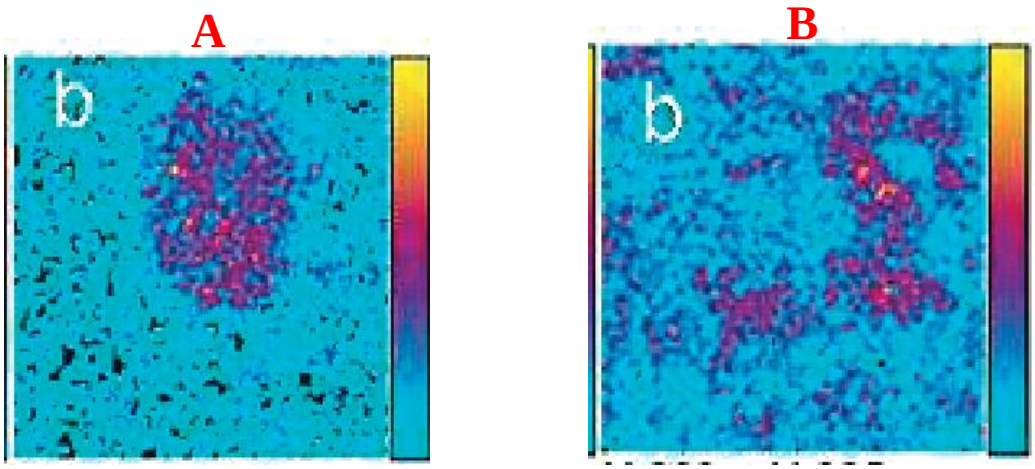

Figure 2.3. Cholesterol ion images showing the intact (A) and disrupted (B) cell. Adapted from [47].

This study was of particular personal interest; not only because it used a novel interdisciplinary approach to assess as to the efficacy of Hcol-A1 as a permeabilizing agent; but, also as it provides a good illustration of the successful

localization of various membrane components, in the presence of an added chemical - which is of great relevance to the present study.

Finally, ToF-SIMS has been used to investigate the molecular composition of normal and cancerous cell lines [48]. From this, valuable information regarding the natural history of the disease and metastasis has been obtained. One particular group used the technique to discriminate between malignant and non-malignant prostate cancer cells [49]. Baker *et al.* utilised three prostate cancer cell lines: PC-3, LNCaP and PNT2-C2 - the latter being the non-malignant example [49]. A 40KeV C_{60}^{+} primary ion beam was used for the analysis to generate 135 spectra. The complexity of the spectral signatures associated with biological materials, as mentioned previously, is widely known. Interpretation of their spectra was, therefore, aided by chemometric analysis. Subsequently, the greatest mass spectral differences were rapidly identified [49]. Due to the non-destructive nature of static SIMS, the group were able to discriminate the cell lines according to the phospholipid contents of their cell membranes [49]. This was then illustrated using Principal Component-Discriminant Function Analysis (PC-DFA) (figure 2.4).

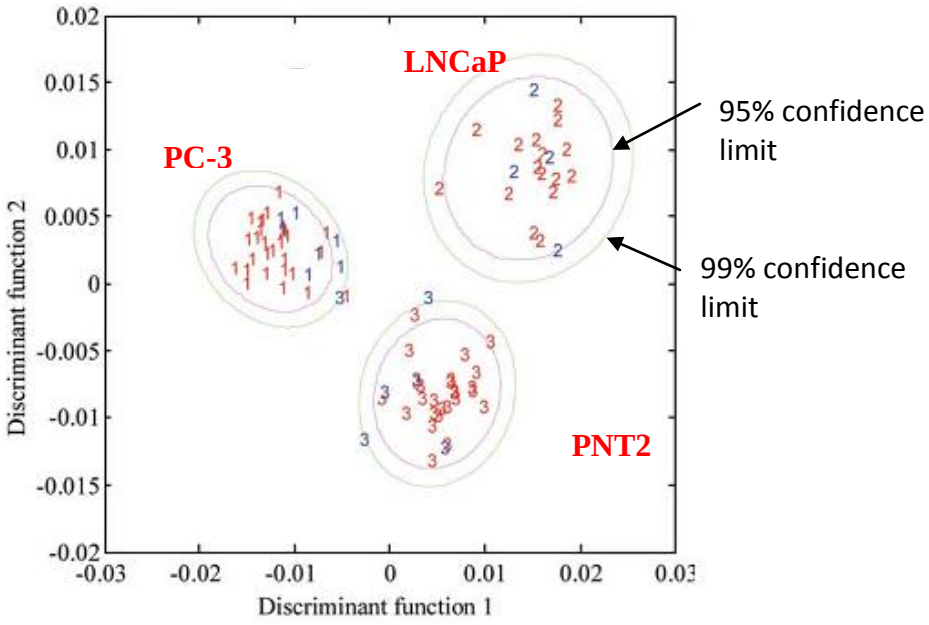

Figure 2.4. Discriminant function projection plot showing PC-3, LNCaP and PNT2 cell lines (red = training set, blue = test set). Adapted from [49].

It is clear from the literature that both ToF-SIMS and FTIR are capable of becoming valuable tools for the pathologist. It is important to recognize the strengths and weaknesses of both FTIR and ToF-SIMS. Through this recognition it is hoped the techniques can be used further to complement each other as in [6,48]. Furthermore, both supervised (using a known training set to help classify data) and unsupervised chemometric techniques can be used to successfully aid analysis, as demonstrated by Baker *et al.* [49].

2.3 Other related analytical techniques

Mass spectrometry and vibrational spectroscopy, in their various different guises, are complex, yet accurate means of quantifying and identifying biological entities. The following project focuses on the use of ToF-SIMS and FT-IR for bioanalysis; nevertheless, it is important to briefly recognize the range of similar techniques available and their associated bioanalytical studies.

2.3.1 Fast atom bombardment mass spectrometry (FAB-MS)

Fast atom bombardment (FAB) studies have provided a wealth of fundamental information on biochemicals [e.g. 50,51,52]. The technique, first developed by Barber *et al.* involves focussing a KeV atom beam (typically Ar or Xe) onto a sample, which, must be dissolved in a suitable liquid matrix, such as glycerol [53]. The matrix is usually a non-volatile, inert solution, used to absorb most of the energy imparted by the beam of atoms. As the matrix is bombarded, clusters of the matrix and sample are released from the surface resulting in the formation of ions. As the sample is in a liquid the surface is essentially replenished in analyte continuously because it mixes as the beam hits it. Use of the liquid matrix in this way makes imaging tissue and cells difficult as the sample should be liquid. Liquid matrix applied to tissue would cause the redistribution of surface chemical species. Furthermore, a large amount of background signal is detected from the matrix, which would further compound analysis of lower molecular weight analytes.

As an analytical tool, FAB was the first to be successful for the mass spectrometric analysis of macromolecules, such as lipids [51] and amino acids

[54]. Cancer based studies, using FAB, are again generally based around the characterization of biological analytes. For example, FAB-MS has been used to characterize novel peptide hormones present during lung cancer [55]. The ability of FAB to detect small and large molecules has enabled researchers to detect small structural changes in peptide hormones and is often used in the diagnosis of lung cancer [55]. In a similar way, the technique has also been applied to study androgens, which are thought to play a large role in prostate cancer proliferation [56]. However, as stated earlier, the technique is hampered by the necessary addition of a matrix; a problem which has been largely solved by the introduction of electrospray ionization [1].

2.3.2 Electrospray

Electrospray (see [57]), like many of the mass spectrometric techniques, has often been used for the classification of biocompounds [e.g. 58]. This method is of great importance as there is no need for a matrix, or vacuum, which allows for relatively undisturbed analysis. More recently, desorption electrospray ionization (DESI) in particular, has been gaining popularity. Essentially combining both desorption ionization and electrospray ionization, DESI generates ions using charged micro-droplet bombardment at atmospheric pressure [59]. Through the impact of the "spray", microscopic liquid layers are formed, in which, the analyte dissolves [59]. Following this, desorption occurs through energy transfer, which occurs *via* collisions between droplets and the newly formed liquid layers. In this way, the dissolved analyte is forced into the gas phase, and, through heating, produces free gas-phase ions [59].

As an ambient MS method, DESI has the capacity for extremely high-throughput analysis, thus making it ideal for clinical applications. The methodology has successfully been used to investigate lipid distributions in metastatic human-liver adenocarcinoma [59]; and, image lipids and drug molecules within healthy rat brain [60]. However, despite offering ambient surface sampling without pre treatment, low spatial resolution due to large spot size of the spray (>150 μm) makes it less favourable than SIMS or MALDI.

2.3.3 Matrix assisted laser desorption/ionization (MALDI)

A soft ionization technique, MALDI functions by interrogating a co-crystallized sample and matrix with a laser (e.g. UV 337nm). The energy transfer, from the laser to the matrix, results in the sample's transition from solid to gas phase. In this gas phase, the analyte is then ionized by gaining energy from the matrix.

MALDI has become one of the most important techniques involved in biomedical analysis. Furthermore, the methodology is unrivalled in its ability to classify proteins, polymers and amino acids [1]. The introduction of commercially available systems for molecular imaging has facilitated the production of many proteomic studies [61]. The majority of these investigations have been based around imaging proteins and peptides associated with various pathologies [62,63].

Again, the greatest hindrance of MALDI is the need for a matrix, making it difficult to analyse low molecular weight compounds (<500 m/z) and poorer image resolution than SIMS (2-25 µm). Considerable effort has developed a pre-existing "matrix free" technique known as LDI (laser desorption/ionization). It is thought that, in a similar way to MALDI, this technique will become of great proteomic, metabolomic and lipidomic significance but will have limitations for intact macromolecular analysis due to the lack of matrix [1].

2.3.4 Raman spectroscopy

Raman spectroscopy is essentially a measure of energy exchange between a molecule and electromagnetic radiation. From this exchange a shift in the wavelength of the incident light is observed [64]. This measurable shift was first reported by Raman and Krishnan [65] and is now known as the Raman shift, also termed as inelastic light scattering.

The use of Raman spectroscopy with multivariate statistics has shown great promise in terms of biomedical applications. Chemical dissimilarities between precancerous and normal tissues [e.g.66,67]; and, normal and malignant tissues

[e.g. 68] have been observed using Raman to name a few. Most importantly, Raman spectroscopy is not affected by the presence of water as visible lasers are used so no light is absorbed, unlike infrared radiation which is strongly absorbed by water. This has allowed for the analysis of biofluids and even measurements *in vivo* [e.g.66,67,69]. However, there are ongoing problems associated with low signal intensity with as few as 1 in 10^6-10^8 photons experiencing the Raman shift. Many biological samples also produce fluorescence that can render a spectrum useless. Fortunately, signals can be improved by using a laser wavelength that lies under a strong electronic absorption band of a chromophore. This causes resonance enhancement, which increases some band intensities by 10^5. Spectra can also be corrected mathematically to remove fluorescence, which is already significantly reduced at this wavelength [1]. Finally, surface enhanced Raman spectroscopy can produce equal improvements by placing the analyte on a roughened metal surface. In this case the enhancement is either caused by electromagnetic or chemical interactions, however the exact mechanism is still unknown.

2.4 Aims and Objectives

Previously, biological SIMS analysis has focussed mainly on cell cultures grown on SIMS-compatible substrates [e.g.49], or on tissue sections [e.g.6]. Ideally, however, samples should be analysed as close to their native state as possible. It is believed that the surface chemistry of the substrate may cause changes in the cell's natural biochemistry [70,71]. The following study aims to bypass this issue as cells will be grown on relatively inert culture dishes and then cytospun onto substrates. The use of cytospinning as a preparatory technique for ToF-SIMS has not, as yet, been reported. Consequently, any information about cellular chemistry of samples produced in this way will be important for future investigations. Furthermore, and most importantly, a comprehensive study of cytospinning as a novel preparatory method will provide an invaluable starting point for other similar investigations. For example, cells grown directly in suspension have not been analysed with SIMS due to sample preparation issues. Cytospinning, however, would allow for the preparation of viable samples. It

would therefore be interesting to compare adherent and non-adherent cell line based studies.

This study will aim to provide a systematic evaluation of cytospinning based techniques for the preparation of biological cells and nuclei, directly from suspension for ToF-SIMS analysis. Adherent cell lines were used in this particular investigation as they are well characterised and the literature surrounding them will provide a detailed guide throughout the investigation, against which, it will be possible to compare data and evaluate progress. This will be largely achieved through comparisons with existing air drying [e.g. 25] and freeze drying [e.g. 26,27] protocols – as reviewed in section 2.2.1. Furthermore, prior to ToF-SIMS analysis complementary techniques of fluorescence imaging and SEM will be used to visually examine cellular architecture. Additionally, cytospun samples will be freeze fractured to assess whether the two techniques are compatible for the analysis of frozen hydrated samples.

After establishing an optimal preparatory protocol the influence of the various phases of the cell cycle on ToF-SIMS and FT-IR spectral data will be studied. Investigating the cell cycle using FT-IR is not novel alone as several groups have reported similar investigations [19,20,72], however, until now physical effects of sample morphology have compounded investigations, as discussed in section 2.1. This investigation will use a novel correction algorithm to reliably separate physical effects from chemical differences. This will provide genuine chemical information by revealing true absorption spectra for the first time in such an investigation. The use of complementary ToF-SIMS data will help to validate this by providing further chemical information. Furthermore, the results will indicate whether ToF-SIMS can detect surface biochemical changes induced by the cell cycle, and importantly, the extent to which this influences the classification of different cell types. This will add to the novelty of the study as no SIMS investigations into the main phases of the cell cycle are known and little is known about changes in the cell surface chemistry during cell proliferation. To do this, a number of cancerous cell types in G1, S and G2/M growth phases will

be separated by FACS (fluorescence activated cell sorting) and anticancer drug-induced cell cycle arrest. These fractions will then be subjected to ToF-SIMS and FT-IR analysis.

Having characterised the cell cycle the same cancer cell line will then be treated with a novel anticancer agent. Prior knowledge of chemical signatures associated with the different phases of the cell cycle will allow for the identification of the phase, in which, the novel drug causes cell cycle arrest whilst providing valuable chemical information. Furthermore, imaging SIMS will be used to help localise the drug. Whilst it is beyond the capabilities of such an investigation to completely elucidate the mechanisms of the novel anticancer agent, it will serve to provide vital information that may enable this in the future.

In summary the project will aim to:

- Validate an optimum sample preparation method for ToF-SIMS analysis of non-adherent cell lines.
- Investigate the effect of the cell cycle and assess chemical differences between the different phases using ToF-SIMS and FT-IR spectroscopy.
- Use this information to investigate the influences of a novel anticancer agent on ovarian cancer cells.

References

[1] D. Ellis, W.B. Dunn, J.L. Griffin, J.W. Allwood and R. Goodacre. *Pharmacogenomics*. 8 (2007) p1243-1266

[2] C.P.S. Hsu. Infrared spectroscopy. In: *The handbook of instrumental techniques for analytical chemistry*. Prentice Hall (1997) Chapter 15 p247-283. ISBN 0131773380

[3] H. Fabian, N.A.N Thi, M. Eiden, P. Lasch, J. Schmitt and D Naumann. *Biochimica et biophysica acta*. (2006) p874-882

[4] Government statistics, http://www.statistics.gov.uk/CCI/nugget.asp?ID=861&Pos=2&ColRank=1&Rank=160. Visited on 08/07/2010.

[5] D.C. Fernandez, R. Bhargava, S.M. Hewitt, I.W. Levin. *Nature biotechnology*. 23 (2005) p469-474

[6] E. Gazi, J. Dwyer, N. Lockyer, P. Gardner, J.C. Vickerman, J. Miyan, C.A. Hart, M. Brown, J.H. Shanks and N. Clarke. *Faraday discussions*. 126 (2004) p41-59

[7] D.C. Malins, N.L. Polissar and S.J. Gunselman. *Proceedings of the national academy of sciences*. 94 (1997) p259-264

[8] C.M. Krishna, D.G. Sockalingum, R.A. Bhat, L. Veneteo, P. Kushtagi, M. Pluot and M. Manfait. *Analytical and bioanalytical chemistry.* 387(5) (2007) p1649-1656

[9] C. Krafft, L. Shapoval, S.B. Sobottka, K.D. Geiger, G. Scharkert and R. Salzer. *Biochimica and biophysica acta – biomembranes*. 1758 (7) (2006) p883-891

[10] E. Njoroge, S.R. Alty, M.R. Gani, and M. Alaktib. *Annual international conference of the IEEE engineering in medicine and biology –proceedings.* (2006) p5338-5341 art.no. 4029268

[11] E. Gazi, J. Dwyer, P. Gardner, A. Ghanbari-Siahkali, A.P. Wade, J. Miyan, N.P. Lockyer, J.C. Vickerman, N.W. Clarke, J.H. Shanks, L.J. Scott, C.A. Hart and M. Brown. *Journal of pathology*. 201 (2003) p99-108

[12] E. Gazi, M. Baker, J. Dwyer, N.P. Lockyer, P. Gardner, J.H. Shanks, R.S. Reeve, C.A. Hart, N.W. Clarke and M.D. Brown. *European urology.* 50 (2006) p750-761

[13] D.C. Malins, K.M. Anderson, N.K. Gilman, V.M. Green, E.A. Barker and K.E. Hellstrom. *Proceedings of the national academy of sciences.* 101 (2004) p10721-10725

[14] J. Sule-Suso, D. Skingsley, G.D. Sockalingum *et al. Vibrational spectroscopy.* 38 (2005) p179-184

[15] R. Gasper, J. Dewelle, R. Kiss, T. Mijatovic and E. Goormaghtigh. *Biochimica et biophysica acta*. 1788 (2009) p1263-1270

[16]R. Gasper, T. Mijatovic, R. Kiss, E. Goormaghtigh. *Spectroscopy*. 24 (2010) p45-49

[17]H.H. Mantsch, L.P. Choo-smith, R.A. Shaw. *Vibrational spectroscopy.* 30 (2002) p31-41.

[18] M. Diem, S. Boydston-White and L. Chiriboga. *Applied spectroscopy*. 53 (1999) 148A-161A

[19] S. Boydston-White, T. Chernenko, A. Regina, M. Milikovic, C. Matthaus and M. Diem. *Vibrational spectroscopy*. 38 (2005) p169-177

[20] S. Boydston-White, M. Romeo, T. Chernenko, A. Regina, M. Milikovic and M. Diem. *Biochmica et biophysica acta*. (2006) 908-914

[21] P. Bassan, H.J. Byrne, F. Bonnier, J. Lee, P. Dumas and P. Gardner. *Analyst*. 134 (2009) p1586-1593.

[22] B. Mohlenhoff, M. Romeo, M. Diem and B.R. Wood. *Biophysical journal*. 88 (2005) p3635-3640

[23] P.Bassan, A. Kohler, H. Martens, J. Lee, H.J. Byrne, P. Dumas, E. Gazi, M. Brown, N. Clarke and P. Gardner. *Analyst*. 135 (2010) p268-277

[24] D.Breitenstein, C.E. Rommel, J. Stolwijk, J. Wegener, B. Hagenhoff. *Applied Surface Science.* 255 (2008) p1249-1256.

[25] J. Malm, D. Giannaras, M. O Riehle, N. Gadegaard, and P. Sjövall. *Analytical chemistry.* (2009) ; doi: 10.1021/ac900636v

[26] T.L. Colliver, C.L. Brummel, M.L. Pacholski, F.D. Swanek, A.G. Ewing and N. Winograd. *Analytical Chemistry*. 69 (1997) p2225-2231

[27] S.Chandra. *Applied Surface Science* 255 (2008) p1273-1284.

[28] E.S.F. Berman, S.L. Fortson, K.D. Checchi, L. Wu, J.S. Felton, K.J.J. Wu and K. S. Kulp. *Journal of the American society for mass spectrometry.* 19 (2008) p1230-1236

[29] I. Lanekoff, M.E. Kurczy, R. Hill, J.S. Fletcher, J.C. Vickerman, N. Winograd, P. Sjovall and A.G. Ewing. *Analytical Chemistry.* 82 (2010) p6652-6659

[30] S. Chandra and G.H. Morrison. *International journal of mass spectrometry - ion processes*. 143 (1995) p161-176

[31] C.M. McQuaw, L. Zheng, A.G. Ewing and N. Winograd. *Langmuir*. 10 (2007) p5645-5650

[32] S.G. Ostrowski, C.T. Van Bell, N. Winograd and A.G. Ewing. *Science*. 305 (2004) p71-73

[33] M.E. Kurczy, P.D. Piehowski, C.T. Van Bell, M.L. Heien, N. Winograd and A.G. Ewing. *Proceedings of the national academy of sciences of the United States.* 107 (2010) p2751-2756

[34] C. Prinz, F. Hook, J. Malm and P. Sjovall. *Langmuir*. 23 (2007) p8035-8041

[35] S.G. Ostrowski, M.E. Kurczy, T.P. Roddy, N. Winograd and A.G. Ewing. *Analytical Chemistry*. 79 (2007) p3554-3560

[36] M.L. Heien, P.D. Piehowski, N. Winograd and A.G. Ewing. Lipid detection, identification, and imaging single cells with SIMS. In: *Mass Spectrometry Imaging: Principles and Protocols*. Human Press Inc (2010) Chapter 4 p85-97. ISBN 9781607617457(H).

[37] J.P. Berry, F. Escaig, F. Lange and P. Galle. *Laboratory investigation*. 55 (1986) p109-119

[38] J. Clerc, C. Fourre and P. Fragu. *Cell biology international.* 21 (1997) p619-633

[39] S. Chandra and G.H. Morrison. *Journal of microscopy*. 188 (1997) p182-190

[40] B. Cliff, N.P. Lockyer, C. Corlett and J.C. Vickerman. *Rapid communications in mass spectrometry.* 17 (2003) p2163-2167

[41] N.P. Lockyer and J.C. Vickerman. *Applied surface science*. 11 (2004) p377-384

[42] S. Chandra, M.T. Bernius, G.H. Morrison. *Analytical Chemistry* 58 (1986) p493-496

[43] S. Chandra and D.R. Lorey 2nd. *Cell molecular biology*. 47 (2001) p503-518

[44] F. Chehade, C. De Labriolle-Vaylet, N Moins, M.F. Moreau, J. Papon, P. Labarre, P. Galle, A. Veyre and E. Hindie*. Journal of nuclear medicine.* 46 (2005) p1701-1706

[45] J. N. Quong, M.G. Knize, K.S. Kulp and K.J. Wu. *Applied surface science*. 231-232 (2004) p424-427

[46] M. Fartmann, S. Dambach, C. Kriegeskotte, H.P. Wiesmann, A. Wittig, W. Sauerwein, D. Lipinsky and H.F. Arlinghaus. *Surface and interface analysis.* 34 (2002) p63-66

[47]G.D. Mazzucchelli, N.A. Cellier, V. Mshviladzade, R. Elias, Y. Shim, D. Touboul, L. Quinton, A. Brunelle, O. Laprevote, E.A. De Pauw and M.A. De Pauw-Gillet *Journal of proteome research.* 7 (2007) p1683-1692

[48] E. Gazi, N.P. Lockyer, J.C. Vickerman, P. Gardner, J. Dwyer, C.A. Hart, M.D. Brown, N.W. Clarke and J. Miyan. *Applied surface science* 231-232 (2004) p452-456

[49] M.J. Baker, M.D. Brown, E. Gazi, N.W. Clarke, J.C. Vickerman and N.P. Lockyer. *The analyst.* 133 (2008) p1-6

[50] E. Ayanoglu, A. Wegmann, O. Pilet, G.D. Marbury, J.R. Hass and C. Djerassi. *Journal of the American chemical society.* 106 (1984) p5246-5251

[51] J.P. Lehman, C. Fenselau and J.R. DePaulo. *Drug metabolism and disposition.*11 (1983) p221-225

[52] T. Matsubara and A. Hayashi. *Progress in lipid research.* 30 (1991) 301-322

[53] M. Barber, R.S. Bordoli, D. Sedgwick and A.N. Tyler. *Journal of the chemical society – chemical communications*. 7 (1981) p325-327

[54] D.H. Chace, S.L. Hillman, D.S. Millington, S.G. Kahler, C.R. Roe, E.W. Naylor. *Cinical chemistry.* 41 (1995) p62-68

[55] A.M. Treston, A.L. Yergey, P.G. Kasprzyk, F. Cuttitta and J.L. Mulshine. Application of mass spectrometry to the identification of novel peptide hormones involved with lung cancer biology. In: *Biology of lung cancer: diagnosis and treatment*. Marcel Dekker inc. (1988) Chapter 4. p91-120. ISBN 0-8247-7642-9

[56] J. Belanger, B.A. Lodge, J.R. Pare and P. Lafontaine. *Journal of pharmaceutical and biomedical analysis*. 3 (1985) p81-86

[57] J.B. Fenn, M. Mann, C.K. Meng and S.F. Wong. *Nature biotechnology.* 23 (2005) p469-474

[58]S.B. Milne, P.T. Ivanova, D. DeCamp, R.C. Hsueh. *Journal of lipid research.* 46 (2006) p1796-1802

[59] J.M. Wiseman, S.M. Puolitaival, Z. Takats, R.G. Cooks and R.M. Caprioli. *Angewandte chemie international edition.* 44 (2005) p7094-7097

[60] J.M. Wiseman, D.R. Ifa, Q.Y. Song and R.G. Cooks. *Angewandte chemie international edition.* 45 (2006) p7188-7192

[61] J.M. Wiseman, R.I. Demian, A. Venter and R.G. Cooks. *Nature Protocols. 3* (2008) p517-524

[62] M. Stoeckli, P. Chaurand, D.E. Hallaham and R.M. Caprioli. *Nature medicine.* 7 (2001) p493-496

[63] P. Chaurand, S.A. Schwartz, M.L. Reyzer and R.M. Caprioli. *Toxicologic pathology*. 33 (2005) p92-101

[64] J.R. Ferraro, K. Nakamoto and C.W. Brown. Basic theory. In: *Introductory Raman spectroscopy*. Elsevier science. (1994) Chapter 1. p1-66. ISBN 0-12-254105-7

[65] C.V. Raman and K.S. Krishnan. *Nature*. 121 (1928) p501-502.

[66] U. Utzinger, D.L. Heintzelman, A. Mahadevan-Jansen, A. Malpica, M. Follen and R. Richards-Kortumt. *Applied spectroscopy*. 55 (2001) p955-959

[67] A. Mahadevan-Jansen, M.F. Mitchell, N. Ramanujam, A. Malpica, S. Thomsen. U. Utzinger and R. Richards-Kortumt. *Photochemistry and photobiology.* 68 (1998) p123-132

[68] P. Crow, A. Molckovsky, N. Stone, J. Uff, B. Wilson, L.M. Wongkeesong. *Urology*. 65 (2005) p1126-1130

[69] M.G. Shim and B.C. Wilson. *Journal of Raman spectroscopy*. 72 (2000) p3771-3775.

[70] B.G. Keselowsky, D.M. Collard and A.J. Garcia. *Applied biological sciences*. 102 (2005) p5953-5957

[71] A.D. Meade, F.M. Lyng, P. Knief and H.J. Byrne. *Analytical and bioanalytical chemistry*. 387 (2007) p1717-1728

[72] H.N. Holman, M.C. Martin, E.A. Blakely, K. Bjornstad and W.R. McKinney. *Biopolymers (biospectroscopy)*. 57 (2000) p329-335

Chapter 3: Instrumentation

The subsequent chapter will discuss the important features of the instrumentation used throughout this investigation. A custom built Time-of-flight secondary ion mass spectrometer, based in the Manchester Interdisciplinary Biocentre, was used for all SIMS experiments. Synchrotron sourced infrared studies were conducted in France and Italy at international synchrotron facilities. Visits to these sites were fully funded by the EU.

3.1 Time of flight secondary ion mass spectrometry (ToF-SIMS)

The Bio-ToF-SIMS instrument (figures 3.1 and 3.2), used throughout the following investigation, has been highly optimised for the analysis of biomolecules [1]. The result of a collaboration between Pennsylvania State University, The University of Manchester Institute of Science and Technology (UMIST) and Kore Technology, the Bio-ToF has good mass resolution (~2000), high sensitivity (ppm) and a large field of view (1mm) [1]. Furthermore, the Bio-ToF has cryogenic sample handling facilities, a choice of either Au or C_{60} primary ion guns and a post acceleration detector.

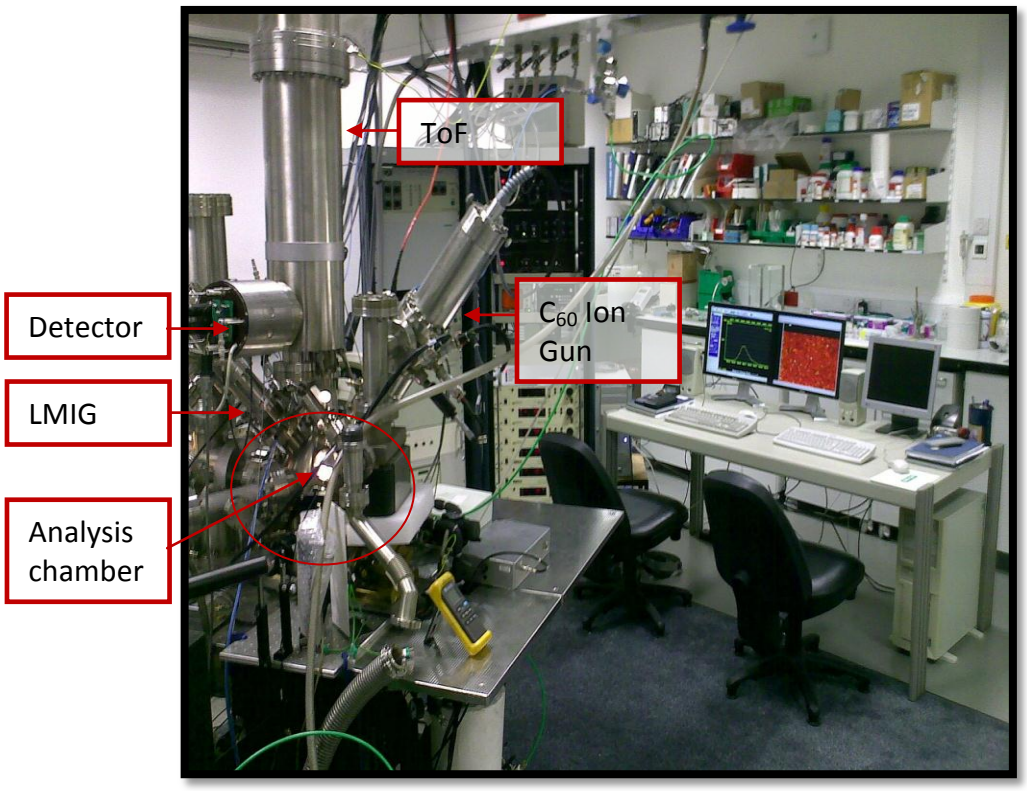

Figure 3.1. The Bio-ToF SIMS instrument (back) and control units.

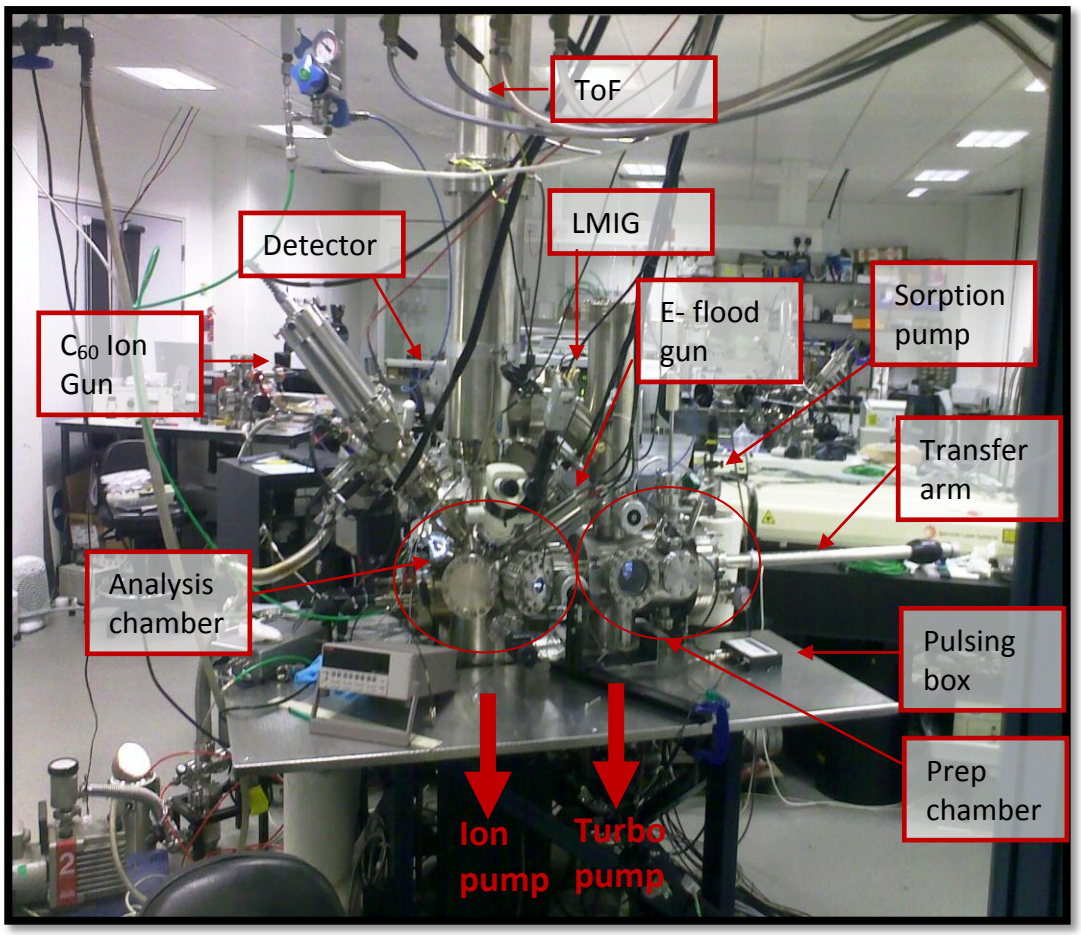

Figure 3.2. The Bio-ToF-SIMS instrument (front).

The Bio-ToF-SIMS instrument consists of five major components: (i) a fast entry port and sample preparation chamber; (ii) a surface analysis chamber; (iii) a cryogenic sample stage; (iv) a liquid metal ion gun, C_{60} ion gun and electron flood gun; and, (v) a secondary ion extractor and detector [2]. The following chapter will provide a brief description of the instrument, focussing on these important parts. For a more detailed explanation of the instrumentation see Vickerman [1] and Braun *et al.* [2].

3.1.1 Fast entry port and prep chamber

To rapidly introduce samples into the high vacuum environment (*ca* 1 x 10^{-8} Torr) – maintained by a turbomolecular pump – a two stage entry system is employed [2]. The first part of this system consists of a small chamber (*ca* 3 x 10^{-3} Torr) – evacuated by a sorption pump – into which, the sample "stub" (figure 3.3) can be placed using a shrouded receptacle [2]. The second part of the system is accessed through a gate valve, via the previously described chamber,

thus preventing loss of high vacuum. This second chamber, known as the prep chamber, contains a transfer arm, onto which, the sample "stub" can be attached.

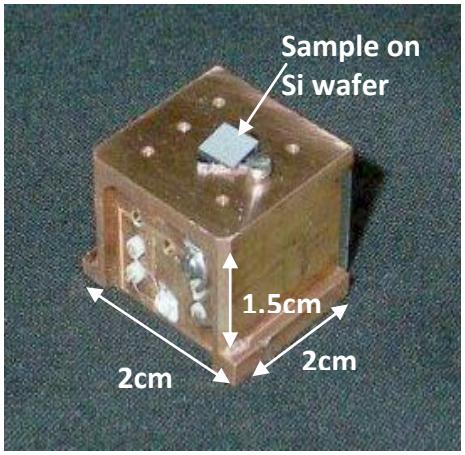

Figure 3.3. The copper sample stub with a sample ready for freeze fracture. Adapted from [3].

Once housed within the prep chamber, it is possible to transfer the sample onto a liquid nitrogen cooled freeze fracture arm. Here it can either be stored, or, freeze fracturing (as described in chapter 1) can be done. Alternatively, the sample can be transferred directly into the surface analysis chamber and onto the sample stage.

3.1.2 Surface analysis chamber and sample stage

The surface analysis chamber houses the sample stage at *ca* 1.5 x 10^{-9} Torr maintained by an ion pump. A channel electron multiplier, above the sample, detects secondary electrons allowing for gun tuning and focussing prior to experiments. Additionally, secondary electron images, analogous to scanning electron microscopic images can be obtained [2]. An optical microscope allows for visual inspection and alignment and a low energy electron gun for charge compensation (discussed later).

The sample stub is mounted horizontally inside the surface analysis chamber on the sample stage, which is positioned in such a way that the sample is aligned with the ion guns and extraction optics [2]. The stage can be moved in the X and Y positions using two, high precision micrometers. Additionally, the sample

height can be adjusted to accommodate samples of various heights. This is important as ToF-SIMS data are sensitive to sample height because alterations in the z position (height) effectively change the length of the flight tube for secondary ions released from the surface. Furthermore, it is important to ensure the sample surface is coincident with both the field of view of the analyser and the area accessed by the ion beam to ensure the full sample area can be accessed by the beam. For example, if the sample is too thick it may result in areas that are inaccessible to the ion beam. In this case, lowering the sample stage would allow the beam to fully access the sample. It is also possible to cool the stage by flowing liquid nitrogen cooled gas through gas lines that are built into the stage block. Furthermore, both the stage and stub contain thermocouples so the temperature may be monitored during experiments of this nature. In this way, volatile, or biological samples can be analysed in a frozen-hydrated state.

The stage is generally held at either + or – 2500 V depending on the type of experiment, or it can be pulsed, to accelerate ions towards the extraction optics. By controlling the length of time the stage is pulsed, known as the pulse width, it is possible to only detect ions produced during the primary ion pulse, thus reducing chemical noise in the mass spectrum.

3.1.3 Primary ion sources

3.1.3.1 Liquid Metal Ion Gun (LMIG)

Commonly, modern ToF-SIMS instruments are equipped with liquid metal ion sources. In particular, gallium is generally used; however, the instrumentation relevant to this investigation used a eutectic gold/germanium alloy. The main advantage of such a mixture is its reduced operating temperature (~400^{o}C) relative to the melting point of pure gold [4].

The source itself (figure 3.4) comprises of a filament, to which, a reservoir of Au/Ge and a needle are attached [5]. The filament is supported by two legs, which serve as electrical contacts.

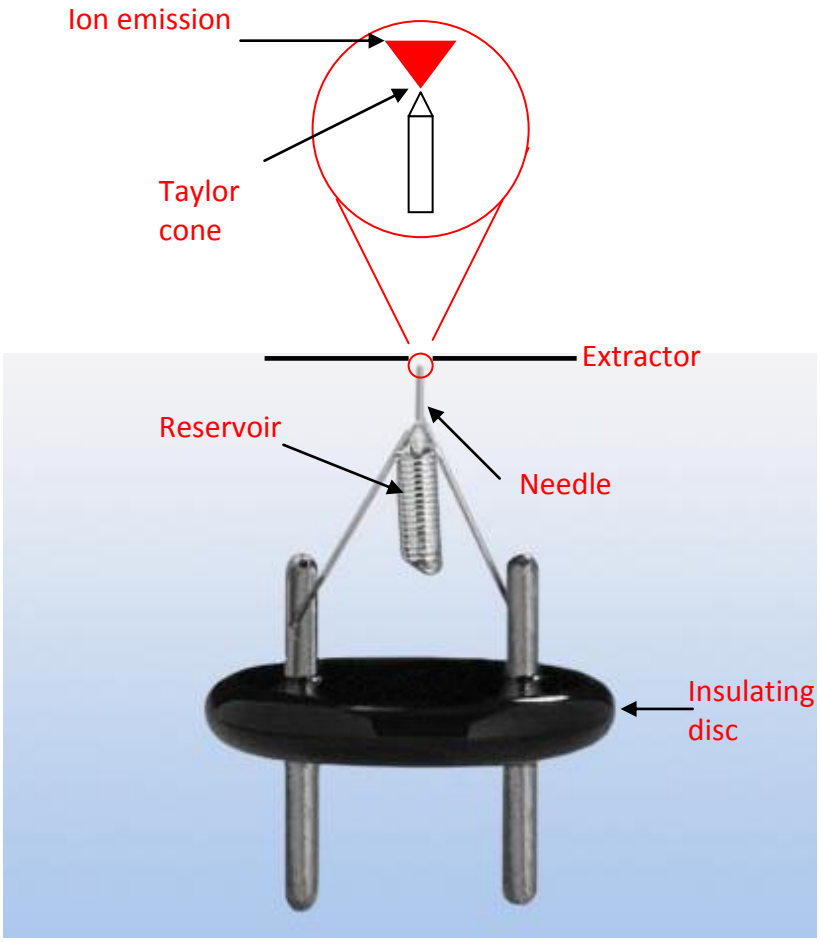

Figure 3.4. Liquid metal Ion source. Adapted from [6].

Close to the tip of the needle is an extraction electrode, to which, a potential is applied (~10 – 25 kV). In this way, an intense electric field is created around the

source tip, which causes Au/Ge ions to move towards the tip of the needle while, similarly, electrons move away down the needle [5]. Consequently, the metal begins to extend to form a Taylor cone (figure 3.4). Following this, once electrostatic and surface tension forces are in equilibrium, emission can occur [5].

Lenses and stigmators are used to focus the beam through the gun assembly, into a bright spot, delivering high current density into a small area. The current and beam diameter delivered by the beam can be varied via a series of replaceable apertures, which can range from 100 µm to 1 mm [2]. For the static SIMS experiment, it is important to pulse the ion beam so as not to cause too much sample damage. To do this, the beam is steered, or "blanked" away from the sample. Essentially, blanking is performed through the application of a potential to only one of the two deflector plates. The beam is then returned to its original position by applying the same potential to the other plate.

As briefly mentioned in chapter 1.2.3, by rastering the ion beam across the sample surface it is possible to create an image, or chemical map of the sample. To do this, the ion beam raster unit employs digital to analogue converters to apply a potential across two other sets of deflector plates [2]. The deflector plates move, or raster, the beam in the X and Y directions across the sample.

Due to the nature of the Au/Ge alloy, there will be ions of different masses emitted from the source. Therefore, mass filtering - using a Wien filter - is necessary to ensure that only selected ions are utilised for analysis. Through the application of mutually orthogonal magnetic and electric fields, orthogonal to the optical axis – with suitable polarity – lateral forces from the fields will oppose each other when:

(3.1) $Bvq = Eq$

B = magnetic flux

E = electric field

v = velocity

q = charge

If this equation, also known as the Wien filter equation, is satisfied for an ion of a particular mass, then that ion will pass through undeflected. Since the velocity (v) depends on mass through the equation $KE=1/2mv^2$ - where KE = Kinetic energy; m = mass; and v = velocity – ions of other masses will be deflected from the optical axis [5].

3.1.3.2 C_{60} ion gun

Unlike the conventional LMIG source, the C_{60} ion gun (figure 3.5) produces ions through what is essentially an effusive source [7]. A small amount (~0.5g) of C_{60} at the rear of the source is heated to ~475^{o}C [7]. The evaporated C_{60} is then ionized through electron bombardment via a thoriated tungsten filament [7]. The resulting C_{60} ions are then extracted and accelerated into the column, through which they are focussed by two lenses. Mass filtering of the beam is again done using a Wien filter and pulsing by a pair of short plates near to the adjustable aperture.

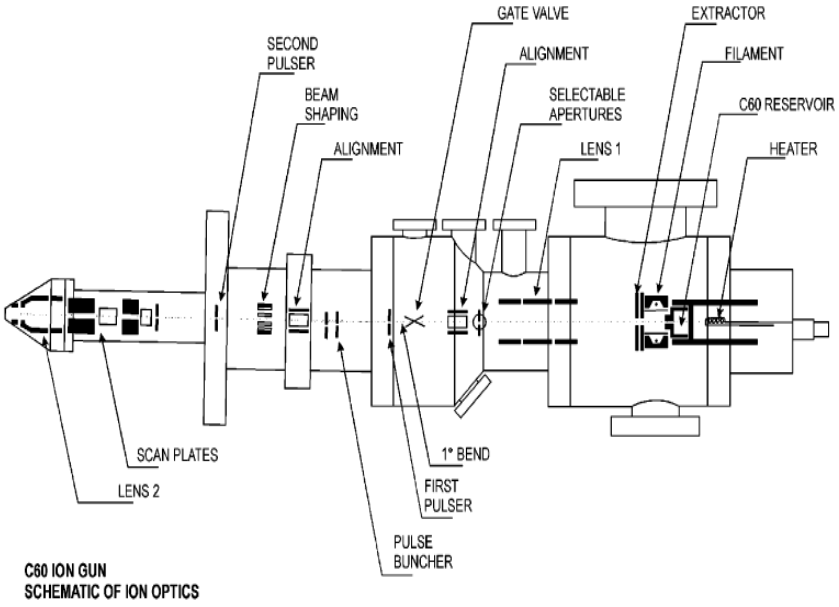

Figure 3.5. Schematic of C_{60} ion gun. Taken from [7].

3.1.4 Time of Flight (ToF) mass analyser

The time-of-flight mass analyser (figures 3.1 and 3.2) has a high transmission efficiency (10-50%) and high sensitivity. However, to use the ToF system a pulsed primary ion beam must be used, after which the resultant ions are subjected to delayed, non-delayed or DC extraction; used to accelerate them to a given potential. Following this, the charged particles are pulsed into the field free, or drift, zone. The time (t) taken for masses (m) to travel through this region of length (d) can be calculated by the following:

(3.2) $$t = d\sqrt{(m/2zv)}$$

t = Time of flight

d = length of flight tube

m = mass of ion

z = ion charge

v = electric field

Lighter ions therefore, have a higher velocity than heavier ions when passing through the drift zone. However, to decrease kinetic energy dispersions which arise through the sputtering process, between ions of the same mass, a reflectron is used. In this way, the mass resolution of the instrument is

increased. Very simply, the reflectron is an electrostatic mirror that creates a retarding and reflecting field. Ions of a given mass to charge ratio (m/z) and high kinetic energy will penetrate further into this field before being turned around than those of equal mass but lower kinetic energy. Therefore, ions of the same m/z but differing kinetic energies will be detected at the same time.

3.1.5 Microchannel Plate (MCP) Detector

Having travelled through the reflectron ToF tube, the mass resolved secondary ions are converted into an electrical signal, which can be detected and counted. The conversion from ion beam to electrical signal occurs within the microchannel plate detector. Essentially, ions impinge upon the lead/glass plate surface, which results in electron emission, and consequently, an electron cascade. The signal is further multiplied via a second plate, after which they strike a metal anode, thus creating the output signal.

If however, the ions are particularly large or heavy they can often impact with such low velocity or energy density that an electron cascade does not occur. To alleviate this problem the ions are subjected to a final electrical field (~22 kV) of opposite charge prior to detection. This is known as post acceleration and allows for increased signal in the higher mass ranges.

Finally, the signal created through the above process is recorded using a time to digital converter (TDC). This part of the instrumentation records a hit every time the signal exceeds a threshold voltage.

3.1.6 Electron Flood Gun

As described earlier secondary ions are formed by the impinging primary ion beam. A direct result of this is a build up of positive charge on poorly conductive samples, which, if unchecked, can compound analysis. The solution to this problem involves the use of a low energy electron gun (~25 eV) to flood the sample surface following extraction [8]. It is important to note, however, that the electron dosages must be kept to less than 6×10^{18} electrons/m^2, or 90nA

delivered over an area of 3mm x 3mm for a 100s spectrum, so as to prevent further sample damage while maintaining charge neutralisation [8].

3.2 Synchrotron sourced FTIR microspectroscopy

Previously, FTIR was introduced and general theory explained. The following will provide instrumental information and discuss some of the main advantages of using a synchrotron light source – used in this investigation - instead of a conventional thermal source.

Synchrotron radiation is emanated from relativistic electrons as they are accelerated in a circular trajectory. To do this, magnets are positioned around the circumference of an ultra-high vacuum insulated pipe. The emitted radiation is essentially "white light", encompassing the entire wavelength range of the electromagnetic spectrum [9]. The 3-20µm wavelengths (mid-IR) of the source are then focussed into a beam with an approximate 10 µm spot size and introduced – as an external source – into the FTIR spectrometer and into the interferometer [10,11].

The FTIR data for this investigation was collected at two separate synchrotron facilities. These were the SISSI beamline at Elettra in Trieste, Italy and the SMIS beamline in Soleil, France. The coupling of the spectrometer to the beamline is relatively similar for both. The synchrotron radiation, however, is directed into the spectrometers in slightly different ways.

3.2.1 Soleil

The Soleil synchrotron is a third generation source of around 2.75 GeV and contains two IR stations [12]. The first (figure 3.6 S1), utilises bending magnet radiation, while the second (figure 3.6 S2) takes advantage of edge radiation. The majority of beam lines have exploited the radiation emitted by bending magnets; however, edge radiation is becoming more widely used [12]. The Advanced Infrared Line Exploited for Spectroscopy, or AILES (Figure 3.6 S2) as commonly abbreviated, connected to a NIC-plan Nicolet Magna Michaelson

interferometer (Thermo Fisher scientific, MA, USA), was used for the investigation. More detailed descriptions of the beam line optics and performance can be found elsewhere [12].

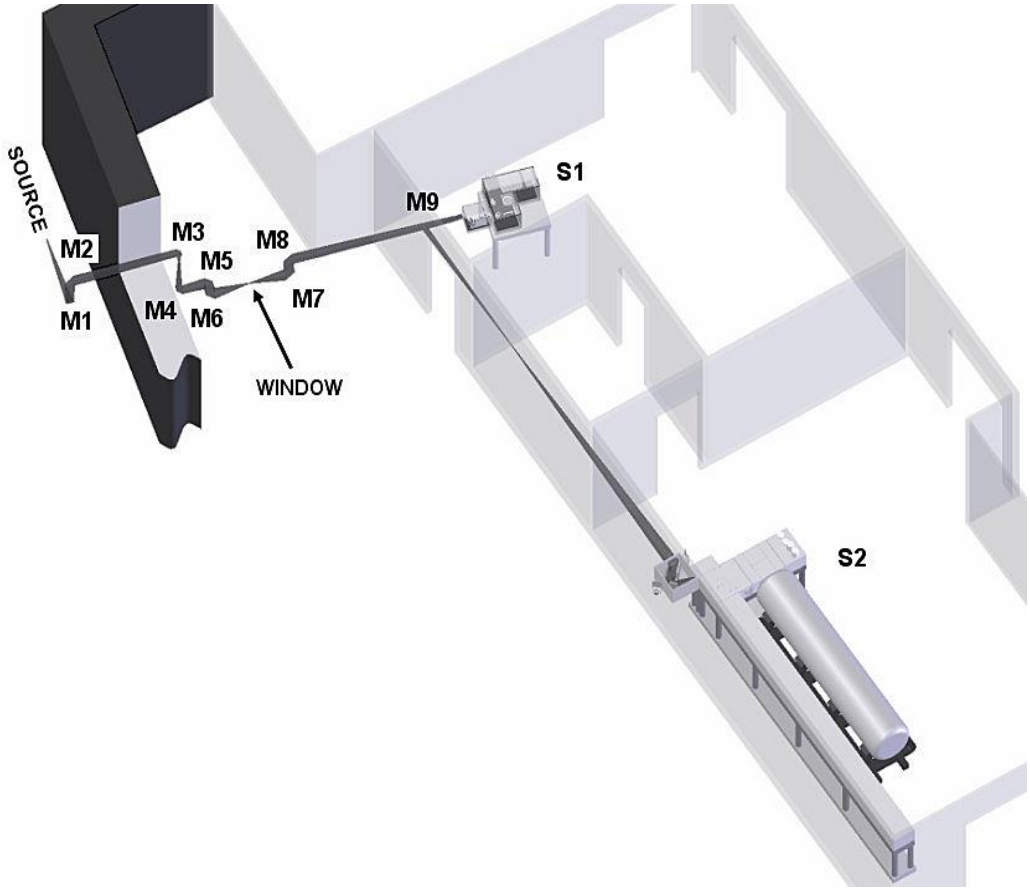

Figure 3.6. The layout of the two IR beamlines at Soleil. M1, M3, M4, M5, M8 and M9 and flat mirrors, M2, M6 and M7 are Toroidal mirrors. S1 and S2 are the IR stations. Reproduced from [12].

3.2.2 Elettra

The second beam line used is connected to the Elettra ring (2.4 GeV) in Trieste, Italy. The Source for Imaging and Spectroscopic Studies in the Infrared, or SISSI, exploits bending magnet radiation and a Bruker IFS-66v Michaelson interferometer (Bruker Optik GmbH, Germany) (figure 3.7) [11].

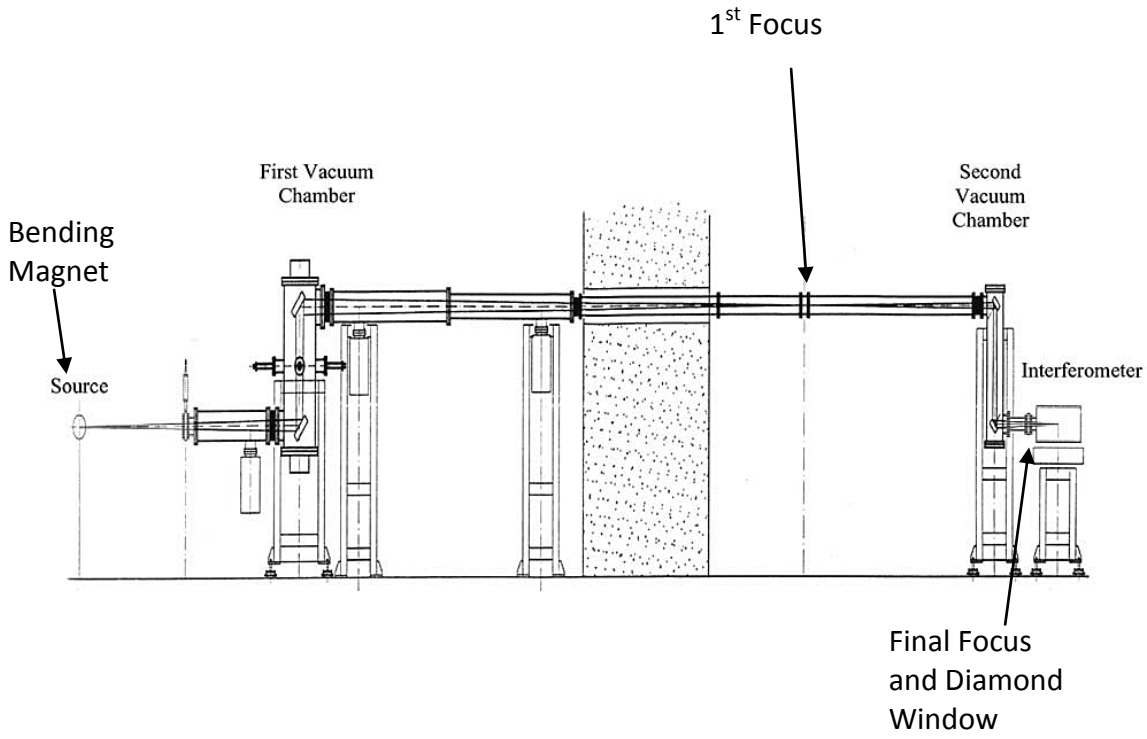

Figure 3.7. Schematic of the SISSI beamline at Elettra [11]

It should be noted that both facilities offered excellent beam stability, but, the Soleil beam was slightly more stable than Elettra. However, the Bruker instrumentation used at Elettra had a programmable stage, which allowed for a more high-throughput analysis. This is of great importance at a synchrotron facility where experimental time is limited.

3.2.3 Advantages of synchrotron sources

Good spectral signal to noise is paramount when performing infrared microspectroscopy to detect subtle chemical differences in biological samples. Conventional thermal sources are limited by the fact that decreasing the aperture size decreases the IR flux reaching the detector [13]. Therefore, the signal to noise ratio decreases, which has a detrimental effect on spectra (figure 3.8 B) [13].

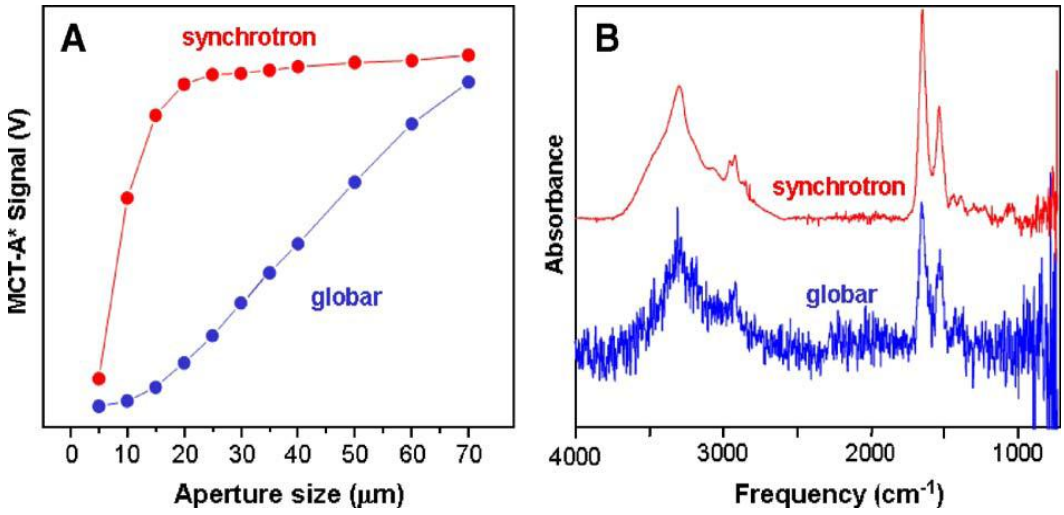

Figure 3.8. Plot A shows the change in detected infrared signal through various aperture sizes. Plot B illustrates the signal to noise differences of a single cell spectrum between a synchrotron and globar source. Taken using an aperture of 5 x 5 μm^2. Reproduced from [13].

Synchrotron IR sources have the advantage of high intrinsic brilliance which is often 100-1000 times greater than traditional thermal emission sources [14]. This advantage is predominantly due to the high flux density of the synchrotron source and allows the analysis of smaller samples, such as single cells, with acceptable signal to noise ratios using smaller aperture sizes (figure 3.8). This is because the effective source size is much smaller and the light is more collimated, in contrast to globar sources which emit through a much larger range of angles [14]. Figure 3.8A illustrates this by the large differences in

intensity between the two sources for the same aperture sizes, most noticeably for aperture sizes of 10-20µm^2. However, as the synchrotron source is only 10-20µm^2 this advantage is reduced for aperture sizes above this, again shown by figure 3.8A [13,14].

3.3 Cytospinning

Commonly, cytospinning is used by biologists for spinning cell suspensions onto microscope slides. The following investigation adapted this technique to spin cell suspensions onto Si wafer for ToF-SIMS analysis, and CaF_2 slides for FTIR analysis. The cytospin used for this particular study was a Shandon Cytospin 4 Cytocentrifuge (Thermo Fisher scientific, MA, USA) (figure 3.9) [15].

Figure 3.9. Shandon Cytospin 4 Cytocentrifuge. Taken from [15]

A detailed description of the cytospin and its capabilities can be found elsewhere [15]. However, very simply, figure 3.10 illustrates a cross section of the cytospin rotor with cytofunnels in place. Three to four drops of the cell suspension are placed into the cytofunnels –inside the rotor - before replacing the lid and inserting into the cytospin (figure 3.9). The instrument is then programmed and started. As the rotor spins the centrifugal forces push the cell suspension onto the Si wafer which deposits the cells, while the blotting paper absorbs the excess fluid (figure 3.10).

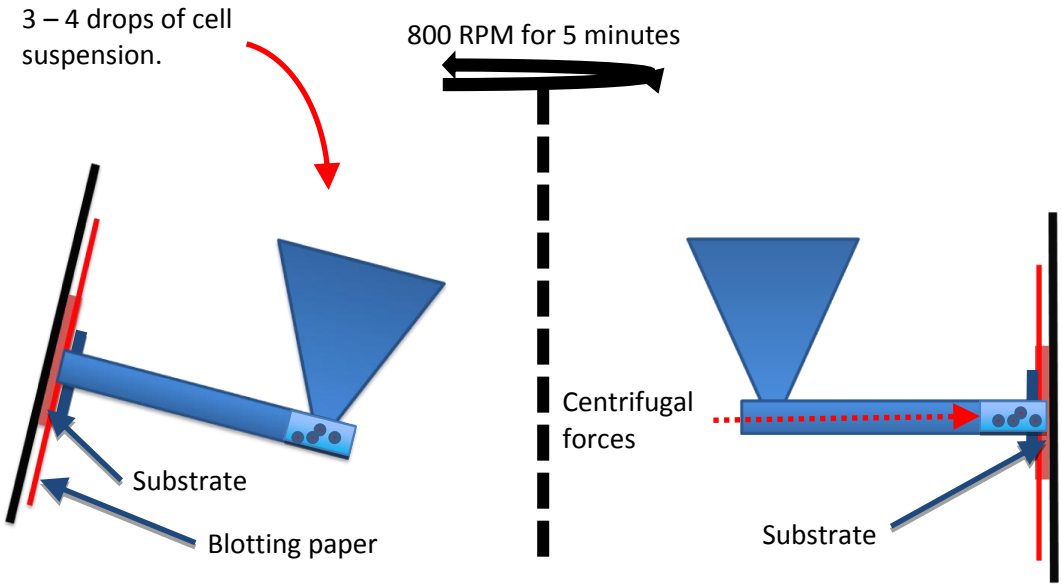

Figure 3.10. Schematic of the cytospin rotor and cytofunnels.

3.3 Fluorescence Assisted Cell Sorting

From the first patent in 1968 [16], cell sorters have been developed to sort around 60 million cells/hour and are now predominantly developed by Becton Dickinson. Fluorescence activated cell sorting, or FACS, as commonly abbreviated, is used to sort a heterogeneous mixture of biological cells into two or more containers. To do this, the system uses specific fluorescent and light scattering properties of each cell.

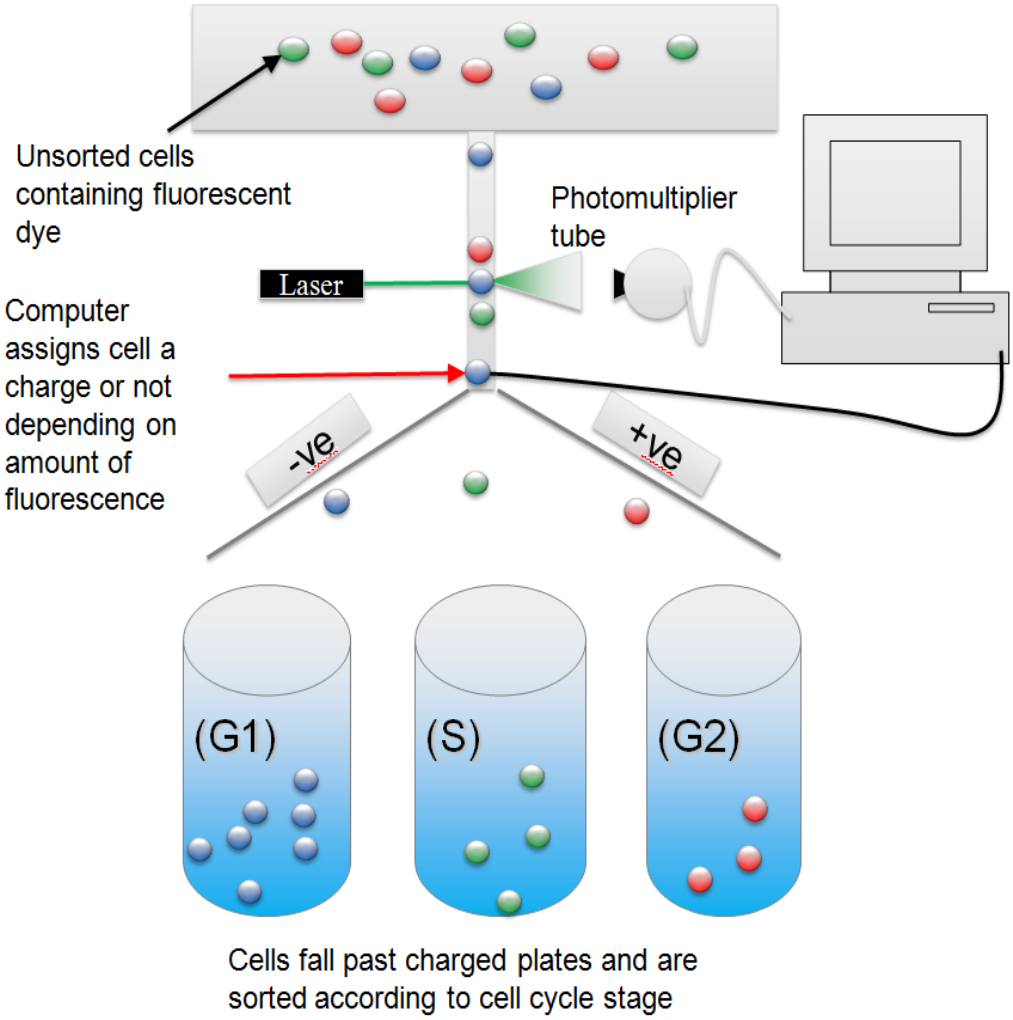

Figure 3.11. Schematic of a FACS sorter.

Unsorted cells containing a fluorescent dye, such as propidium iodide, are passed through a laser one at a time (figure 3.11). The laser excites the dye and the computer assigns the cell a positive, negative, or no charge according to the

amount of fluorescence detected. The cells then pass between charged plates and are sorted into containers accordingly. Therefore, it is possible to obtain enriched fractions of cells in the different phases of the cell cycle. A more in depth description of flow cytometry and FACS sorting can be found elsewhere [16].

References

[1] J. C. Vickerman. ToF-SIMS An overview. In: *ToF-SIMS surface analysis by mass spectrometry*. IM publications (2001) Chapter 1. p1-41 ISBN 1 901019 03 9

[2] R.M. Braun, P. Blenkinsopp, S.J. Mullock, C. Corlett, K.F. Willey, J.C. Vickerman and N. Winograd. *Rapid communications in mass spectrometry.* 12 (1998) p1246-1252

[3] Kore technology: http://www.kore.co.uk/ms2000.htm. Visited on 26/7/2010

[4] N. Davies, D.E. Weibel, P. Blenkinsopp, N.P. Lockyer, R. Hill and J.C. Vickerman. *Applied surface science.* (2003) p223-227

[5] R. Hill. Primary ion beam systems. In: *ToF-SIMS surface analysis by mass spectrometry*. IM publications (2001) Chapter 4. P95-112

[6] FEI company tools for nanotech: http://www.fei.com/products/components/electron-ion-sources.aspx. Visited on 26/7/2010

[7] D. Weibel, S. Wong, N. Lockyer, P. Blenkinsopp, R.Hill and J.C. Vickerman. *Analytical chemistry.* 75 (2003) p1754-1764

[8] I.S. Gilmore and M.P Seah. *Applied surface science.* 187 (2001) p89-100

[9] G.P. Williams, W.D. Duncan. *Applied Optics.* 22(18) (1983) p2914-2923

[10] P. Dumas, F. Polack, B. Lagarde, O. Chubar, J.L. Giorgetta, S. Lefrancois. *Infrared Physics and Technology.* 49 (2006) p152-160

[11] A. Nucara, S. Lupi and P. Calvani. *Infrared Physics and Technology.* 45 (2004) p375-381.

[12] P. Roy, M. Rouzieres, Z. Qi and O. Chubar. *Infrared Physics and Technology.* 49 (2006) p139-146

[13] L.M. Miller, P. Dumas. *Biochimica et Biophysica Acta.* 1758 (2006) p846-857

[14] J.A Reffner, P.A. Martoglio and G.P. Williams. *Review of scientific instruments.* 66 (1995) p1298.

[15]Thermoscientific: http://www.thermo.com/com/cda/product/detail/1,,16469,00.html. Accessed on 31/07/10

[16] M. J. Fulwyler *United States Patent Office*. (1968) Number 3380584

[17] Z. Darzynkiewicz and H.A. Crissman. *Flow cytometry volume 33*. Academic Press. Inc (1990). ISBN 0-12-564133-8

Chapter 4: A systematic evaluation of cytospinning as a novel technique for the preparation of cells for ToF-SIMS analysis

As previously mentioned, Time-of-flight secondary ion mass spectrometry is capable of elemental and molecular analysis of complex chemistry on the sub-cellular scale [1]. However, the high vacuum requirement of SIMS prevents the analysis of live cells because of their water content. Robust sample preparation protocols are therefore critical in preserving the biochemical architecture of biological samples and extracting meaningful information [2,3,4].

The optimum preparation protocol will almost certainly depend on the nature of the sample, the type of instrument used, and the aim of the analysis. For example, 70% ethanol fixation can be used to remove lipid membranes and expose intracellular proteins for analysis, if required. As a result various different preparation protocols have been adopted as reviewed earlier (Chapter 2.1) [1-4]. Previously, biological SIMS analysis has focused mainly on cell cultures, grown on SIMS-compatible substrates, or on tissue sections. The following chapter will discuss a systematic evaluation of cytospinning based techniques for the preparation of biological cells and nuclei – used as a novel, less complex system - directly from suspension for ToF-SIMS analysis. This was achieved through comparisons with existing air drying and freeze drying protocols. Furthermore, prior to ToF-SIMS analysis complementary techniques of fluorescence imaging and SEM were used to assess cellular architecture. Additionally, cytospun samples were freeze fractured to assess whether the two techniques were compatible for the analysis of frozen hydrated samples.

4.1 Experimental

4.1.1 Hela-M Cell culture

Cells from the Hela-M human cervical cancer cell line [5] were seeded in 25cm^3 sterile plastic culture flasks (Fisher Scientific, UK). After culturing (37^{0}C, 5% CO_2, in air) in media (DMEM, 10% FCS, 1% penicillin/streptomycin, 1% L-glutamine, 1% non-essential amino acids and 1% sodium pyruvate, Sigma Aldrich, UK) to around 80% confluency, the media was removed. The cells were then washed in Dulbecco's Phosphate Buffered Saline (DPBS) (10ml, Sigma Aldrich, UK), after which 1ml trypsin solution (0.5 mg/ml trypsin; 0.2 mg/ml EDTA in PBS, Sigma Aldrich, UK) was added and the cells were incubated (3 minutes, 37^{0}C, 5% CO_2, in air). The cells were then resuspended in the growth media (4ml) and removed for centrifugation. Once removed, the cell suspension was centrifuged (800 RPM, 5 minutes) and the supernatant discarded. The cells were then resuspended in DPBS (5ml) and centrifuged as before. Finally, the DPBS was removed and the cells were suspended – and fixed – in formalin (4ml, 4% in PBS).

4.1.2 PC-3 cell culture and nuclei extraction

Cells from the PC-3 human prostatic adenocarcinoma (metastatic to bone) cell line [6] were seeded in 75cm^3 sterile plastic culture flasks (Fisher Scientific, UK). After culturing (37^{0}C, 5%CO_2 in air) in PC-3 media (Ham's F12, 7% FCS and 2mM L-glutamine) to around 80% confluency the media was removed. The cells were then washed in DPBS (10ml), after which, ice cold nuclei EZ lysis buffer (4ml, Sigma Aldrich, UK) was added. Cells were then harvested and lysed by scraping with a small bladed cell scraper. The entire cell lysate was then transferred to a 15ml centrifuge tube, vortexed (40 seconds), and set on ice (5 minutes). Nuclei were collected through centrifugation (800 RPM, 5 minutes, 4^{0}C), resuspended in Nuclei EZ lysis buffer (0.5ml, Sigma Aldrich, UK) and vortexed (40 seconds). Once the pellet was fully resuspended Nuclei EZ lysis buffer (3.5ml, Sigma Aldrich, UK) was added, mixed and the tube set on ice (5 minutes). Nuclei were then collected by centrifugation (800 RPM, 5 minutes, 4^{0}C) and fixed in formalin (4ml, 4% in DPBS). Samples were stored in a refrigerator (4^{o}C).

4.1.3 Sample preparation

Prior to each sample preparation method the substrate (silicon wafer, Agar Scientific Ltd, UK) was cleaned by sonicating 5 min in chloroform, washing twice in water and sonicating 5 min in ethanol. All solvents were HPLC grade (Sigma Aldrich, UK).

Air dried nuclei were prepared by pipetting the nuclei suspension (5µl) onto Si wafer and allowing to dry. Washed samples were dipped in 0.15M ammonium formate (30 seconds).

Freeze dried nuclei were prepared by dropping nuclei suspension (5µl) onto cleaned Si wafer and then flash freezing (liquid N_2). The samples were then freeze dried in a Heto Drywinner freeze dryer (24 hours, 10^{-3} mbar at -110^{o}C, Edwards High Vacuum, UK). Washed samples were dipped in 0.15M ammonium formate (30 seconds).

Cytospun nuclei and cells were prepared using a Shandon Cytospin 4 Cytocentrifuge (Thermo Fisher scientific, MA, USA). Suspensions of nuclei or cells (150µl) were placed into the cytofunnels® and spun (800RPM, 5mins, low acceleration) onto cleaned Si wafer.

Freeze fractured samples were prepared by cytospinning cells onto cleaned Si wafer. Immediately after this, a second Si shard was placed on top and the "sandwich" was plunged into liquid nitrogen cooled propane (30 seconds). The sample was then manually fractured under liquid nitrogen using a liquid nitrogen cooled scalpel and forceps and introduced into the SIMS instrument.

4.1.4 Microscopy Imaging

Scanning electron microscopy was used to study the morphology of the nuclei and cells after cytospinning. Cytospun samples were coated with a thin layer of gold – palladium and imaged in under high vacuum and medium voltage (30 kV) using a FEI Quanta 200 Environmental SEM (FEI™, Oregon, USA).

Fluorescence microscopy was used to study the internal architecture of the cells after cytospinning. Cells were cultured in the presence of a baculovirus that, upon entry into the cells directs the expression of an intracellular targeted fluorescent protein. This system is known as an organelle light™ (Molecular Probes®, Invitrogen™, UK). More specifically, the organelle light™ used was a red fluorescent protein associated with the lipid membrane. The treated cells were then removed from their substrate and cytospun onto a glass slide. To view the cell's nuclei, Vectashield® fluorescent mounting media containing 4', 6-diamidino-2-phenylindole (DAPI) - a dye that binds to DNA - (Vector Laboratories, Burlingame, CA, USA) was then dropped over the sample prior to fluorescence imaging. A glass coverslip was laid over the sample and sealed with clear nail varnish before imaging with a Zeiss Axiovert 200 fluorescence microscope, equipped with a x100 lens (Carl Zeiss Inc, NY, USA).

4.1.5 ToF-SIMS analysis

ToF-SIMS analysis was performed on the Bio-TOF SIMS instrument described earlier [7]. The primary ion beam used for analysis was Au^+ or Au_3^+ as detailed below. For frozen hydrated samples etching was performed with C_{60}^+ to remove surface ice overlayers. The dose density used for this was 3×10^{15} ions/cm^2/s. This was calculated by the following:

1. C_{60} ion beam current measured on the sample stage:

$$200 \text{ pA} = 2 \times 10^{-10} \; C/s \text{ (as 1 ampere = 1 coulomb per second)}$$

2. Divide by the number of coulombs per ion to give the dose for 1 second.

Charge of an electron

$$\frac{2 \times 10^{-10}}{1.6 \times 10^{-19}} = 1.25 \times 10^{9}\ ions/s$$

3. The dose density is then calculated by dividing this by the area of bombardment (500 × 500 µm^2)

$$\frac{1.25 \times 10^{9}}{2.5 \times 10^{-1}} = 5 \times 10^{13}\ ions/cm^2/s$$

cm^2

4. A 60 second etch was used so the final dose density was:

$$60 \times (5 \times 10^{13}) = \mathbf{3 \times 10^{15} ions/cm^2/s}$$

For analysis a primary ion fluence of < 10^{13} ions/cm^2 was used to minimise sample damage due to gold bombardment. Images were taken over a 256 x 256 µm^2 field of view and delayed extraction was used. Ion detection was achieved using a dual microchannel plate operating at 20 keV post-acceleration.

For frozen hydrated work the base pressure was maintained at 10^{-9} mbar using a liquid nitrogen-cooled cryoshield to remove residual water contamination. The sample stage was cooled to -150^{0}C prior to sample introduction and maintained at this temperature during analysis.

4.2 Results and discussion

Using a two model system of PC-3 cells and Hela-M cells, cytospinning based protocols were developed and evaluated. PC-3 cell nuclei were chosen as a less complex system prior to the analysis of whole Hela-M cells. The objective was to find optimal preparatory protocols for the analysis of cells in suspension and to evaluate these techniques, with respect to their capability to preserve the biochemical architecture of the sample.

The influence of cytospinning on the morphology of fixed nuclei was assessed using scanning electron microscopy (SEM) (figure 4.1A). In this case fluorescence microscopic analysis was unnecessary as preservation of the sub-organelle morphology can be observed. This is shown by the presence of the protein rich nucleoli [8]. However, there is some obvious flattening of the nuclei due to centrifugal forces.

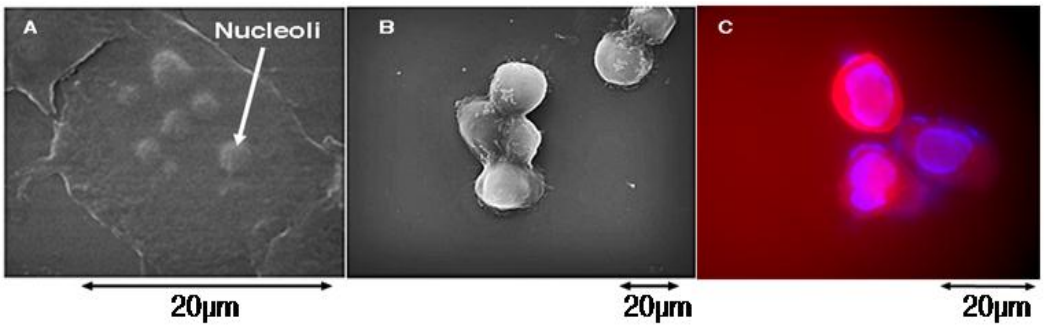

Figure 4.1. SEM images of nuclei (A) and cells (B). C is a fluorescence image of cells.

Following SEM imaging, unwashed and washed cytospun samples were analysed using ToF-SIMS. Positive relative ion yields were determined by selecting a 50 x 50 μm^2 area of biological interest and calculating yields as a percentage of the total ions for that area (figure 4.2). This was repeated for both unwashed and washed air dried and freeze dried samples (figure 4.2). Interestingly, figure 4.2 shows a significant increase in the relative yields of biological ions for both washed and unwashed cytospun samples compared to the other techniques. Figure 4.2 also highlights the important issue of reproducibility with biological sample preparation. This is observed as large error bars showing the standard deviation, which is to be expected of a biological sample. These error bars are slightly larger in washed samples. This is most likely due to the fact that washing adds more variability in sample material because the degree of washing will differ between samples. Furthermore, the greatest variations are generally consigned to those species which are more readily ionised (e.g. m/z 184 and m/z 86). Small differences in these caused by the heterogeneity of the biological samples will therefore lead to great variations in signal.

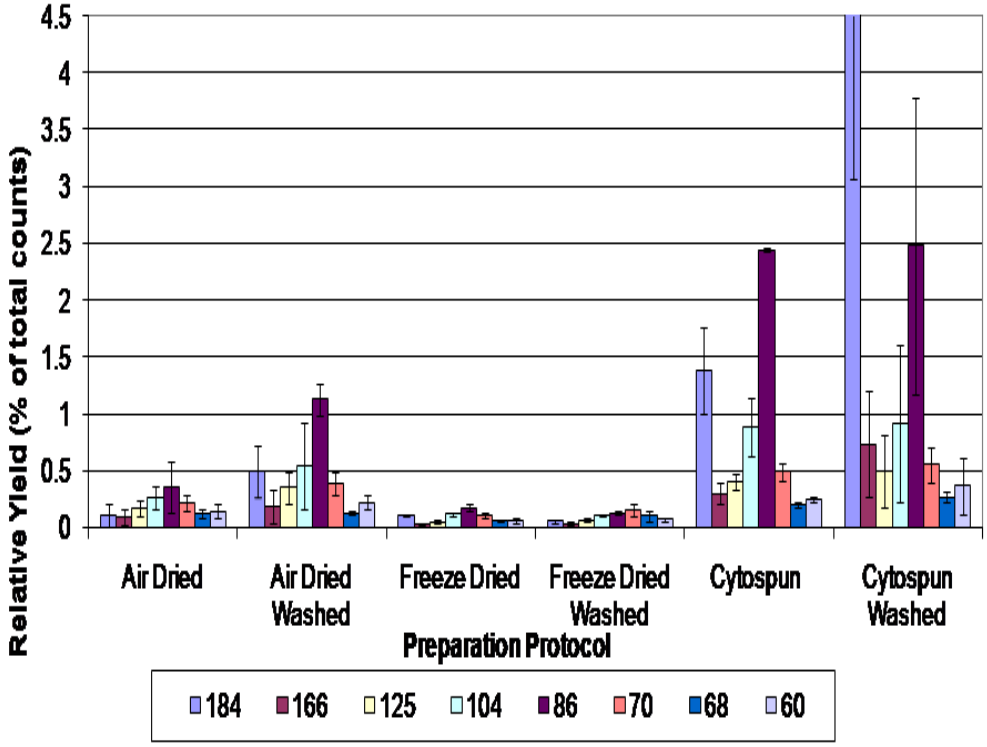

Figure 4.2. Plot of positive ion yields for a range of lipid (m/z 184, 166, 125, 104 and 86) and amino acid (m/z 70, 68 and 60) peaks. The data are presented as means ± s.d (n=5)

Equally as important as organic ions are the inorganic species, as they can lead to ion suppression effects. One of the problems with the preparatory techniques used in this study was a susceptibility to contamination from the chemicals used for nuclear extraction. Figures 4.3A and 4.3B illustrate one particular contaminant from the lysis buffer. This could only be removed using cytospinning with an ammonium formate wash (figure 4.3B). Another inorganic ion of interest is sodium, which has been shown to suppress organic signal [9]. It is thought the large reduction in sodium observed for cytospun samples (figure

4.4) is contributing heavily to the increase in biological yields seen in figure 4.2.

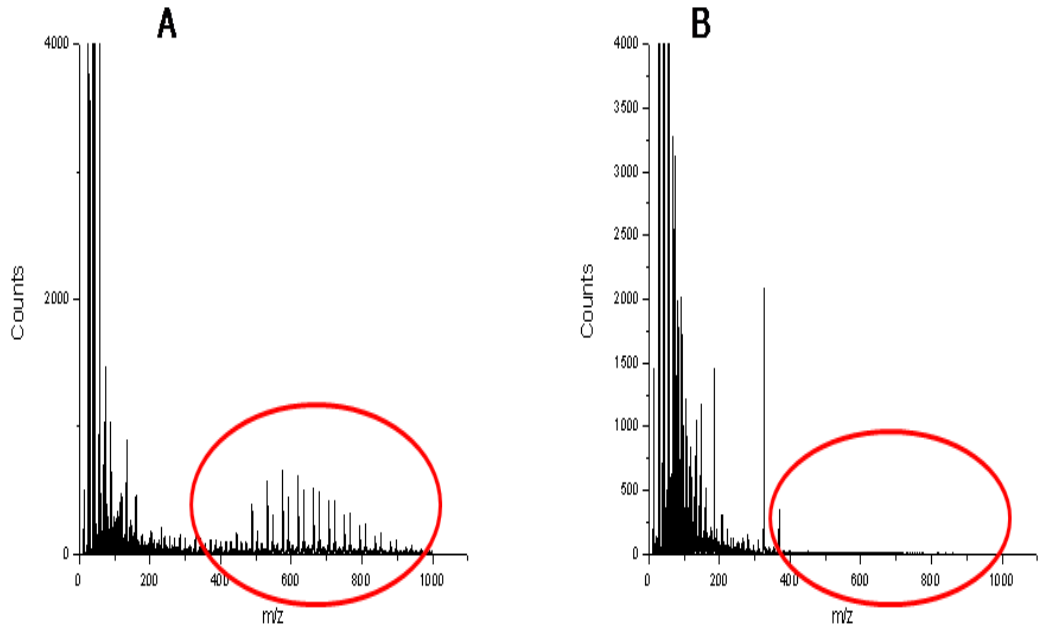

Figure 4.3. Positive SIMS spectra showing presence (A) and removal (B) of chemical contamination.

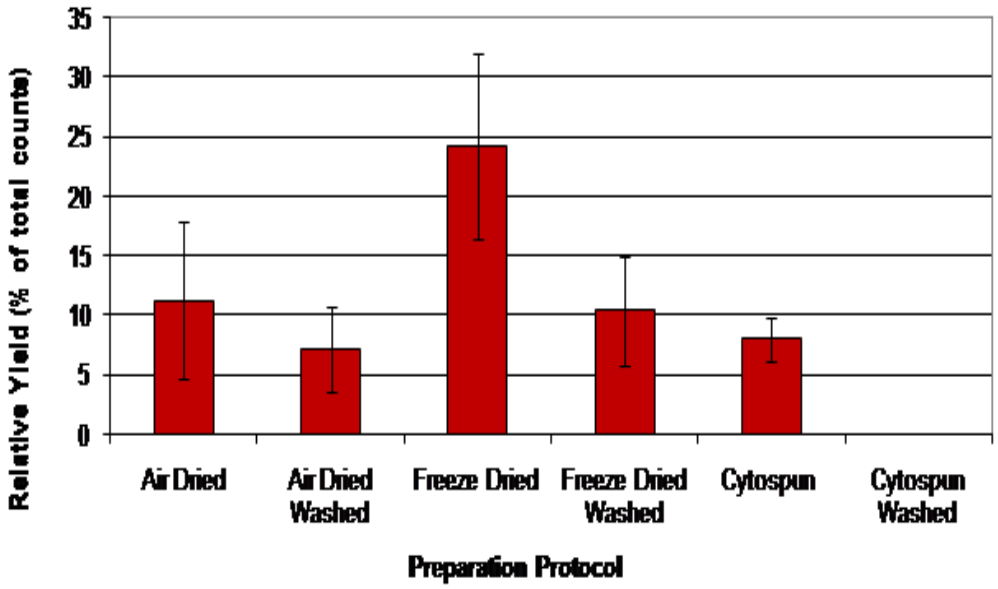

Figure 4.4. Plot showing relative ion yields of sodium. The data are presented as means ± s.d (n=5)

To illustrate the effects of washing further, average absolute yields were calculated (figure 4.5). Again it is clear that washing effectively removes sodium for all of the preparation methodologies, and consequently, yields of organic species increase. This is particularly pertinent for cytospun samples as a

significant increase in yields of biological ions is seen after salt removal. This is important as absolute yields of biological ions are increasing and not just increasing relative to salt species after washing.

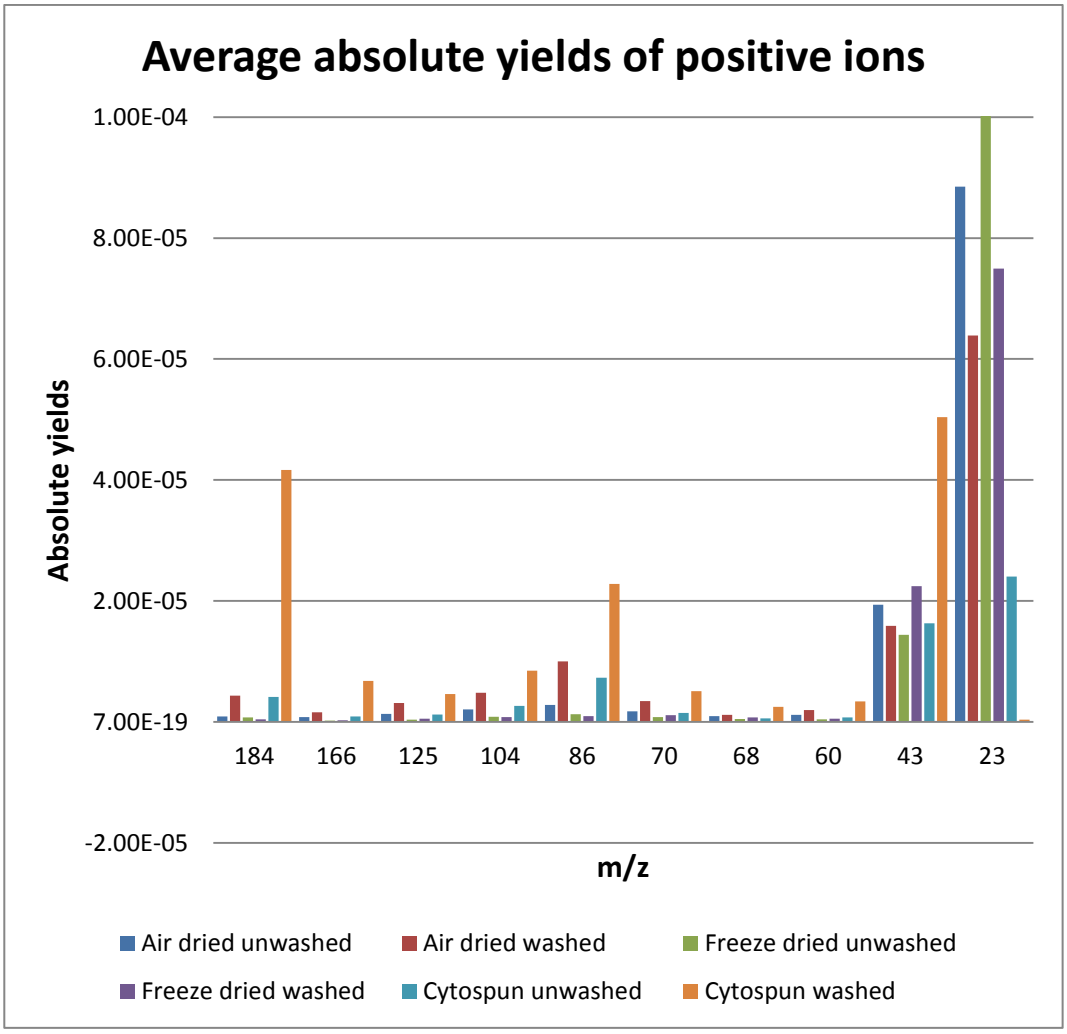

Figure 4.5. Average absolute yields of positive ions.

The investigation was then progressed onto Hela-M cells. Biochemical architecture was evaluated, once more, using SEM imaging to observe the surface morphology (figure 4.1B). To ensure the internal structure was retained, fluorescence imaging was used to examine the lipid membrane that encapsulates the cell, and the nucleus (figure 4.1C). Figure 4.6 shows the SIMS images obtained using a Au_3^+ primary beam on cytospun, washed Hela-M cells. The images clearly show that in both positive and negative ion mode important chemistry can be localised to the cell. It should be noted that these images were taken from different sample areas so they do not correlate.

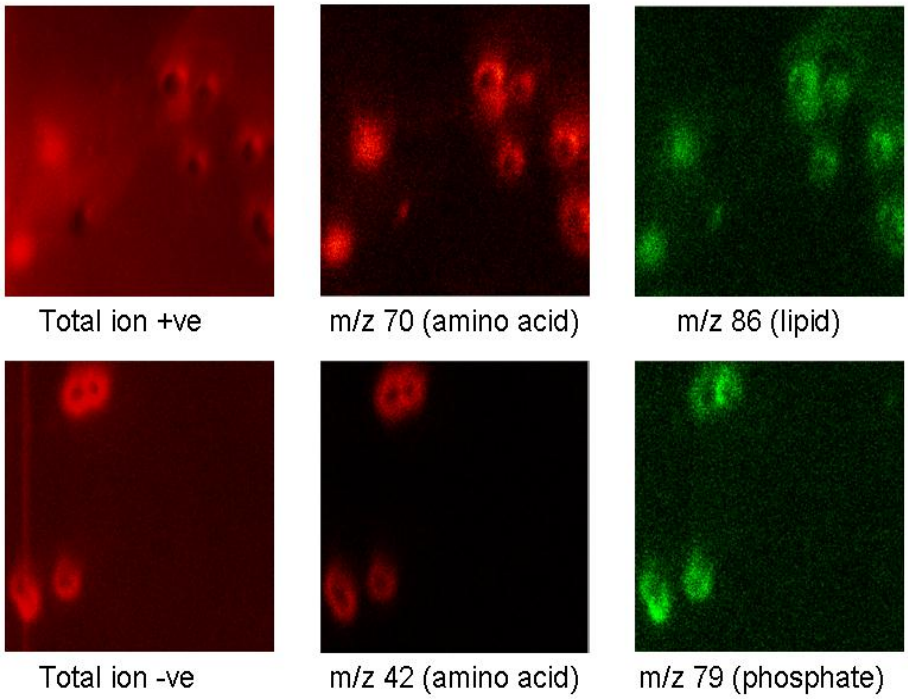

Figure 4.6. SIMS images of cytospun, washed Hela-M cells. Taken over a 250 × 250 μm^2 field of view using Au_3^+.

Finally, the amenability of cytospinning to frozen hydrated analysis was studied. This was achieved through freeze fracturing and C_{60}^+ sputter etching. In this way, a depth profile was performed; providing a means, by which, it was possible to comment upon the success of the experiment. For example, if there had been too much ice it would have not been possible to detect any ions from biological origins, and therefore could be deemed unsuccessful. Figure 4.7 illustrates the depth profile of freeze fractured, cytospun Hela-M cells. Removal of atmospheric water and the appearance of biological ions can be seen. The emergence of intracellular potassium, often reported as an indicator of cellular integrity [10] is also shown as the membrane is etched away by C_{60}^+ sputtering. It is also important, however, to recognise that the presence of water can lead to an enhancement of analyte signals from the frozen-hydrated matrix [11]. Therefore, there is a possibility that the patterns of sharp increases in biological signals, thought to represent the appearance of biological material as the ice is etched away (figure 4.7) could, in fact, be artefacts created through this effect.

Etching away the ice to a thin layer could create the conditions necessary for this phenomenon [4]. The latest spring-loaded fracture devices would provide a more reproducible means, by which, this could be investigated further [12]. Manual freeze fracturing is a difficult process to control, in this case, cells were almost certainly not fractured but atmospheric ice was removed.

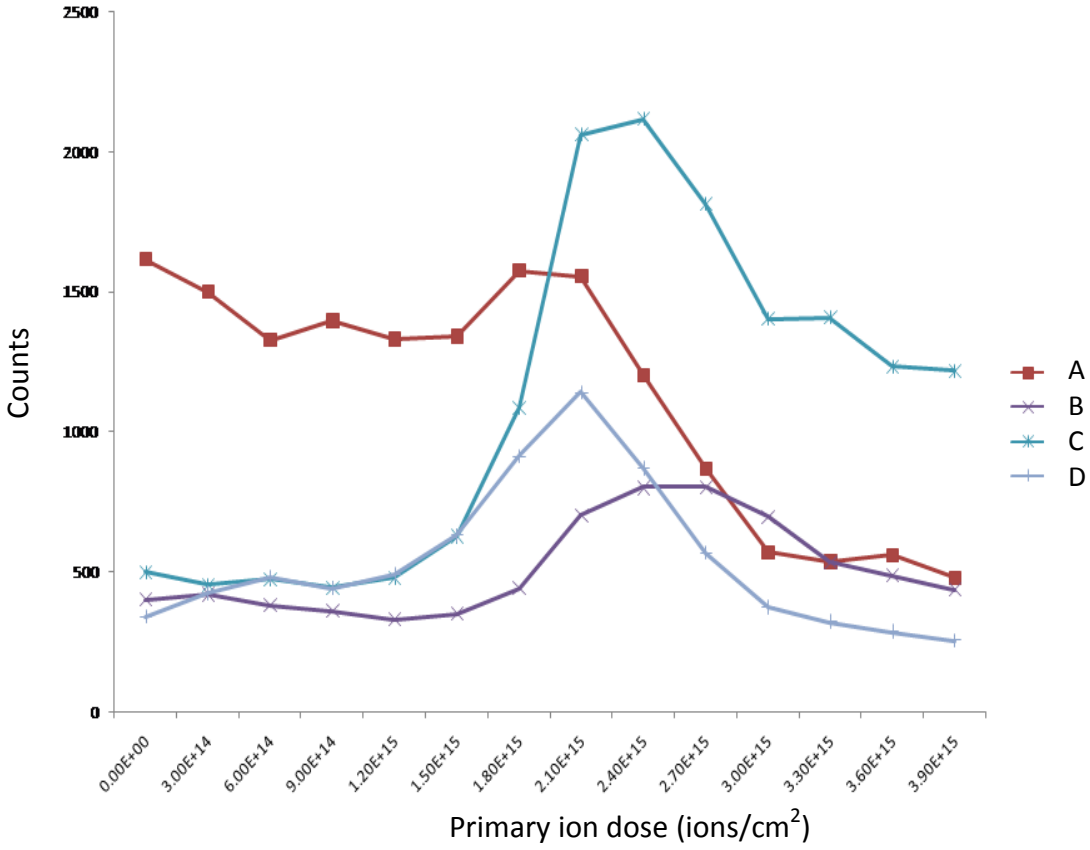

Figure 4.7. Depth profile plot of signal from ions of interest ([A] $H_3O(H_2O)^+$, [B] K^+, [C] C_4H_8N and [D] $C_5H_{15}NO_4P^+$) against primary ion fluence for freeze fractured, frozen hydrated Hela-M cells.

4.2 Conclusions

Cytospinning is a viable alternative to existing methods of preparation for biological cells. For samples grown on substrates and tissues, where cytospinning cannot be applied, washing is beneficial [2]. Our results suggest washing may be less critical for cytospun samples due to the removal of most of the extracellular liquid matrix, and associated contaminants such as Na^+, during the cytospinning step. However, washing is still beneficial as significant increases

in biological yields are seen. Importantly, the methodology presented here is directly compatible with other complementary analytical techniques and imaging modalities for cellular characterisation. This avoids the need to culture cells on a substrate specific to an analytical technique, avoiding the likelihood that cellular chemistry is influenced by different substrates, and making non-adherent cells amenable to analysis.

References

[1] D.Breitenstein, C.E. Rommel, J. Stolwijk, J. Wegener, B. Hagenhoff. *Applied Surface Science* (2008) ; 255, 1249-1256.

[2] J. Malm, D. Giannaras, M. O Riehle, N. Gadegaard, and P. Sjövall. *Anal. Chem.* (2009) ; doi: 10.1021/ac900636v

[3] M.E. Kurczy, P.D. Piehowski, S.A. Parry, M. Jiang, G. Chen, A.G. Ewing. N. Winograd. *Applied Surface Science* (2008) ; 255, 1298-1304.

[4] S.Chandra. *Applied Surface Science* (2008) ; 255, 1273-1284.

[5] G. O. Gey, W.D. Coffman & M. T. Kubicek. *Cancer Res.* (1952) ; 12, 264–265

[6] M.E. Kaighn, K.S. Narayan, Y. Ohnuki, J.F. Lechner and L.W. Jones. *Invest. Urol.* (1979) ; 17: 16-23

[7] R.M. Braun, P. Blenkinsopp, S.J. Mullock, C. Corlett, K.F. Wiley, J.C. Vickerman and N. Winograd. *Rapid commun. Mass Spectrom.* (1998) ; 12 (18) 1246.

[8] E.G. Jordan and C.A. Cullis. *The nucleolus*, Cambridge University Press (1982).

[9] A.M. Piwowar, N.P. Lockyer, J.C. Vickerman. *Analytical Chemistry* (2009) ; 81, 1040-1048

[10] S. Chandra and G.H. Morrison. *Int. J. Mass. Spectrom. Ion Processes* (1995) ; 143, 161-176

[11] X.A. Conlan, N.P. Lockyer, J.C. Vickerman. *Rapid Communications in Mass Sectrometry* (2006) ; 20, 8, 1327-1334

[12] I. Lanekoff, M.E. Kurczy, R. Hill, J.S. Fletcher, J.C. Vickerman, N. Winograd, P. Sjovall and A.G. Ewing. *Analytical Chemistry.* 82 (2010) p6652-6659

Chapter 5: The combined application of ToF-SIMS and FTIR in the spectral investigation of the cancer cell cycle

The following chapter aims to determine the influence of the various phases of the cell cycle, discussed earlier (Chapter 1.1.5), on the classification of ToF-SIMS spectral data. A good understanding of cell cycle progression is particularly important when characterising a cancer cell line. Cancer is defined by the loss of the ability to regulate cell division, therefore, investigations into the "modes of action" of chemotherapeutic agents – usually designed to target the cell cycle machinery – would benefit greatly from techniques that could not only chemically characterise the cell line in question, but also chemical responses to drugs.

A number of cancerous cell types in G1, S and G2/M growth phases were separated by FACS (Fluorescence activated cell sorting) or anticancer drug induced cell cycle arrest and subjected to ToF-SIMS analysis. In doing so, results indicate whether ToF-SIMS can detect surface biochemical changes induced by the cell cycle, and importantly, the extent to which this influences the classification of different cell types. Furthermore, the ToF-SIMS data obtained was compared to results obtained from synchrotron sourced FTIR microspectroscopy to assess the complementarities of the two approaches for cell line classification.

5.1 Experimental

5.1.1 FACS sorting

Cells from the A2780 human ovarian cancer epithelial cell line [1] were seeded in 25cm^3 sterile plastic culture flasks (Fisher Scientific, UK). After culturing (37^{0}C, 5% CO_2, in air) in media (RPMI-1640, 10% FCS and 2mM L-glutamine, Sigma Aldrich, UK) to around 80% confluency the media was removed. The cells were then washed in Dulbecco's Phosphate Buffered Saline (DPBS) (10ml, Sigma Aldrich, UK), after which 1ml trypsin solution (0.5 mg/ml trypsin; 0.2 mg/ml

EDTA in PBS, Sigma Aldrich, UK) was added and the cells were incubated (3 minutes, 37^0C, 5% CO_2, in air). The cells were then resuspended in the growth media (4ml) and removed for centrifugation. Once removed, the cell suspension was centrifuged (800 RPM, 5 minutes) and the supernatant discarded. The cells were then resuspended in DPBS (5ml) and centrifuged as before. Finally, the DPBS was removed and the cells were suspended – and fixed – in ethanol (4ml, 70% in HPLC grade water, Sigma Aldrich, UK).

The fixed cells were then centrifuged (800 RPM, 5mins) and the supernatant discarded. The resultant cell pellet was re-suspended in ice-cold PBS (10ml) and then centrifuged (800RPM, 5mins) to remove the media. Before the mixture was transferred to flow cytometry tubes it was incubated (37^oC, 15 mins, 5%CO_2 in air) with RNAse (150µl, 500mg/ml, DNAse free, from bovine pancreas). Following centrifugation (800RPM 5mins) to remove the media, the cells were re-suspended in a solution of propidium iodide in PBS (0.5ml, 50µl/ml) before FACS sorting (see section 3.3) using a FACSAria (BD biosciences, CA USA) into the different phases of the cell cycle (G1, S and G2/M). All samples prepared in this way will be referred to collectively as the FACS sorted data throughout.

5.1.2 Serum deprivation and anticancer drug induced cell cycle arrest

Cells from the A2780 human epithelial cell line were seeded on CaF_2 in sterile plastic 6 well plates for Infrared analysis (Fisher Scientific, UK). Due to the incompatibility of silicon wafer with cell adhesion and the possibility of changes in cellular biochemistry [2], samples were seeded in 25cm^3 sterile plastic flasks for SIMS analysis. After culturing (37^0C, 5% CO_2, in air) in media (RPMI-1640, 10% FCS and 2mM L-glutamine, Sigma Aldrich, UK) to around 60% confluency, the cells in different wells, or flasks, were then blocked into the various stages of the cell cycle by the following methods.

To synchronise the cells in G1 phase the media was replaced without adding 10% FCS. In doing so the cells are serum starved and become synchronised in G0/1 phase by the adverse growth conditions.

The remaining cells were blocked into S and G2/M phases by adding Combretastatin (G2/M blocker) or Methotrexate (S) for 24hours. Each drug was added to the culture media at ten times the IC50 value dissolved in DMSO. To ensure the drugs had worked flow cytometry was used (cells prepared as for FACS sorting) (table 5.1). It should be noted that it was difficult to distinguish between G2/M and S for methotrexate as it has a tendency to act in late S, early G2/M phase.

Control	Phase	Percentage of cell population
	G1	52%
	G2M	10%
	S	38%
Serum deprived		
	G1	67%
	G2M	18%
	S	15%
Combretastatin (100nM)		
	G1	7%
	G2M	74%
	S	19%
Methotrexate (400nM)		
	G1	1%
	S/G2M	99%

Table 5.1. Flow cytometry results and drug concentrations.

The flasks of cells were then prepared in suspension as in section 5.1.1 to be cytospun onto silicon wafer for SIMS analysis – discussed later. The sample set prepared in this way will be referred collectively to as the drug treated data throughout the discussion of results.

5.1.3 Sample preparation

Prior to sample preparation the substrate (silicon wafer, Agar Scientific Ltd, UK) was cleaned by sonicating 5 min in chloroform, washing twice in water and sonicating 5 min in ethanol. All solvents were HPLC grade (Sigma Aldrich, UK).

Cytospun cells were prepared using a Shandon Cytospin 4 Cytocentrifuge (Thermo Fisher scientific, MA, USA). Suspensions of sorted, or drug treated cells (150µl) were placed into the cytofunnels® and spun (800RPM, 5mins, low acceleration) onto cleaned Si wafer for ToF-SIMS analysis or calcium fluoride slides for FTIR analysis.

5.1.4 ToF-SIMS analysis

ToF-SIMS analysis was performed on a Bio-TOF SIMS instrument described earlier (section 3.1). The primary ion beam used for analysis was Au_3^+ as detailed below. For analysis a primary ion fluence of < 10^{13} ions/cm^2 was used to minimise sample damage due to gold bombardment. Images were taken over a 256 x 256 μm^2 field of view and delayed extraction was used. Ion detection was achieved using a dual microchannel plate operating at 20 keV post-acceleration. As in chapter 4.2, in an attempt to minimise the effects of variable surface coverage of cells between samples, spectra were extracted from images by selecting a 50 x 50 μm^2 area of biological interest. Relative ion yields were also calculated as a percentage of the total ions for that area, thus reducing the amount of signal from the silicon substrates.

5.1.5 FTIR analysis

FTIR microspectroscopy was performed primarily at the Elettra synchrotron facility detailed earlier (Chapter 3.1). Some preliminary experiments were also carried out at the Soleil synchrotron (chapter 3.1 and appendix 1). FTIR absorbance spectra were collected in transmission mode using a 20 x 20 μm^2 aperture. Spectra of single cells were taken by co-adding 512 interferograms at 8cm^{-1} spectral resolution. This spectral resolution was used to ensure water vapour artefacts were smoothed out.

5.1.6 ToF-SIMS data processing

Immediate processing was carried out using BioToF 8.1 software (Penn State, USA). This included highlighting 50 × 50 μm^2 areas of interest and extracting, and calibrating spectra. Rebin software (SurfaceSpectra, UK) was used to bin the data to 0.5 Da to increase signal intensity (figure 5.1). This works, for example by merging a peak that may span 10 spectral channels into 1 channel, therefore increasing the intensity of the peak by 10. However, it should be recognised that if part of the same peak were to fall outside the 10 then it could get incorporated into the next channel with a different peak. Binning the data to a low value can help to avoid this. Matlab™ paired with in-house written software (Royston Goodacre and Alex Henderson, University of Manchester) was used to remove Poisson noise (figure 5.2) [3]. This is necessary as all techniques that produce spectra from counts, e.g. of ions, are subject to variations in spectra. These variations are said to follow a Poisson distribution and are subsequently referred to as Poisson noise [4]. If they were not removed, PCA analysis may attempt to account for this variation, missing small, important chemical differences [4]. Again using Matlab™ paired with in-house written software (Royston Goodacre and Alex Henderson, University of Manchester) spectra were vector normalised to account for the possibility of instrumental drift and differences in the amount of sample (figure 5.3). Vector normalization is carried out by taking the average value of peak intensities and subtracting it from the spectrum such that a new average equals zero. The spectra are then scaled so that the sum squared deviation over the spectral range equals 1. Finally, square rooting the data increased the relative intensity of the high masses as they are often more diagnostic (figure 5.4). Spectra were then imported into pychem [5] for principal component analysis and discriminant function analysis.

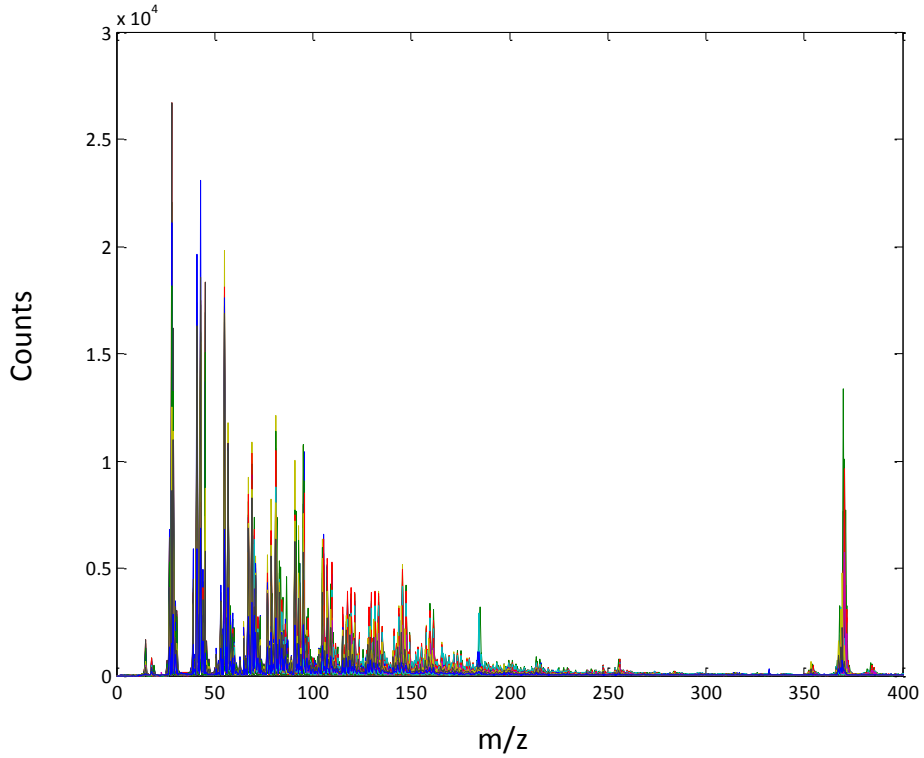

Figure 5.1. Overlaid positive SIMS spectra for G1, S and G2 phases of the cell cycle binned to 0.5 Da.

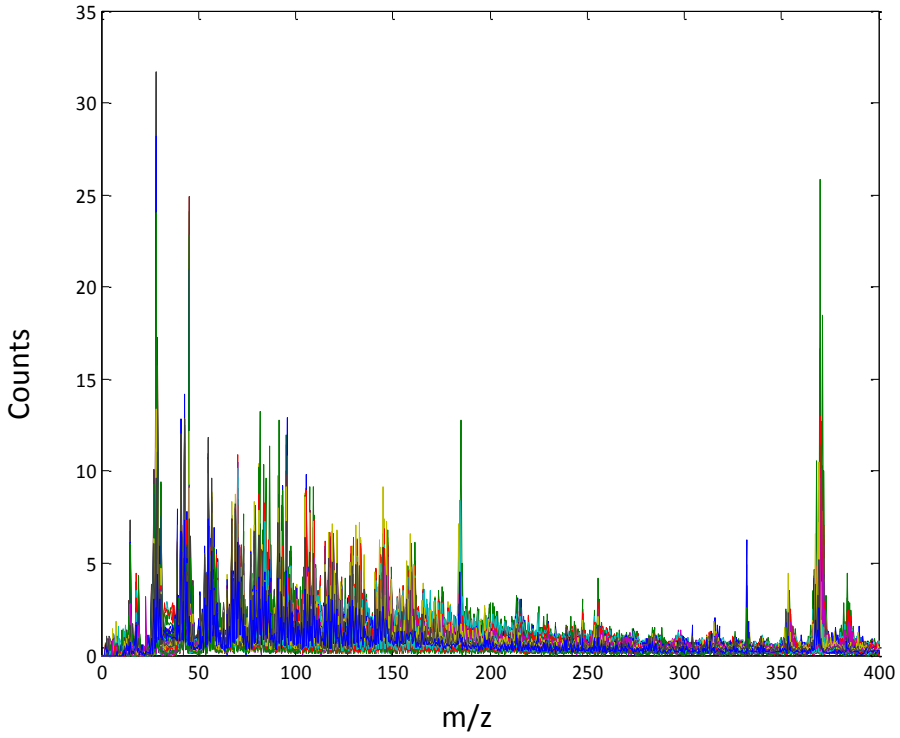

Figure 5.2. Overlaid positive SIMS spectra for G1, S and G2 phases of the cell cycle. Data has been binned (0.5 Da) and Poisson scaled.

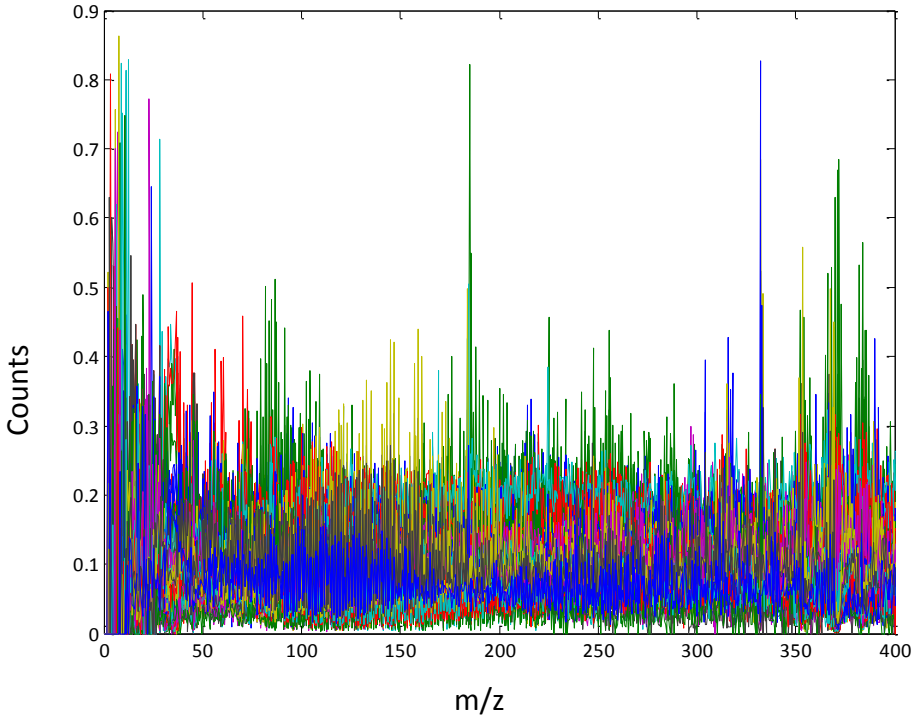

Figure 5.3. Overlaid positive SIMS spectra for G1, S and G2 phases of the cell cycle. Data has been binned (0.5 Da), Poisson scaled and vector normalised.

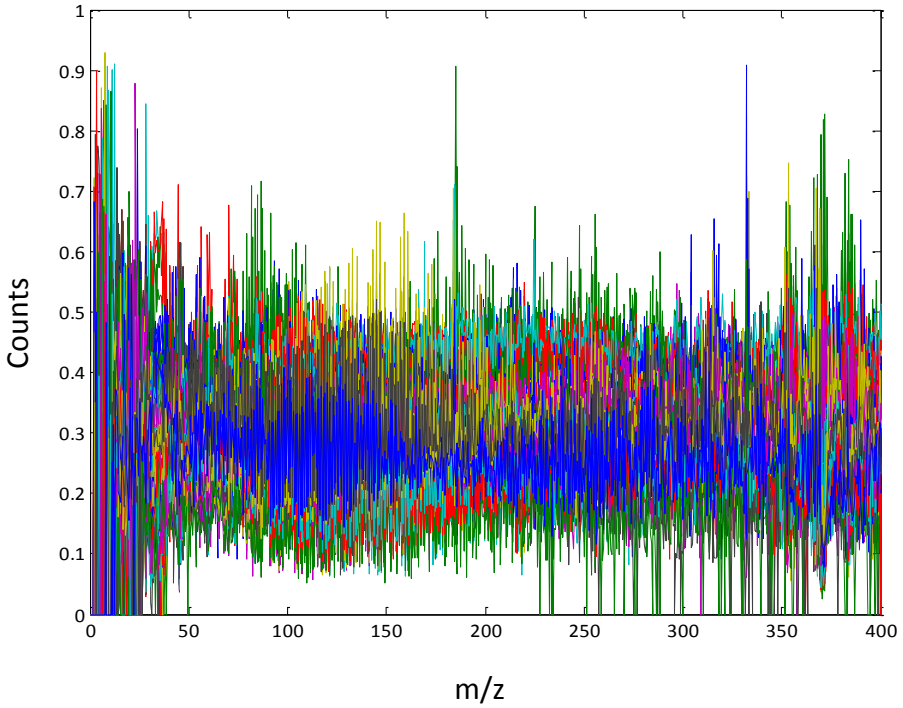

Figure 5.4. Overlaid positive SIMS spectra for G1, S and G2 phases of the cell cycle. Data has been binned (0.5 Da), Poisson scaled, vector normalised and square rooted.

5.1.7 FTIR data processing

Immediate processing to convert spectra from Opus files to a format compatible with Matlab™ was carried out using Opus 6.5 (Bruker Optik GmbH, Germany). Spectra (figure 5.5) were then corrected for Mie scattering and anomalous dispersion artefacts using the RMieS EMSC correction algorithm (10 iterations) paired with Matlab ™ [6]. After this, the corrected spectra (figure 5.6) were imported into PyChem [5] to perform principal component analysis and discriminant function analysis.

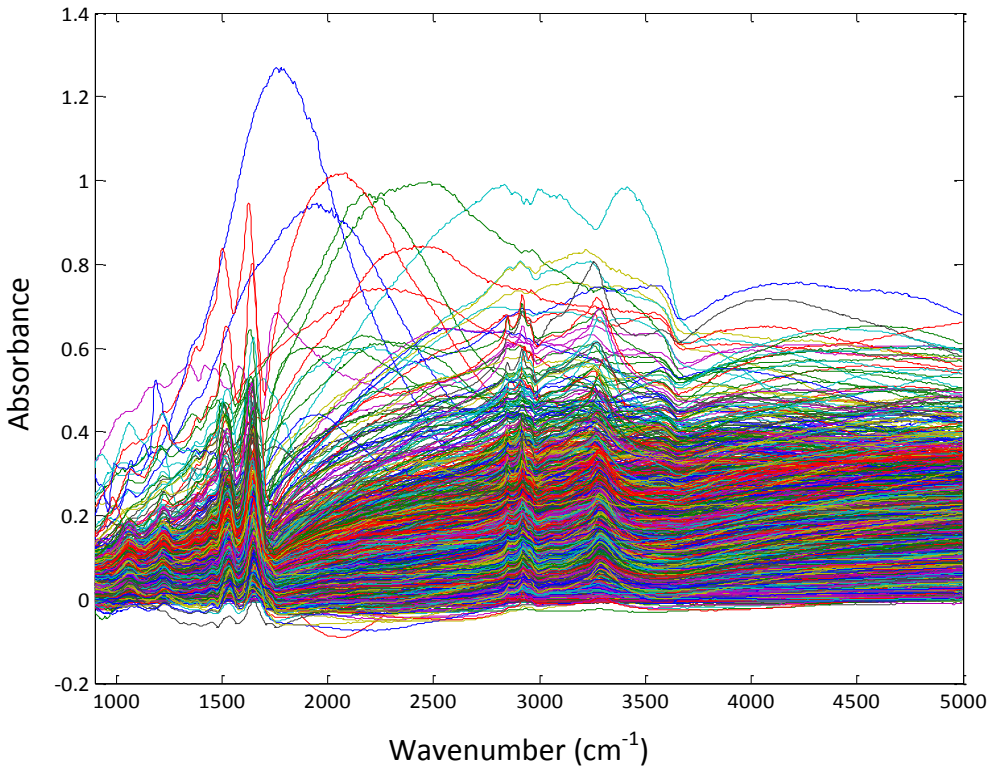

Figure 5.5. Uncorrected spectra for G1, S and G2 phases of the cell cycle.

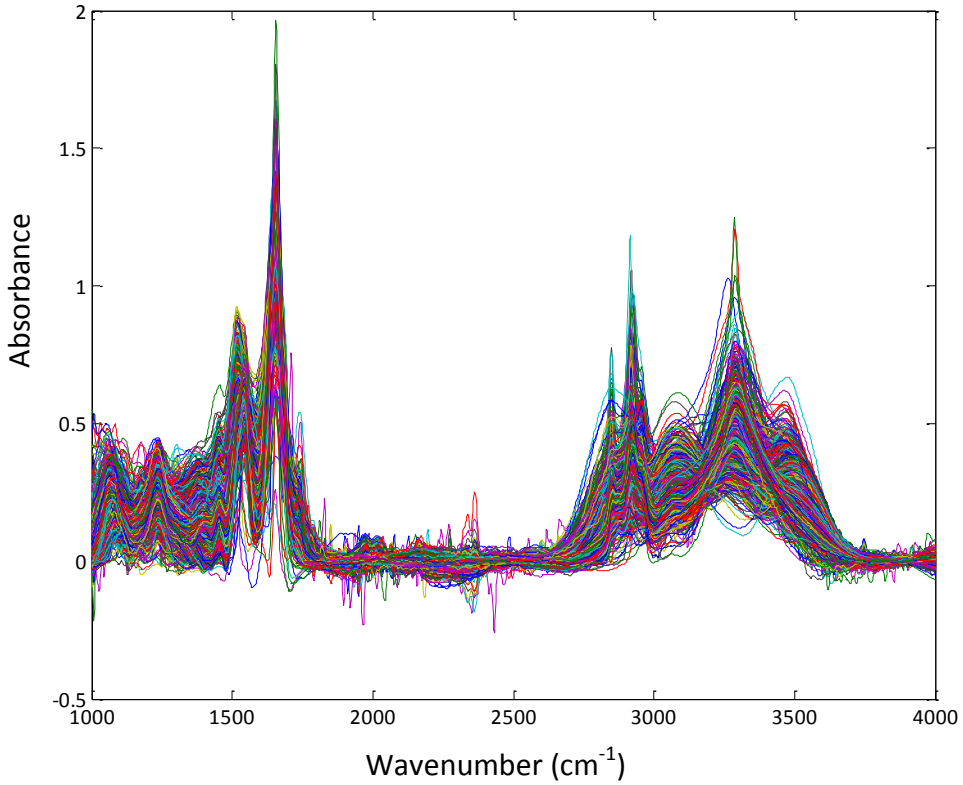

Figure 5.6. RMieS EMSC corrected spectra for G1, S and G2 phases of the cell cycle.

5.2 Results and discussion

As mentioned earlier in chapter 2, the literature pertaining to the ToF-SIMS and FTIR analysis of biological specimens demonstrates the suitability of these techniques for providing complementary information about subtle biochemical differences between biological specimens. Using methodologies developed previously (chapter 4), cytopsun cells were analysed using both FTIR and ToF-SIMS. Preliminary investigations into sample preparation (chapter 4) led to the development of a robust protocol with an appropriate cell line that was both amenable to FACS sorting and anticancer drug induced arrest. Using two different methods for producing known populations of cells in the various cycle phases allowed for a much more comprehensive and robust analysis of the cell cycle.

5.2.1 FTIR analysis of the cell cycle

As previously described, populations of cells were first divided into the different phases of the cell cycle using FACS. Figure 5.7 shows superimposed average spectra for G1, S and G2 phases. The differences between the various phases of the cell cycle manifest themselves principally in the regions associated with O-H and N-H stretching (3400 cm^{-1}); the CH stretching region mainly associated with lipids (also approximately 2800 – 3100 cm^{-1}); and, in the amide I,II and III bands (1655, 1517, 1320 cm^{-1} respectively). G1 phase exhibits a marked drop in intensity in both amide I and III regions with an increase in intensity in the amide II band (figure 5.8 (A)). Conversely, G2 phase exhibits a drop in the amide II region with a slight increase in signal from CH_3 bending modes from the methyl groups of proteins or COO^- vibration of fatty acids and amino acids (~1400 cm^{-1}) (figure 5.8 (A)) [6]. Furthermore, the amide I peak shows a low frequency shoulder at about 1740 cm^{-1} that is more pronounced in G1 phase and a broadening of the amide I around 1600 – 1635 cm^{-1} possibly due to changes in protein structure or nucleic acid content [7].

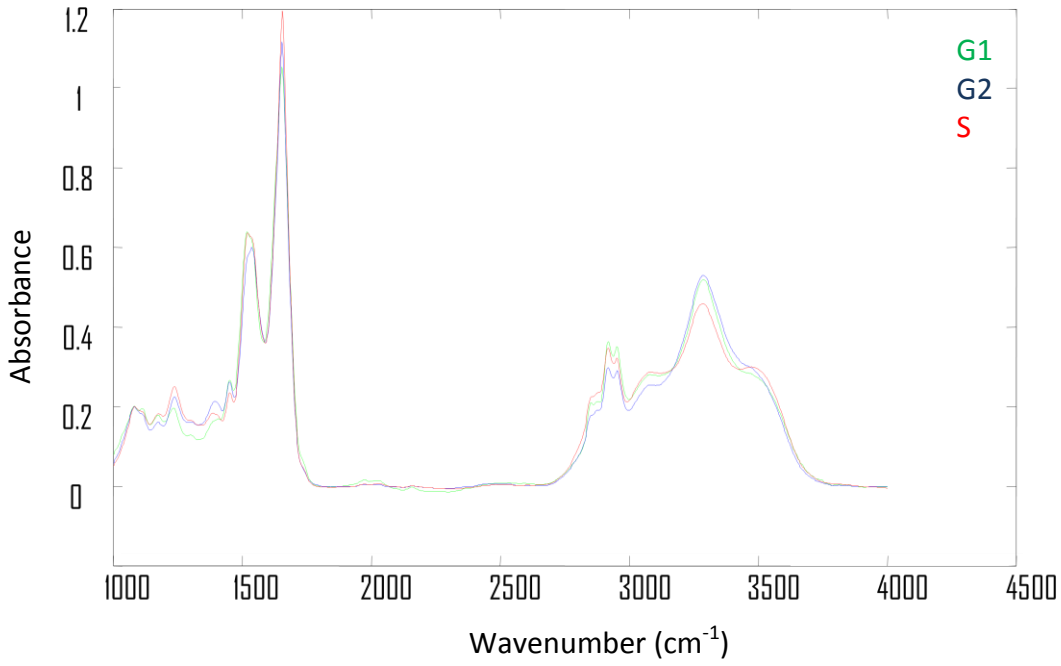

Figure 5.7. Superimposed average spectra of FACS sorted cells.

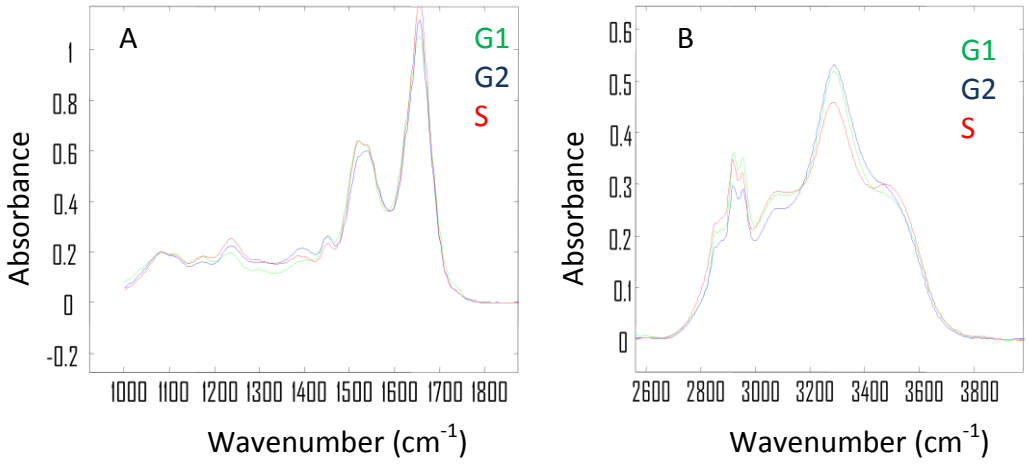

Figure 5.8. Fingerprint region (A) and lipid region (B) of superimposed spectra.

The spectral differences described are all relatively easily observed through the above figures, however, it should be reiterated that these were average spectra. Due to spectral heterogeneity such an approach is inappropriate as these differences are lost (figure 5.9).

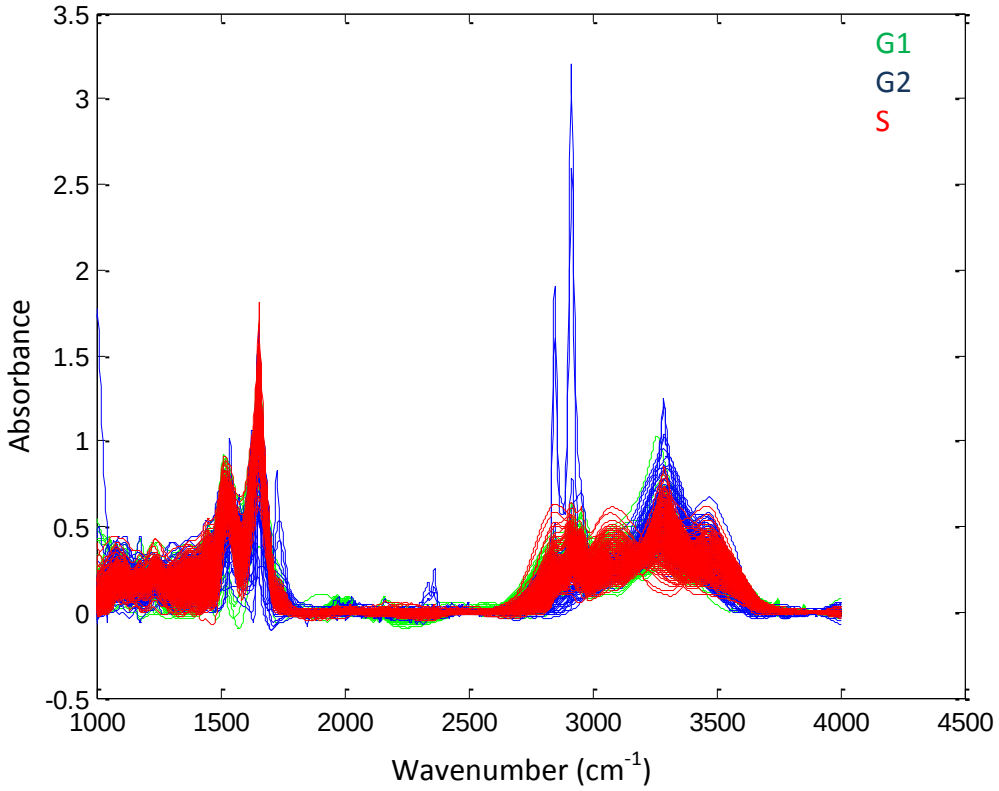

Figure 5.9. Individual superimposed spectra for G1, S and G2 phases.

A more suitable approach involves the use of multivariate statistics for interpretation of individual spectra (discussed later).

The same approach was then applied to the drug treated data (figure 5.10). Differences between the various phases of the cell cycle were again prominent in the regions associated with O-H and N-H stretching (3400 cm^{-1}); the CH stretching region mainly associated with lipids (also approximately 2800 – 3100 cm^{-1}); and, in the fingerprint region (1000 – 1800 cm^{-1}). However, G1 phase does not exhibit a marked drop in intensity in both amide I and III regions but still shows an increase in intensity in the amide II band (figure 5.11 (A)). G2 phase again exhibits a small drop, and new broadening, of the amide II band with a slight increase in signal from CH_3 bending modes from the methyl groups of proteins or COO^- vibration of fatty acids and amino acids (~1400 cm^{-1}) (figure 5.11 (A)). The amide I peak once more shows a low frequency shoulder at about 1740 cm^{-1} that is more pronounced in G1 phase, less so in G2 and absent in S.

Furthermore, G2 phase shows an increase in the signal from both the 3070 cm^{-1} and 3500 cm^{-1} regions (figure 5.11 (B)).

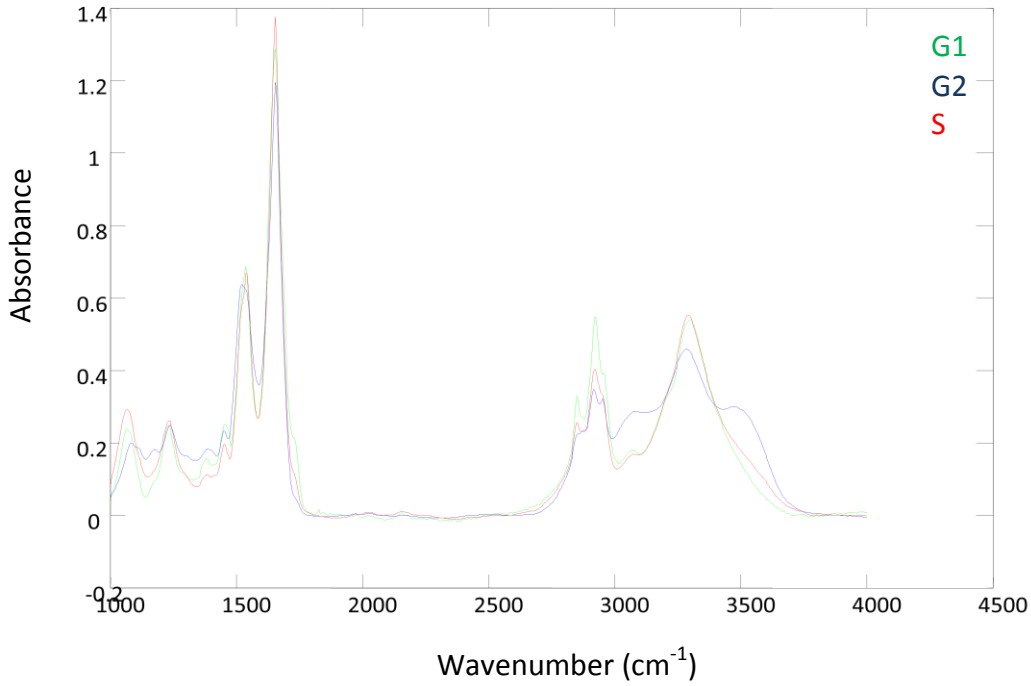

Figure 5.10. Superimposed average spectra of drug treated cells.

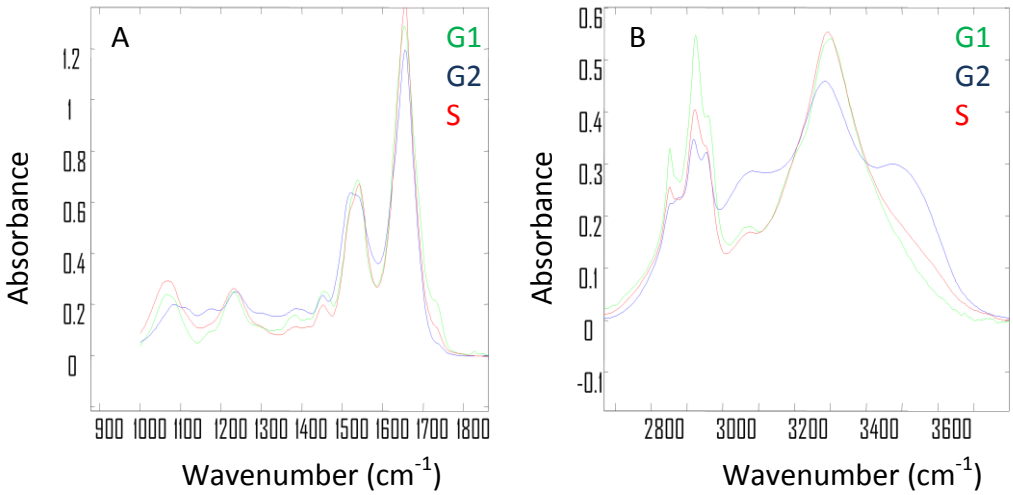

Figure 5.11. Fingerprint region (A) and lipid region (B) of superimposed spectra.

Spectral heterogeneity was not such an issue for the drug treated cells (figure 5.12), however, multivariate analysis will aid spectral interpretation. There are also several spectral features, such as high absorbances between 2800 and 2960

cm^{-1} and the presence of a large peak at 1460 cm^{-1}, that clearly require further investigation.

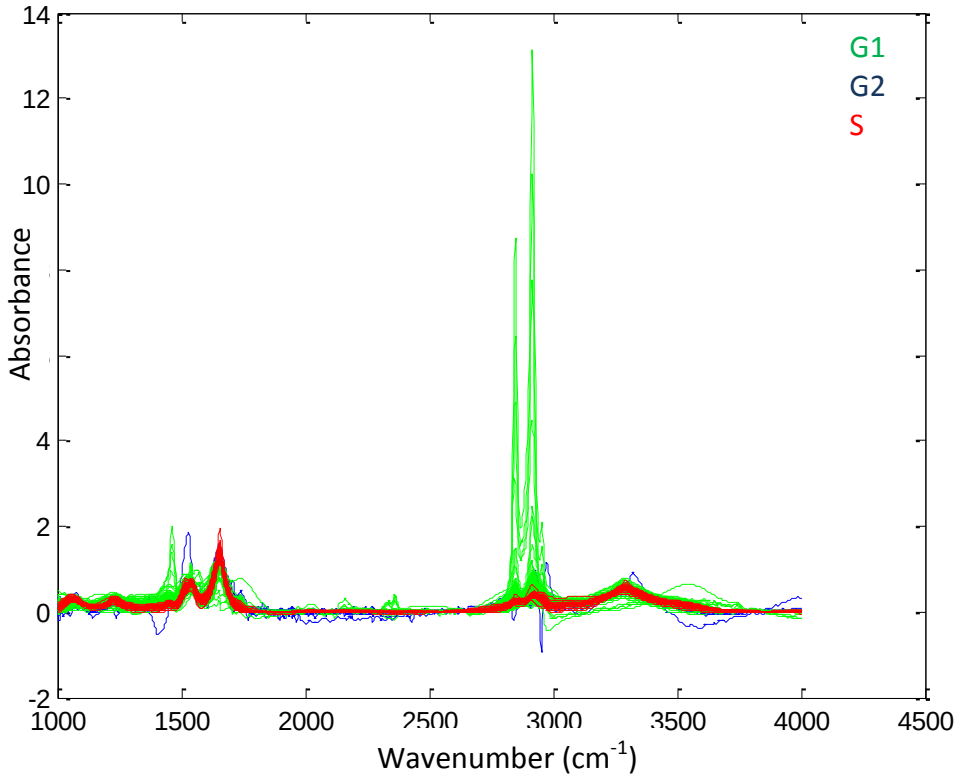

Figure 5.12. Individual superimposed spectra for G1, S and G2 phases of drug treated cells.

5.2.1.1 Multivariate analysis

Principal component analysis (PCA), as discussed earlier in section 1.4, is an unsupervised method used to aid in the identification of patterns in complex data sets and to visualise similarities and differences. In this case PCA was used to try to group the data into the phases of the cell cycle and elucidate the chemical differences between these groups. However, spectral heterogeneity again compounded the analysis. This is demonstrated in figure 5.13, where a PCA scores plot of the FACS sorted cell line is presented. Little separation is seen between the different groups indicating that a more powerful "supervised" method is required.

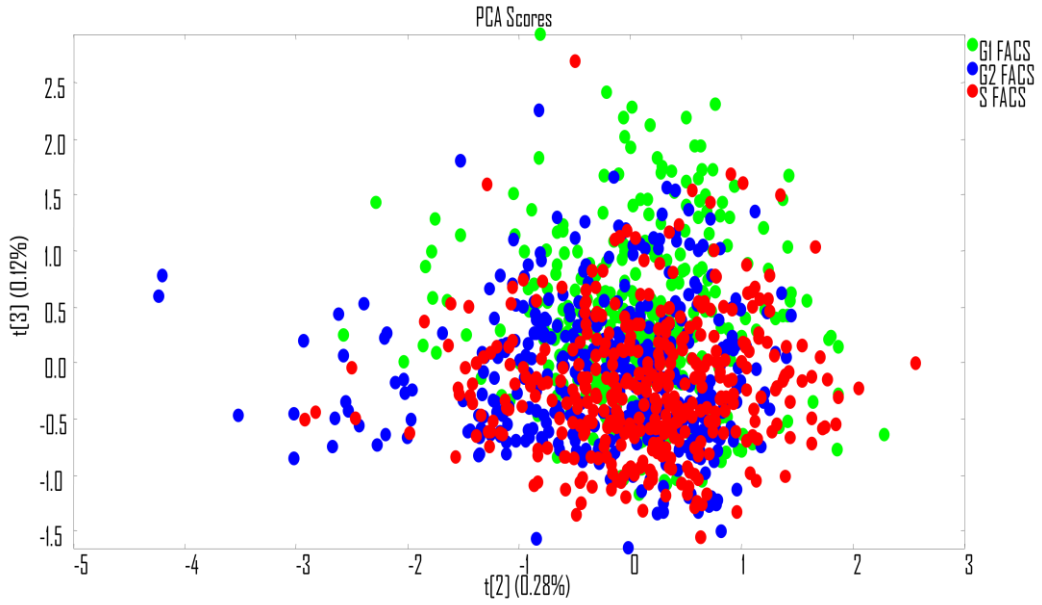

Figure 5.13. PCA scores plot (PC 3 vs 2) for FACS sorted cells.

Discriminant Function Analysis (DFA) essentially uses Principal Component analysis to first attempt to classify and reduce the dimensionality of the data. A selection of the data is then deliberately classified as G1, G2 or S and used to "train" the model. The remaining data is then introduced as the "blind" set and grouped based on the *a priori* knowledge of the training set. This is then validated by introducing a small validation set of completely blind data with no influence from the training set. Figure 5.14 shows a PC-DFA scores plot using 24 of the principal components from figure 5.13. The training set consisted of 70% of the data and the remaining 30% was a mix of the test set and validation set.

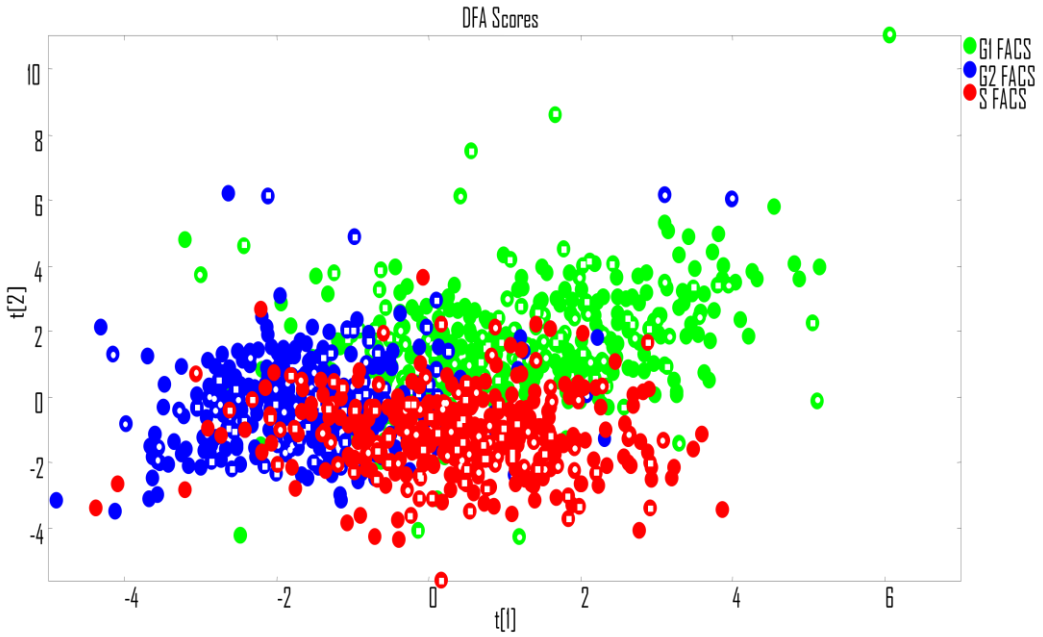

Figure 5.14. PC-DFA scores plot (DF 1 vs 2) for FACS sorted cells. Points with a white centre are the test set.

Clearly, despite a large amount of overlapping, PC-DFA has classified the spectra according to the cell cycle. This overlapping is to be expected as the bulk chemistry of the cell will remain relatively similar and FACS sorting is not 100% effective. These DFA results were produced from the whole spectral range with 1800-2500 cm^{-1} and above 3700 cm^{-1} removed. Therefore, any influences from atmospheric CO_2 and synchrotron noise were reduced. Figure 5.14 shows greatest separation between G1 and G2 along the first discriminant function and G1 and S phase along the second. Therefore, this result suggests little differences between G2 and S phase. This is probably due to the fact that most of the proteins and lipids used in G2 phase are synthesised in S phase.

PC-DFA of the drug treated data, again using 70% of the data as a training set, reveals much clearer separation between the various phases with only 10 principal components from the PCA (figure 5.15). This is probably due to the fact that the drug treated and serum starved cells will be arrested in a specific part of the cell cycle with the added influence of the drug chemistry. Similarities can still be drawn with the FACS sorted data as G1 and G2 phase again separate along

the first discriminant function and to a lesser extent G1 and S. In contrast to figure 5.14, however, the largest separation along the second discriminant function is between G2 and S.

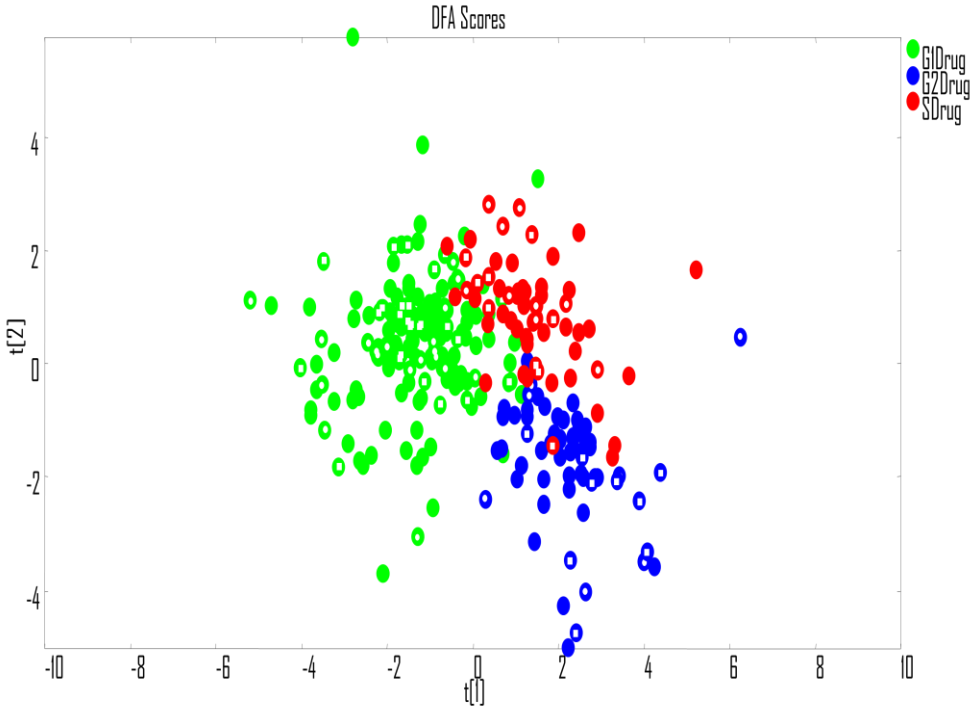

Figure 5.15. PC-DFA scores plot (DF 1 vs 2) for drug treated cells. Points with a white centre are the test set.

PC-DFA results indicate that sufficient spectral differences exist between the different phases to classify them for both FACS sorted and drug treated spectra. Each of the above discriminant functions has a corresponding loadings plot that contains information as to the spectral differences leading to the discriminations. To further investigate the reasons for the above classifications, the PC-DFA loadings plots were used to highlight the spectral differences between G1 and G2 (figure 5.16); G1 and S (figure 5.17); and G2 and S (figure 5.18) individually, for both sets of data. Principal components that most effectively described the differences between the samples were used. The PC-DFA loading plots shown (figures 5.16-5.18) not only indicate the spectral differences between cell cycle phases, but also highlight which differences are most important. Furthermore, differences present in both the FACS sorted and drug treated data are more likely to be related to the cell cycle phases.

Figures 5.16 – 5.18 are colour coded according to cycle phase. For example, all negative peaks, shaded blue, in figure 5.16 (A) are related to G2 phase and all positive peaks, again shaded blue, in figure 5.16 (B) are related to G2 phase. The following will discuss chemical differences between the cell cycle phases common to both drug treated and FACS sorted cells by identifying and tentatively assigning peaks present in both PC-DFA loading plots.

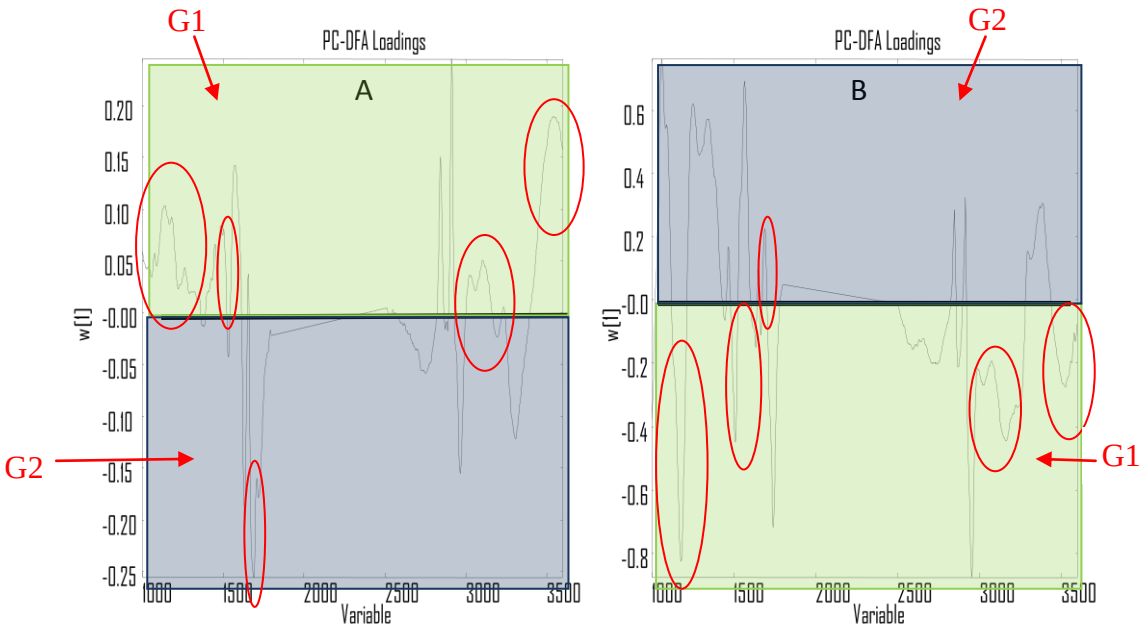

Wavenumber (cm^{-1}) Wavenumber (cm^{-1})

Figure 5.16. PC-DFA Loading plot showing differences between G1 phase (green) and G2 (blue) phase for drug treated (A) and FACS sorted (B) cells.

Despite the complexity of these figures some differences that are present in both plots have been identified (circled in red). The differences in figure 5.16 suggest changes in the DNA content of the cell, shown by a large peak around 1100-1200 cm^{-1} in G1 phase for both drug treated and FACS sorted cells. Similarly, but to a slightly lesser extent, part of the amide II band around 1517 cm^{-1} and the region corresponding to N-H stretching vibrations for proteins (3400-3500 cm^{-1}) is also prominent in G1 phase. However, the amide I region (1650 cm^{-1}) appears to be contributing highly to chemical differences associated with G2 phase. Finally, the doublet peak at 3050-3100 cm^{-1} suggests changes in

lipids, or possibly further differences associated with N-H stretching modes of proteins [7]. Importantly, these findings support those observed earlier in the overlaid average spectra.

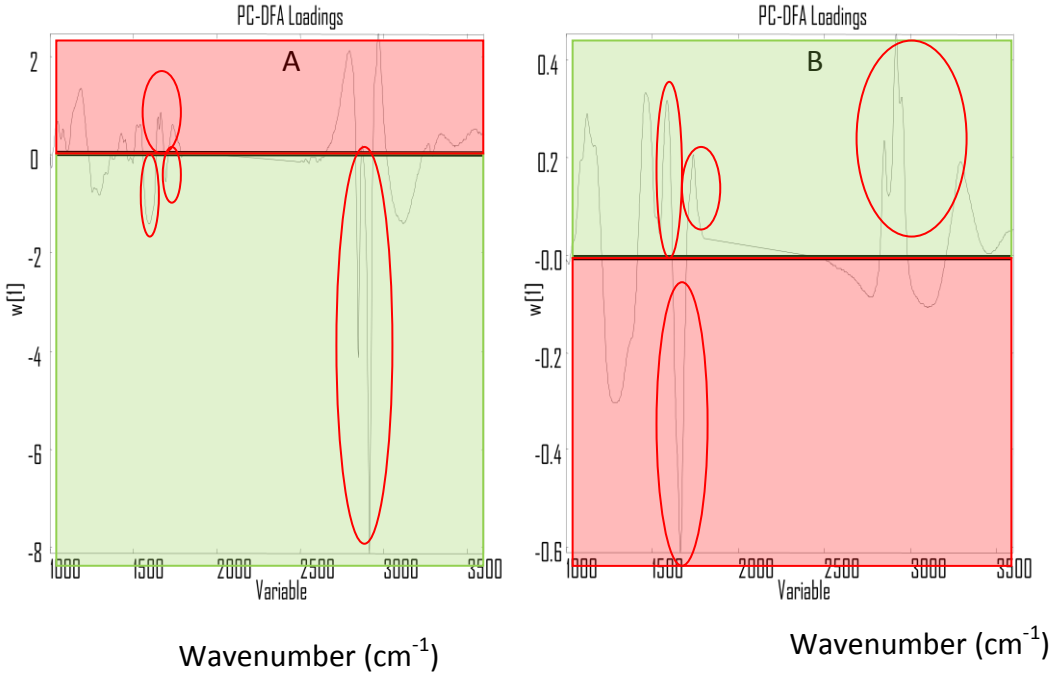

Figure 5.17. PC-DFA Loading plots showing differences between G1 phase (green) and S phase (red) for drug treated (A) and FACS sorted (B) cells.

Figure 5.17 (A) and (B) appear to be much more similar than figure 5.16. Important differences are once more circled in red. The most prominent peaks causing the separation between G1 and S phase appear to be lipid, or fatty acid related with a large scissoring doublet (2800-3000 cm^{-1}) associated with the CH_3 and CH_2 groups of lipid alkyl chains and a smaller C=O stretching band at 1740 cm^{-1}. The amide I peak (1650 cm^{-1}) is also adding to chemical differences related to S phase.

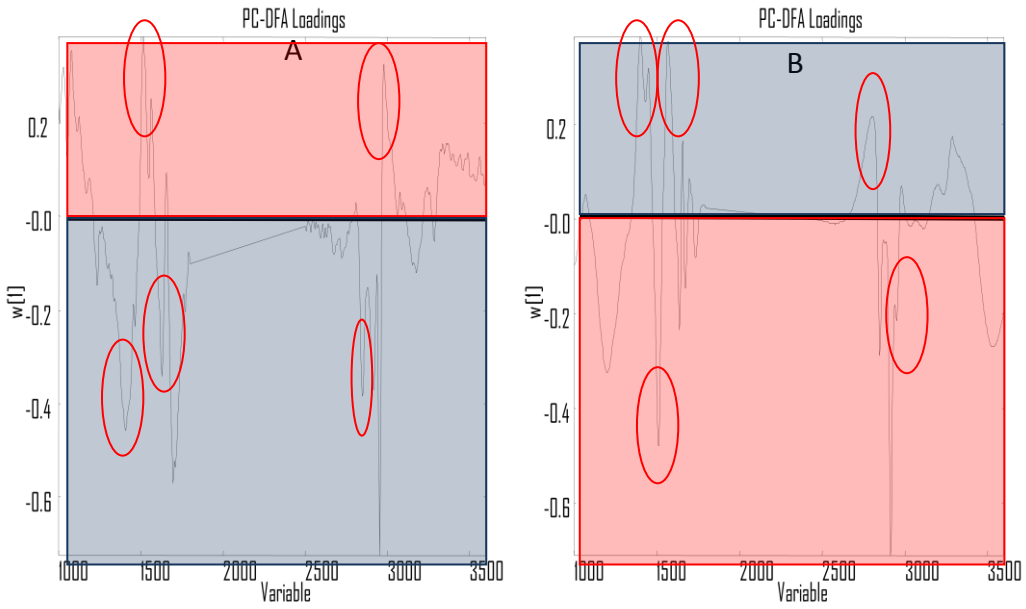

Wavenumber (cm^{-1}) Wavenumber (cm^{-1})

Figure 5.18. PC-DFA Loading plots showing differences between G2 phase (blue) and S phase (red) for drug treated (A) and FACS sorted (B) cells.

Finally, the differences in figure 5.18 highlight a change in the lower part of the amide II signal, and possibly also methyl groups of proteins from S to G2 (1400-1450 cm^{-1}). This could indicate protein methylation, which would occur in G2 phase for entry into mitosis [8]. This is supported by the presence of a peak in the CH_3 stretching region around 2850 cm^{-1} in G2 phase in both (A) and (B) (figure 5.18). The other side of the Amide II region (1540 cm^{-1}), however, appears to contribute strongly to chemistry linked with S phase. This is most likely due to changes in protein conformation. Again, this is reinforced by a sharp amide I peak around 1650 cm^{-1}.

In summary, it is clear that changes in the FTIR spectra as a result of chemistry, as the cell progresses through the growth cycle, are complex. The data suggests FTIR is capable of detecting subtle changes in DNA, Lipid and protein chemistry and structure. These chemical differences combined were significant enough to group cells of the same cycle phase supporting the findings of other similar investigations [9,10,11] confirming that each phase can be characterised and identified spectrally. Furthermore, the use of more sophisticated data

processing techniques allowed for a much more robust analysis than those previously reported in the literature.

5.2.2 ToF-SIMS analysis of the cell cycle

The following reports the findings from the ToF-SIMS investigation of the drug treated and FACS sorted cell lines. Overlays of average positive (figures 5.19 and 5.20) and negative (figures 5.22 and 5.23) ion spectra of the two sample sets are shown. In the positive spectra (figures 5.19 and 5.20), a significant peak representing cholesterol is seen at m/z 369 [M-OH]. On further inspection of these spectral overlays - and relative ion yields (discussed later) -, it appeared that, despite differences in G1 and G2 phases, the levels of cholesterol were at their highest in S phase for both sample sets (figure 5.21). Many other subtle spectral differences are also observed throughout the whole mass range; however, it is difficult to know which are relevant to the cell cycle. The use of multivariate analysis is again a much more appropriate method for extracting significant differences between the various cycle phases.

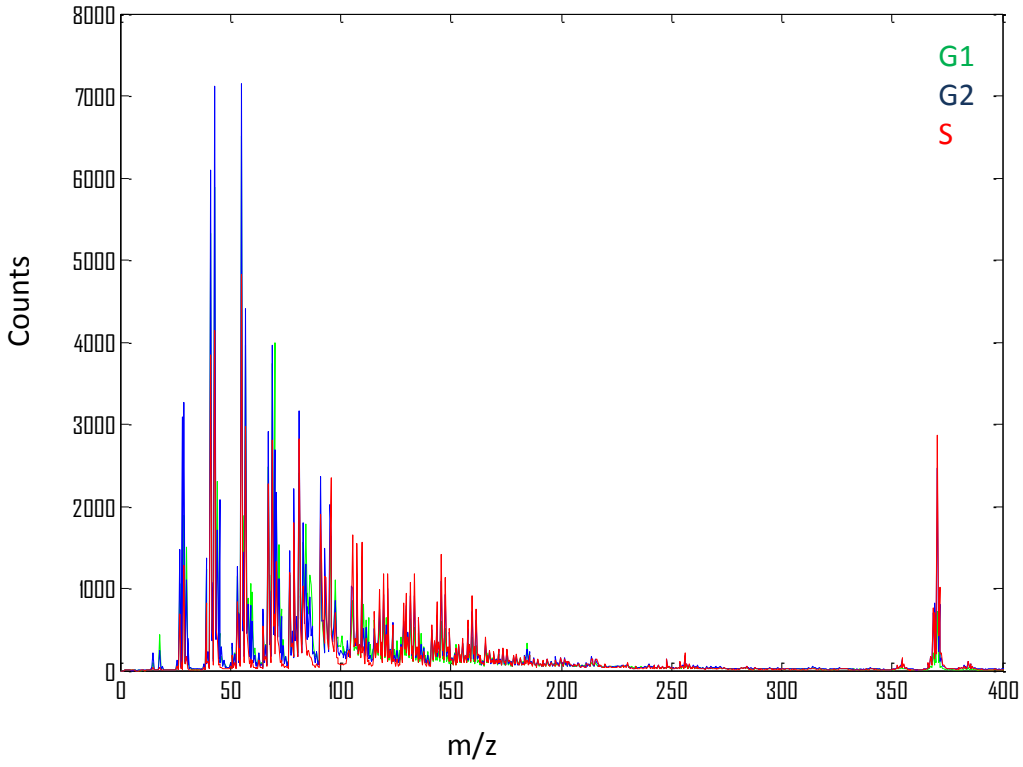

Figure 5.19. Overlay of averaged drug treated spectra (positive ion mode).

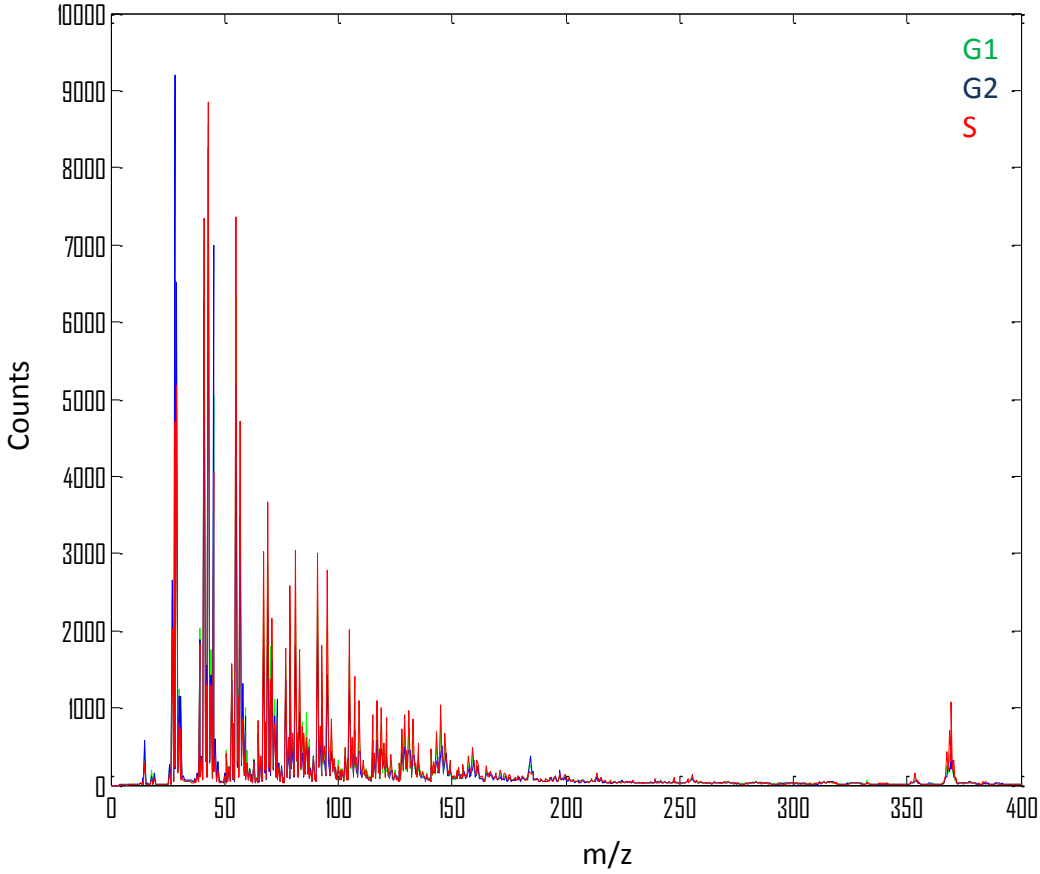

Figure 5.20. Overlay of averaged spectra for FACS sorted cells (positive ion mode).

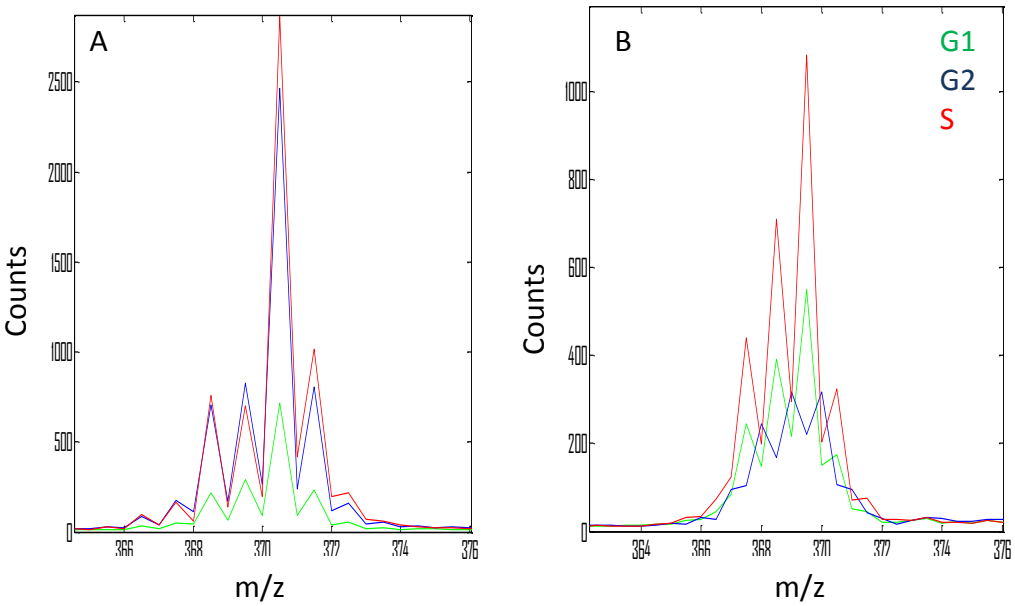

Figure 5.21. Cholesterol region for drug treated (A) and FACS sorted (B) spectral overlays.

Similarly, initial inspection of the average negative ion spectra (figures 22 and 23) reveals many chemical differences; nevertheless, none are as easily identifiable as cholesterol between the two sample sets. Again, interpretation of spectra in this way is difficult for such an information rich technique. To this end, the use of multivariate analysis is a much more appropriate method for extracting significant differences between the various cycle phases.

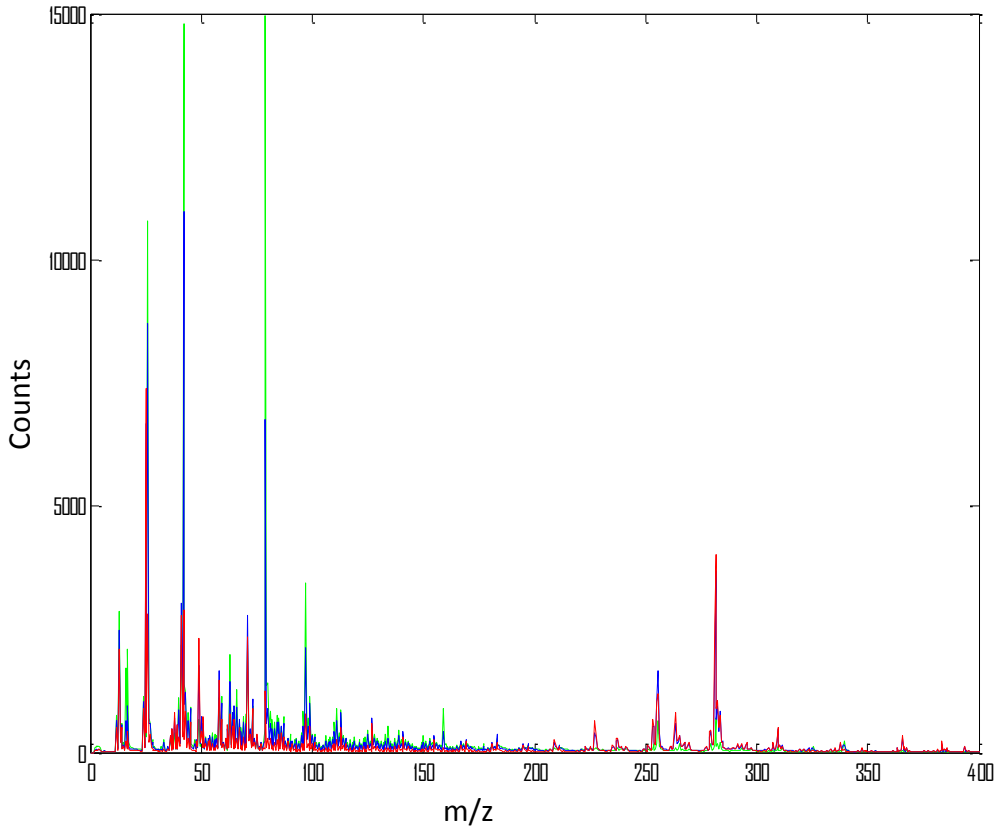

Figure 5.22. Overlay of average drug treated spectra (negative ion mode).

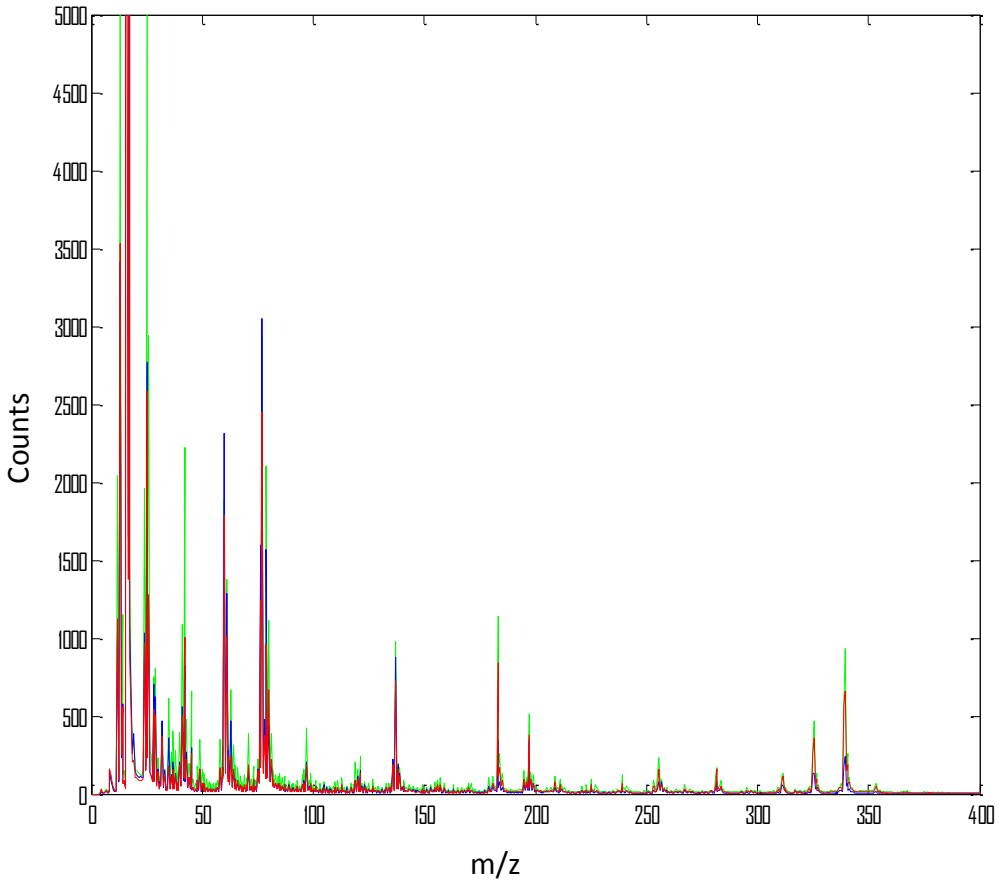

Figure 5.23. Overlay of averaged spectra for FACS sorted cells (negative ion mode).

5.2.2.1 Multivariate analysis

Principal Component-Discriminant Function Analysis (PC-DFA) was used for ToF-SIMS data as for the FTIR analysis. The drug treated data was fed into the DFA programme using 4 principal components for positive and 3 for negative spectra with two discriminant functions (figure 5.24). In this case the training set was made up of 50% of the data and the remaining 50% was a mix of the test set and validation set. Figure 5.24 shows a high degree of separation between the different drug arrested cells. These results were produced across the complete spectral range after poisson scaling, normalising and square rooting, as previously described. In doing so, it is hoped the influence of any instrumental instabilities were reduced, therefore increasing the weight of chemical differences. Figure 5.24 (A) suggests G1 and G2 phases are more chemically

similar to each other than to S phase. Both are separating away from S phase along the first discriminant function and from each other along the second. The negative ion mode data (figure 5.24 (B)) shows three equally distinct groups, however, they are all discriminating along the first discriminant function.

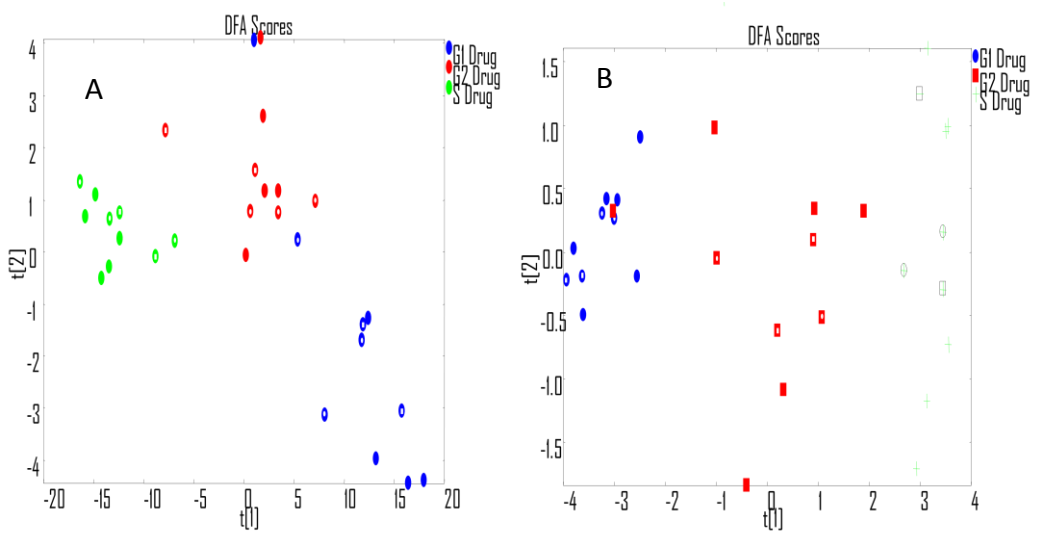

Figure 5.24. Positive (A) and negative (B) ion mode PC-DFA scores plots (DF 1 vs 2) for drug treated cells. Points with a white centre are the test set.

PC-DFA of the FACS sorted data, again using 50% of the data as a training set, reveals much less separation between the various phases with 6 principal components for positive and 8 for negative spectra from the PCA (figure 5.25). It is difficult to draw similarities with the drug treated data due to the high degree of overlapping as with the FTIR data, however G1 and G2 phase again appear to be loosely situated within the positive region of the first discriminant function and S in the negative region in positive ion mode. Similar clustering is also observed from the negative ion mode data (figure 5.25 B).

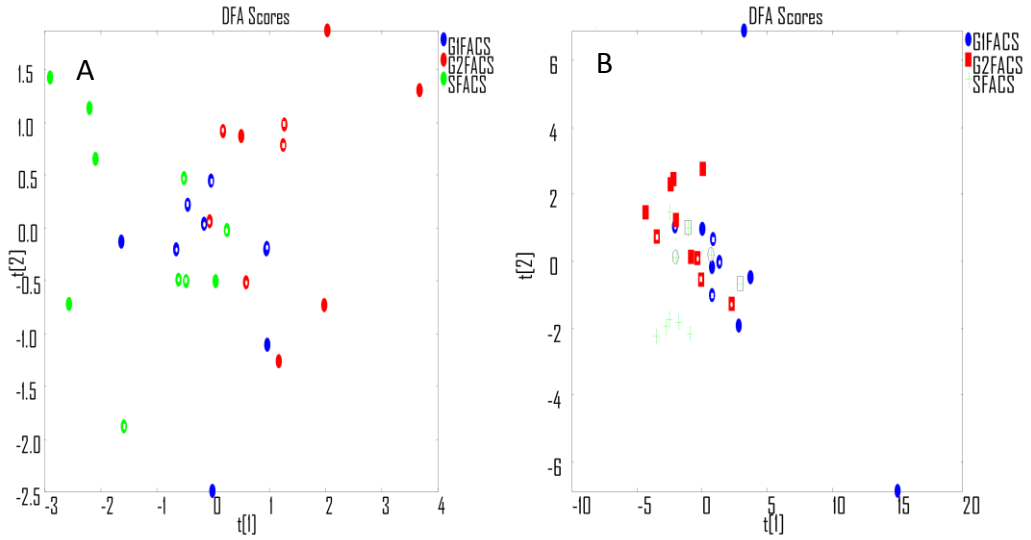

Figure 5.25. Positive (A) and negative (B) ion mode PC-DFA scores plot (DF 1 vs 2) for FACS sorted cells. Points with a white centre are the test set.

As with the infrared data, PC-DFA has proven a useful tool for indicating differences between spectra that are too complex to observe within the raw data alone. To further investigate the chemical differences between the cell cycle phases loadings plots were used to visualise the spectral differences between G1 and G2 (figure A.1.1 and A.1.2); G1 and S (figure A.1.3 and A.1.4), and G2 and S (figure A.1.5 and A.1.6) individually, for both sets of data (see appendices). However, the SIMS loadings plots still contain a large amount of complex information. To interpret and present this data in a more suitable format table 5.2 and the relative ion yields are presented to essentially summarise the main differences from the discriminant function loadings plots common to both FACS sorted and drug treated cell populations. Previously reported SIMS studies were used as a guide to select a range of significant peaks from the PC-DFA loadings plots. These were thought to be representative of chemical changes related to each cycle phase (table 5.2). The static SIMS library (SurfaceSpectra Ltd, UK) was then used to help with peak assignment and relative ion yields were calculated to determine the levels of each chemical as

the cell progresses through the growth cycle. Furthermore, using the static SIMS library it was possible to tentatively assign chemical formulae to the species observed. However, due to the complexity of cell chemistry and the ToF-SIMS technique it should be reiterated that one cannot claim these assignments to be 100% accurate. This is, unfortunately, reflected in the relative ion yields, which, at first sight are not always consistent between polarities, as with the lipid data (discussed later). This could be because the data was binned to 0.5 Da so two adjacent peaks may well have been combined. For example, m/z 117 is reported twice in table 5.2 as it was thought to be related to either deoxycytidine or maleic acid, or both. It is most likely that binning the data in this way does not give a detailed enough view, due to reduced mass resolution, resulting in the loss of certain finer details. This is perhaps compounded further by the influence of the drugs on SIMS spectra and possible matrix effects, which could have caused increases or decreases in ionization probabilities in one polarity more than another. Nevertheless, some interesting, reasonable observations can still be reported.

Compound	Peak	Structure	Polarity	Cycle Phase
DPPC	224	$[C_8H_{19}PO_4N]+$	+	G2
(733.56gmol^{-1})	166	$[C_4H_{13}NO_3P]+$	+	G2
	137	$[C_3H_6PO_4]-$	-	G2
	123	$[C_2H_4PO_4]-$	-	G2
DPPE	283	$[C_{18}H_{35}O_2]+$	+	G2
(719.55gmol^{-1})	210	$[C_{15}H_{30}]+$	+	G2
	208	$[C_7H_9PO_4N]-$	-	G2
	168	$[C_4H_{11}PO_4N]-$	-	G2
Lauric acid	183	$[C_{12}H_{23}O]+$	+	G2
(200.32gmol^{-1})	201	$[C_{12}H_{25}O_2]+$	+	G2
	199	$[C_{12}H_{23}O_2]-$	-	G2
	399	$[C_{24}H_{47}O_4]$	-	G2
Maleic acid	99	$[C_4H_3O_3]+$	+	G2
(116.07gmol^{-1})	117	$[C_4H_5O_4]+$	+	G2
	233	$[C_8H_9O_8]+$	+	G2
	347	$[C_{12}H_{11}O_{12}]-$	-	G2
	231	$[C_8H_7O_8]-$	-	G2
Stearic acid	285	$[C_{18}H_{37}O_2]+$	+	G2
(284.48gmol^{-1})	283	$[C_{18}H_{35}O_2]-$	-	G2
	267	$[C_{18}H_{35}O]-$	-	G2
Cholesterol	369	$[C_{27}H_{45}]+$	+	S
(386.65gmol^{-1})				
Tryptophan	205	$[C_{11}H_{13}N_2O_2]+$	+	S
(204.23gmol^{-1})	188	$[C_{11}H_{12}N_2O]+$	+	S
	130	$[C_9H_8N]+$	+	S
	203	$[C_{11}H_{11}N_2O_2]-$	-	S
Methionine	299	$[C_{10}H_{23}N_2O_4S_2]+$	+	G1
(149.21gmol^{-1})	150	$[C_5H_{12}NO_2S]+$	+	G1
	133	$[C_5H_{12}NOS]+$	+	G1
	297	$[C_{10}H_{21}N_2O_4S_2]-$	-	G1
	148	$[C_5H_{10}NO_2S]-$	-	G1
Deoxycytidine	250	$[C_8H_{11}N_4O_4Na]+$	+	G1
(228.2gmol^{-1})	117	$[C_5H_9O_3]+$	+	G1
	112	$[C_4H_6N_3O]+$	+	G1
	226	$[C_8H_{10}N_4O_4]-$	-	G1
	110	$[C_4H_4N_3O]-$	-	G1
Arginine	175	$[C_6H_{14}N_4O_2]+$	+	S
(174.2gmol^{-1})	87	$[C_4H_{11}N_2]+$	+	S
	70	$[C_4H_8N]+$	+	S
	173	$[C_6H_{13}N_4O_2]-$	-	S
	131	$[C_5H_{11}N_2O_2]-$	-	S

Table 5.2. Summary of main peaks observed in PC-DFA loading plots. The SIMS polarity and relevant cell cycle phase are given for each peak.

As the peaks in table 5.2 were chosen from the PC-DFA loading plots, it is fair to say they can be used to describe the chemistry relevant to the different cycle phases. Therefore, table 5.2 suggests G2 phase, for example, can be characterised by variations in the yields of phospholipids (DPPE and DPPC) and fatty acids (Lauric, Maleic and Stearic acid). Interestingly, the FACS sorted data (figures 5.27 and 5.29) shows a slight increase in levels of DPPC (positive m/z 224, 166 and negative m/z 137, 123) from G1 to G2. However, the drug treated data (figures 5.26 and 5.28) shows slightly higher DPPC signal (positive m/z 224,166 and negative m/z 137,123) in G1 than in G2. This is most likely due to an effect of combretastatin, which was used to block the cells in G2 phase. As combretastatin works by binding to tubulin, and consequently, disrupts microtubule synthesis, this would have prevented the cells from completing the biological the biological preparations for mitosis. It is, therefore, almost certainly responsible for the drop in lipids seen as the cell progresses into G2 phase where it is blocked.

Figures 5.26-5.29 all show an increase in yields of certain fatty acid peaks (positive m/z 117, 201 and negative m/z 399, 347, 283, 267) from G1 to S phase, which is probably accurate as cells would be essentially doubling levels of these for the production of a second cell membrane [12].Similarly, an increase in the average cholesterol yield (m/z 369) is observed from G1 to S with a slight decrease from S to G2 (figures 5.26 and 5.27). This is probably due to the fact that cholesterol is not only an integral part of the cell membrane, but also an important precursor to DNA synthesis. Therefore, levels would increase in preparation for membrane construction and DNA synthesis and then decrease as some is used for DNA synthesis [13]. However, the large overlapping error bars in figures 5.26 and 5.27 suggest these differences are not statistically significant.

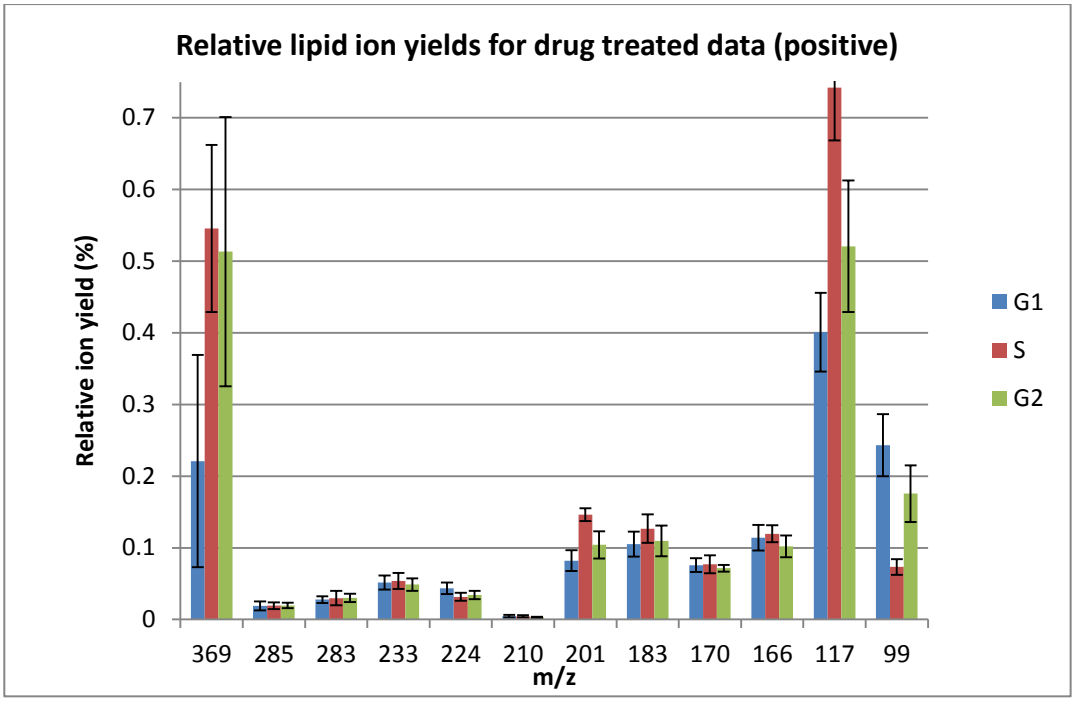

Figure 5.26. Lipid and fatty acid relative ion yields for positive drug treated data. The data are presented as means ± s.d (n=10).

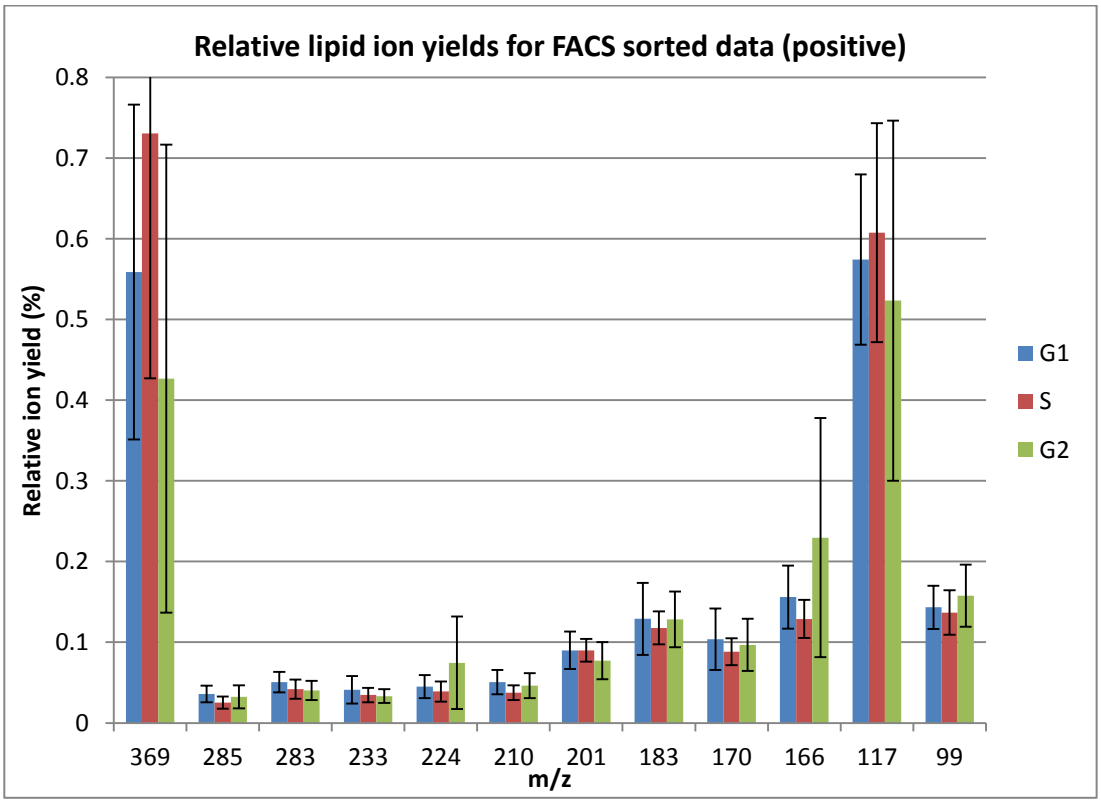

Figure 5.27. Lipid and fatty acid relative ion yields for positive FACS sorted data. The data are presented as means ± s.d (n=10).

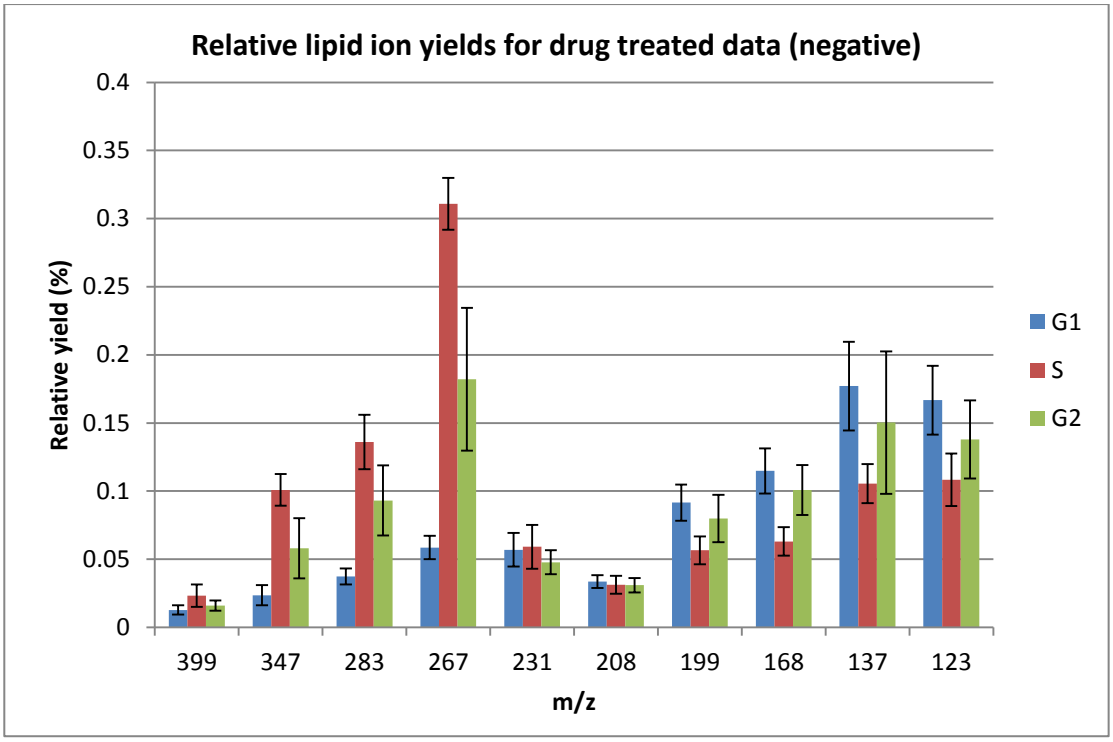

Figure 5.28. Lipid and fatty acid relative ion yields for negative drug treated data. The data are presented as means ± s.d (n=10).

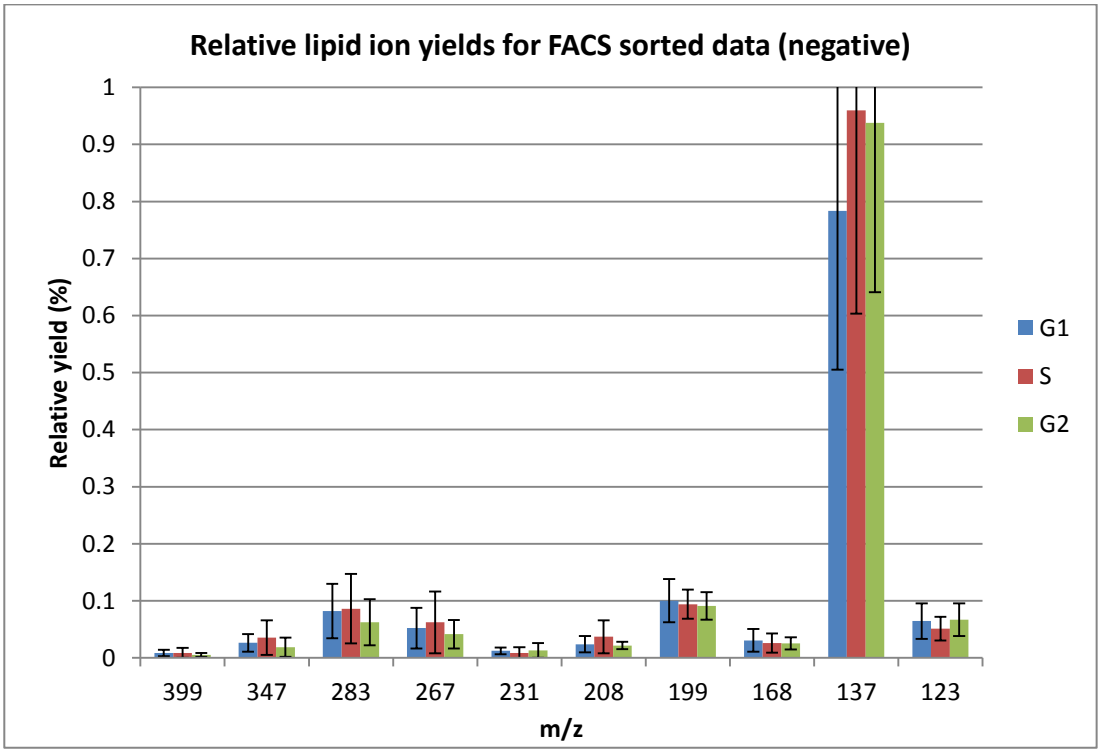

Figure 5.29. Lipid and fatty acid relative ion yields for negative FACS sorted data. The data are presented as means ± s.d (n=10).

Generally, the levels of amino acids and bases for the FACS sorted data (figures 5.31 and 5.33) increase from G1 to S and some either continue increasing or drop off into G2 phase. The drug treated data (figures 5.30 and 5.32), however, shows a sharp drop in amino acid yields during S phase (positive m/z 112, 87, 70 and negative m/z 203, 173, 148, 131, 110). This could again be a result of the effects of the anticancer drug, in this case, methotrexate, which works by inhibiting the folic acid pathway and DNA production. This could then have a knock-on effect on amino acid metabolism.

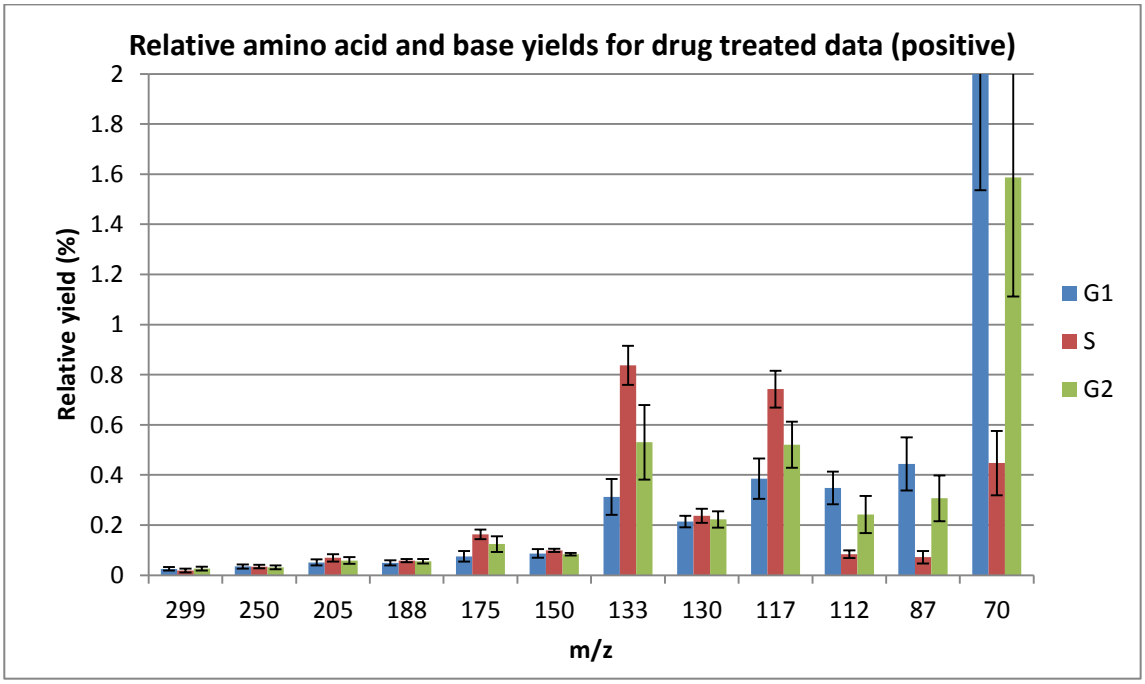

Figure 5.30. Amino acid and base relative ion yields for positive drug treated data. The data are presented as means ± s.d (n=10).

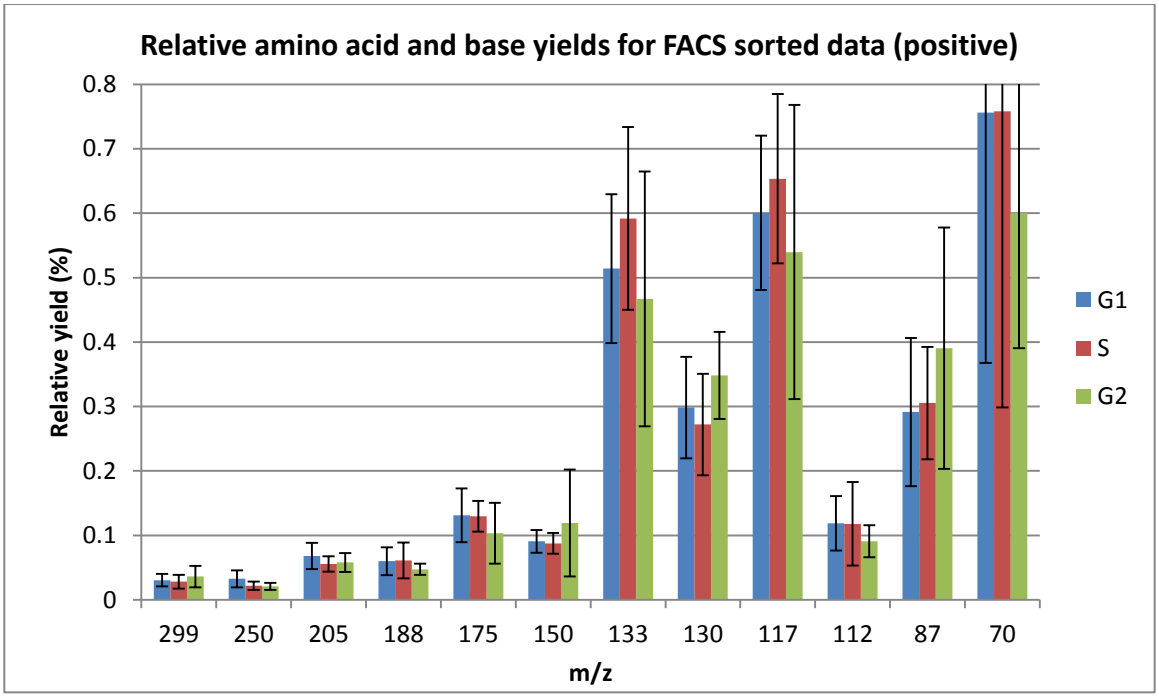

Figure 5.31. Amino acid and base relative ion yields for positive FACS sorted data. The data are presented as means ± s.d (n=10).

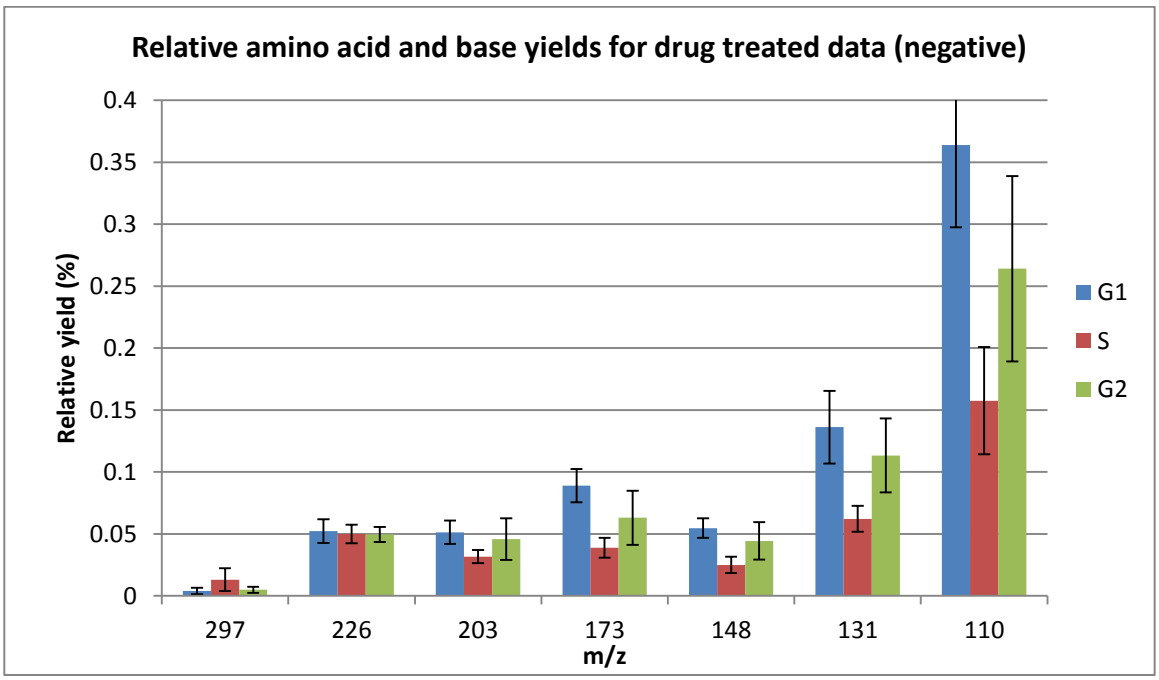

Figure 5.32. Amino acid and base relative ion yields for negative drug treated data. The data are presented as means ± s.d (n=10).

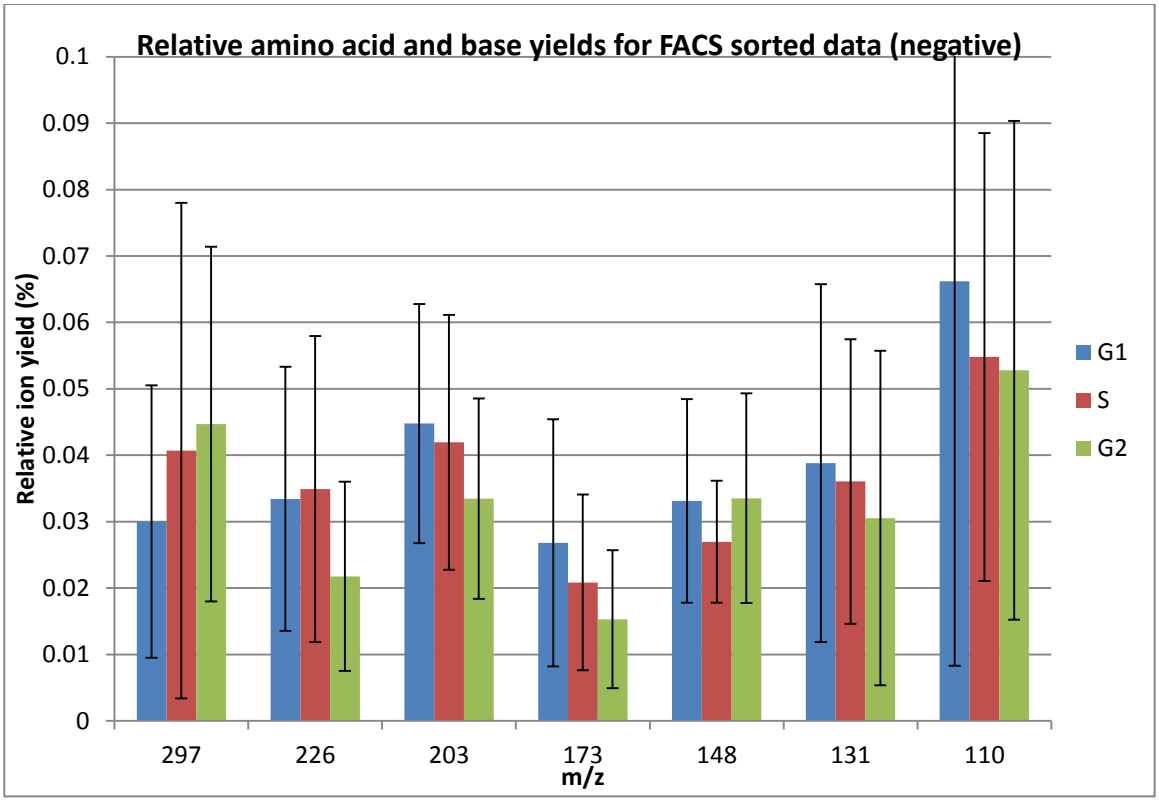

Figure 5.33. Amino acid and base relative ion yields for negative FACS sorted data. The data are presented as means ± s.d (n=10).

5.3 Conclusions

As mentioned earlier, previous FTIR work in this field has not been able to provide a comprehensive analysis of the cell cycle due to spectral issues [9,10,11]. This study has employed a novel correction algorithm to remove the effects of these artefacts and reveal true absorption spectra. This is supported by ToF-SIMS data, which has allowed for further chemical characterisation of each cycle phase. Generally, in both techniques, an increase in cellular constituents is observed as the cell progresses through the cell cycle. Furthermore, ToF-SIMS data has allowed for the tentative identification of some of the chemical species responsible for the differences between each cycle phase. For example, despite large error bars, G2 phase can be characterised by a general increase in lipid signal and S phase by a slight general increase in certain amino acids and cholesterol. Clearly, in this case, such conclusions can only be treated as qualitative. This analysis would benefit from further investigation with a much larger sample set to be statistically more robust.

References

[1] T.C. Hamilton, R.C. Young and R.F. Ozols. *Seminars in Oncology* 11 (1984) p285-298

[2] C.Y. Yang, L.Y. Huang, T.L. Shen and J.A. Yeh. *European Cells and Materials* 20 (2010) p415-430

[3] P. Du, G. Stolovitzky, P. Horvatovich, R. Bischoff, J. Lim and F. Suits. *Bioinformatics* 24 (2008) p1070-1077

[4] M.R. Keenan and P.G. Kotula. *Surface and Interface Analysis* 36 (2004) p203-212

[5] R.M. Jarvis, D. Broadhurst, H.E. Johnson, N. O'Boyle and R. Goodacre. *Bioinformatics* 22(20) (2006) p2565-2566

[6] P. Bassan, H.J. Byrne, F. Bonnier, J. Lee, P. Dumas and P. Gardner. *Analyst* 134 (2009) p1586-1593

[7] Z. Movasaghi, S.Rehman, and I. Rehman. *Applied Spectroscopy Reviews* 43 (2008) p134-179

[8] K.J. McManus, V.L. Biron, R. Heit, D.A. Underhill and M.J. Hendzel. *The Journal of Biological Chemistry* 281 (2006) p8888-8897

[9] S. Boydston-White, T. Chernenko, A. Regina, M. Milikovic, C. Matthaus and M. Diem. *Vibrational spectroscopy*. 38 (2005) p169-177

[10] S. Boydston-White, M. Romeo, T. Chernenko, A. Regina, M. Milikovic and M. Diem. *Biochmica et biophysica acta*. (2006) 908-914

[11] H.N. Holman, M.C. Martin, E.A. Blakely, K. Bjornstad and W.R. McKinney. *Biopolymers (biospectroscopy)*. 57 (2000) p329-335

[12] J. Jackowski. *The Journal of Biological Chemistry* 269 (1994) p3858-3867

[13] M.D. Siperstein. *The Journal of Lipid Research* 25 (1984) p1462-1468

Chapter 6: FTIR and ToF-SIMS based characterisation of a novel anticancer agent.

As discussed in section 2.1.1, attempts have been made to use FTIR to investigate the mechanisms, by which, novel chemotherapeutic agents work [1,2,3,4]. The fruits of which were detecting changes in the global chemistry of the cell attributed to the cycle phase, in which, the drug had caused arrest [4]. However, spectra were averaged thus losing information regarding the chemistry of individual cells. Recently, a similar spectroscopic based investigation into the mechanisms of a novel di-gold organometallic complex [1,3-$(Ph_3PAu)_2$-C_6H_4] (KF0101) used synchrotron-based FTIR coupled with PCA to compare the chemical signatures of the drug with a series of existing anti-cancer agents [5]. Although this investigation hinted at signatures of the cell cycle, it did not take this any further.

The data presented in the previous chapter not only distinguishes between the various cycle phases, but also shows subtle differences between the chemistry of FACS sorted cells and those treated with anticancer drugs. This would suggest it is possible to provide information as to the drugs influence on the cell cycle in conjunction with the chemical changes specific to that drug. The following chapter will use FTIR and ToF-SIMS combined with DFA to investigate the extent to which KF0101 can be characterised using previous knowledge of the cell growth cycle.

6.1 Experimental

For methodologies relating to the initial characterisation of the cell cycle see chapter 5.1. KF0101 treated ovarian cancer cells were also analysed using the same conditions.

6.1.1 Preparation of KF0101 treated cells

Cells from the A2780 human epithelial cell line were seeded on CaF_2 in sterile plastic 6 well plates for Infrared analysis (Fisher Scientific, UK). Due to the incompatibility of silicon wafer with cell growth, samples were seeded in $25cm^3$ sterile plastic flasks for SIMS analysis. After culturing (37^0C, 5% CO_2, in air) in media (RPMI-1640, 10% FCS and 2mM L-glutamine, Sigma Aldrich, UK) to around 60% confluency, the cells in flasks were then treated with KF0101 (50nM in DMSO) for 24 hours. The cells were then fixed in ethanol (70%) and cytospun onto CaF_2 for FTIR analysis or silicon wafer for ToF-SIMS analysis. All cells prepared in this way will be referred to as KF0101 treated treated throughout the discussion.

6.2 Results and discussion

6.1.1 FTIR analysis

Combining the FACS sorted and drug treated data from chapter 5 has provided a framework into which the KF0101 data can be projected (figure 6.1). Figure 6.1 shows a DFA scores plot for DF1 VS 2 of the FACS sorted and drug treated data together using 28 principal components. This plot clearly shows the differences between the cycle phases along the Y axis (DF 2) and importantly the influences of the drug along the X axis (DF 1). It is unsurprising that the two G1 phases are close to each other as they were blocked using serum starvation, and therefore, should be very chemically similar to the FACS sorted cells. Their small differences may be due to the presence of propidium iodide, however there were no spectral indications of this molecule.

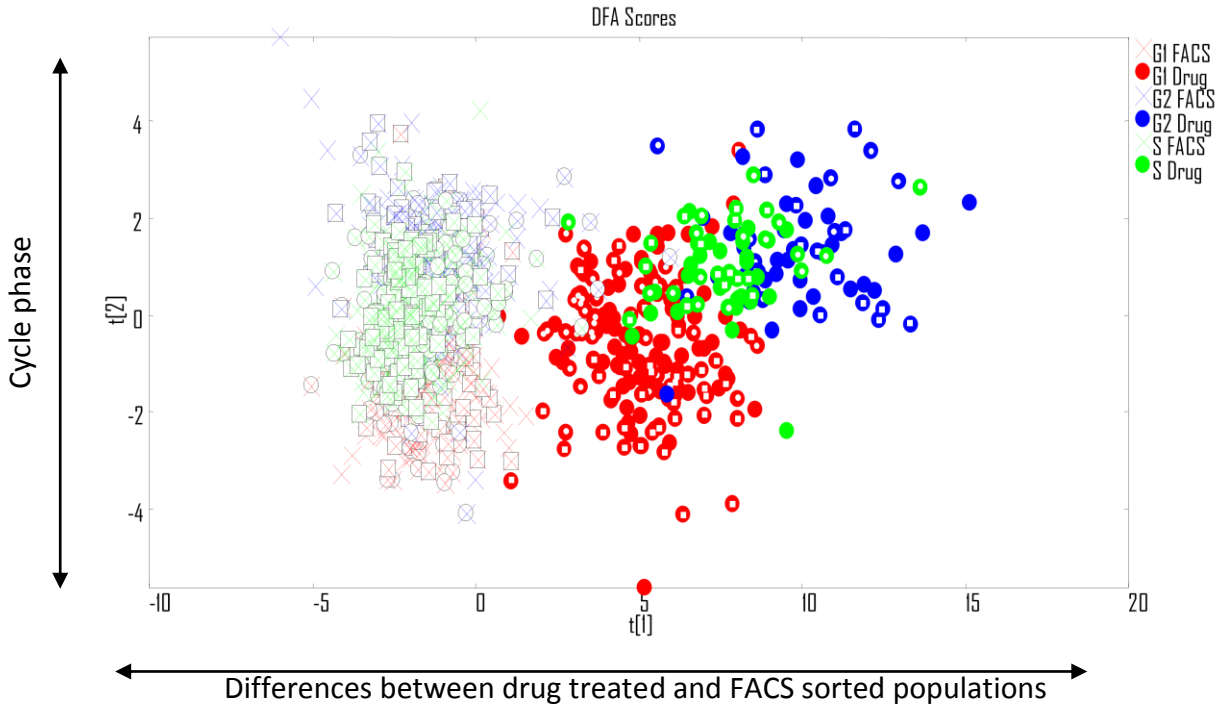

Figure 6.1. DFA scores plot of FACS sorted (points circled are the test set); and Drug treated data (points with a white centre are the test set).

The KF0101 data (labelled Au, figure 6.2) was then combined with the data in figure 6.1 to give figure 6.2 using 32 principal components. Again, despite a tightening of the FACS sorted cluster, the same pattern as before is observed. Interestingly, the KF0101 data appears to be clustering with the data from cells blocked into S-phase of the cell cycle using methotrexate.

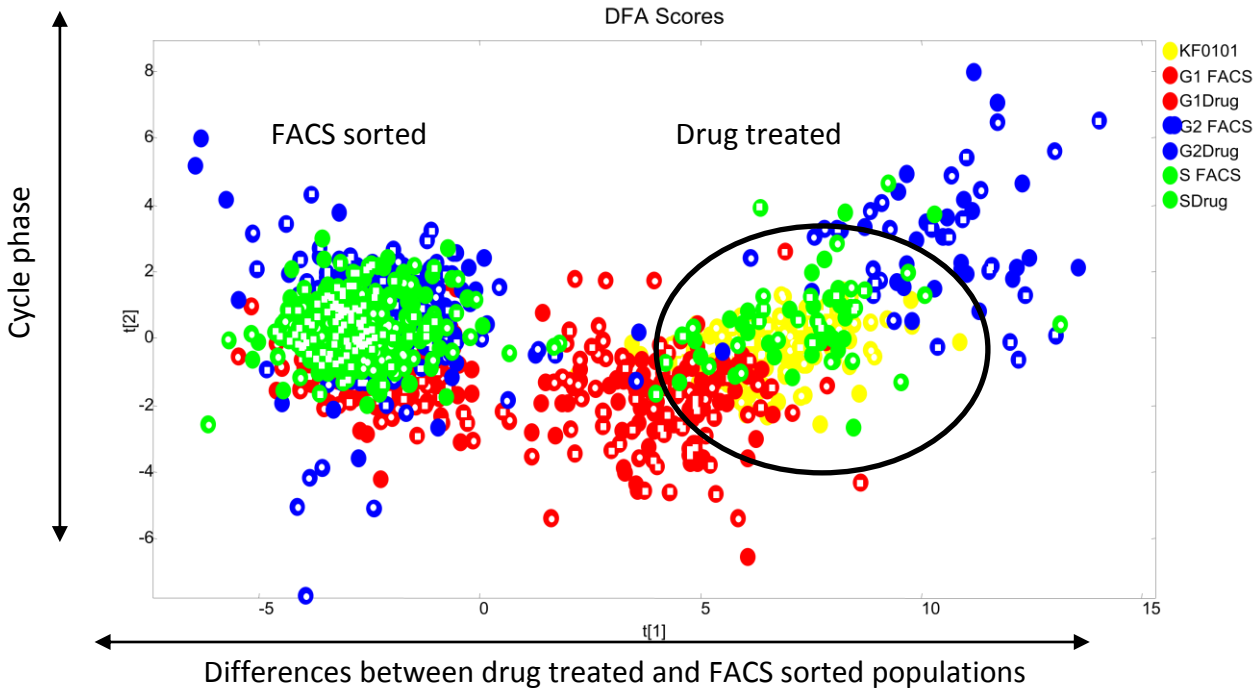

Figure 6.2. DFA scores plot of FACS sorted and drug treated data including KF0101 (Au). Points with a white centre are the test set.

Clearly, figure 6.2 suggests that cells treated with KF0101 are arrested in S-phase of the cell cycle. Examination of the overlaid average spectra and discriminant function loadings plot for S phase of the FACS sorted phase versus KF0101 shows a number of interesting differences (figures 6.3 and 6.4). The most significant difference observed in figure 6.4 is seen in the amide I region of the spectra (1640 cm^{-1}) and (1670 cm^{-1}). Although this is less obvious in figure 6.3, it is clear from the loadings plot that it is important. Interestingly, changes in this area are often associated with changes in the structure of proteins, more specifically beta sheets. Changes in the signal from membrane components such as phospholipid phosphate (1055 cm^{-1}), CH_2 groups of fatty acids and lipids (1444 cm^{-1} and 2925 cm^{-1}) and cholesterol (2800-3500 cm^{-1}) are also clear. Furthermore, the KF0101 treated cells seem to show a drop in signal associated with RNA (~1117 cm^{-1}) - seen in both figures 6.3 and 6.4 - and a reduction in the intensity of the amide II band (1500-1580 cm^{-1}).

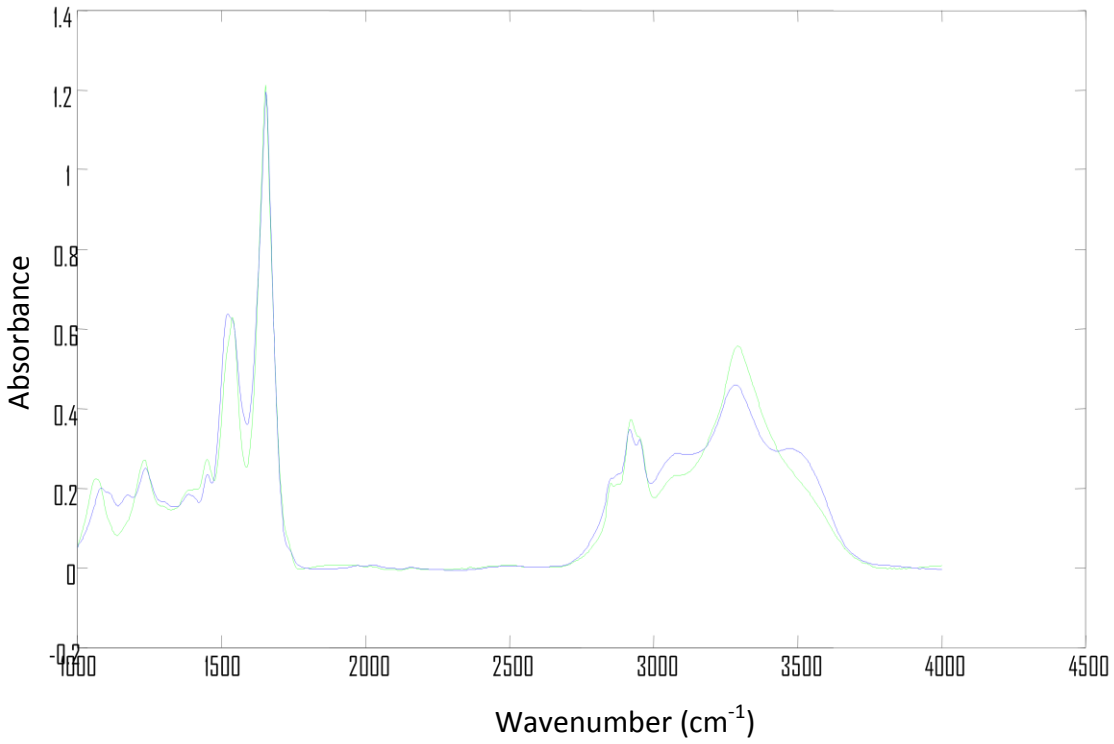

Figure 6.3. Overlay of KF0101 (green) and S-phase (blue) spectra.

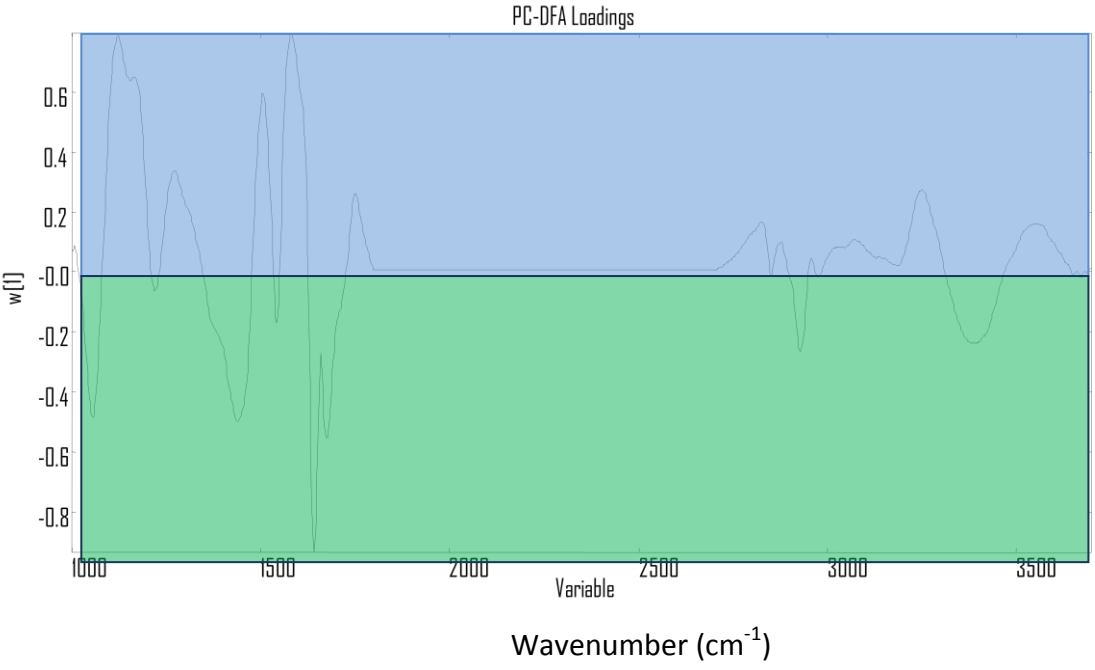

Figure 6.4. Loadings plot for KF0101 (green) Vs FACS sorted S-phase (blue).

6.1.1 ToF-SIMS analysis

As with the previous section the ToF-SIMS data from FACS sorted and drug treated cell lines was combined using 17 and 16 principal components for positive and negative data respectively (figures 6.5 and 6.6).

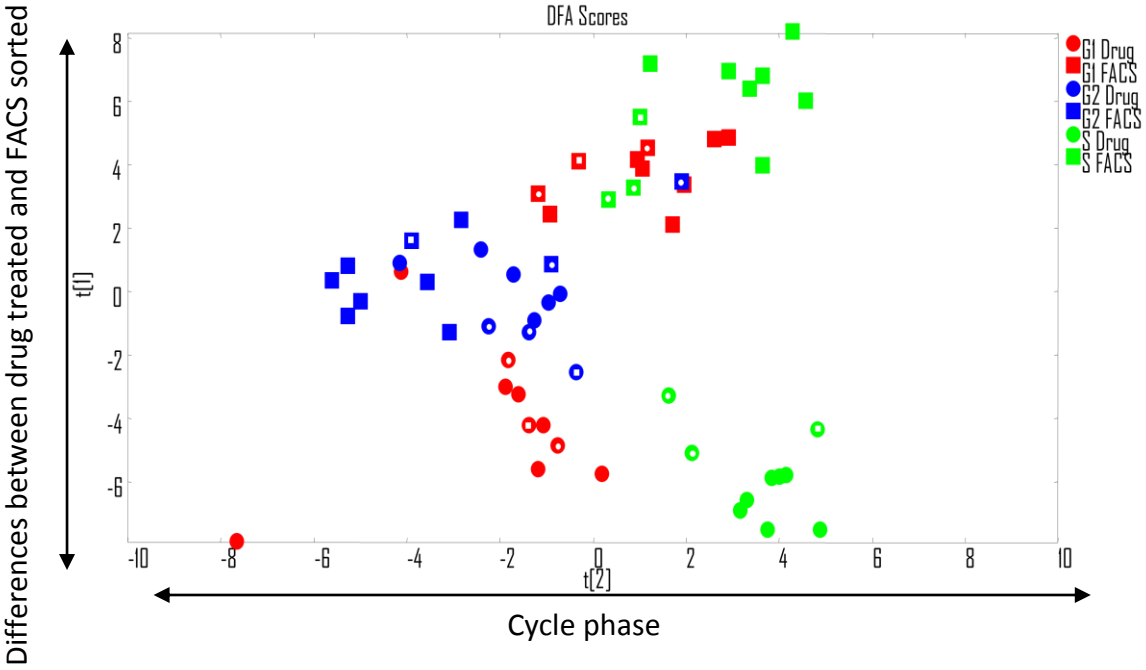

Figure 6.5. DFA scores plot for positive FACS sorted and drug treated data. Points with a white centre are the test set.

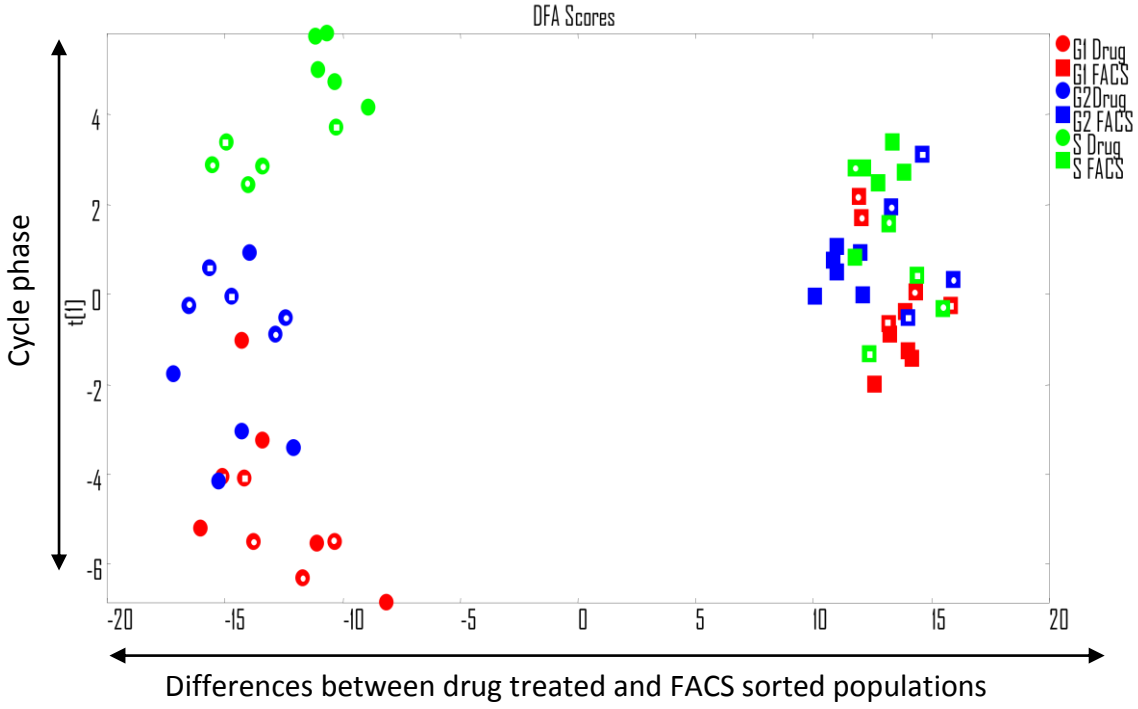

Figure 6.6. DFA scores plot for negative FACS sorted and drug treated data. Points with a white centre are the test set.

Data for the KF0101 treated cells was then included to give figures 6.7 and 6.8. Again, despite a tightening of the FACS sorted group, it is clear that the KF0101 data is grouping with data for cells blocked in S-phase using methotrexate. Furthermore, this pattern is the same for both positive and negative data.

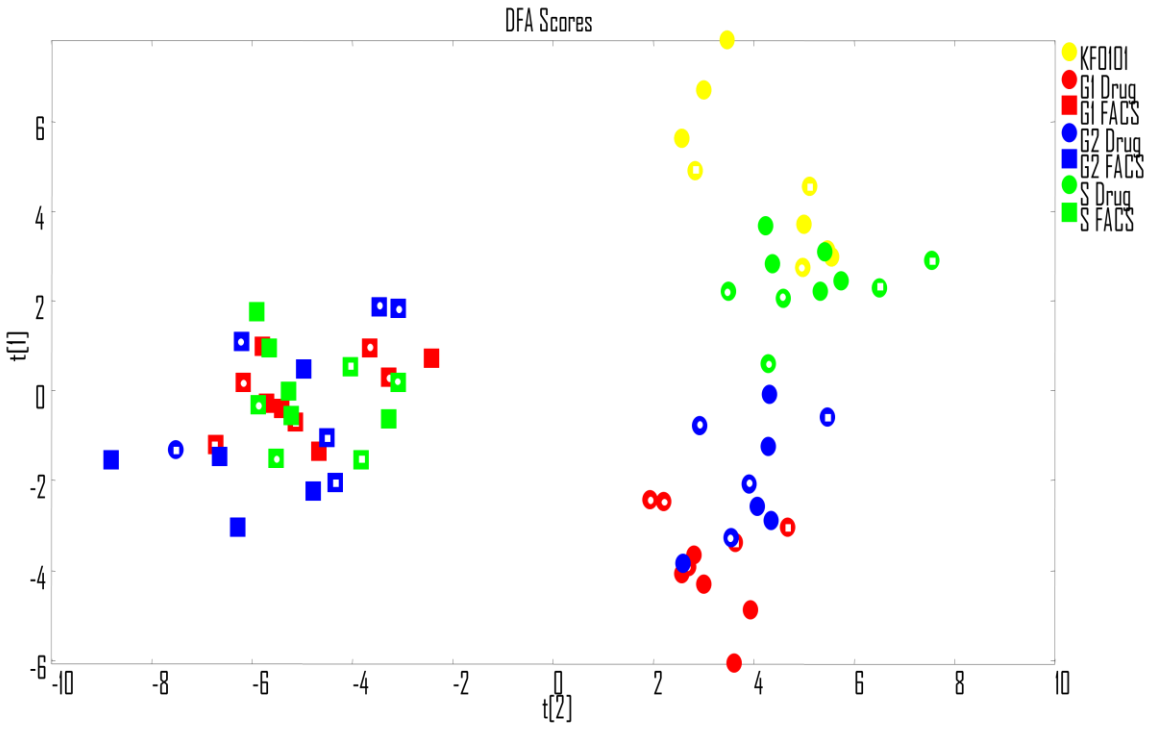

Figure 6.7. DFA scores plot for positive FACS sorted and drug treated cells using 9 principal components. Points with a white centre are the test set.

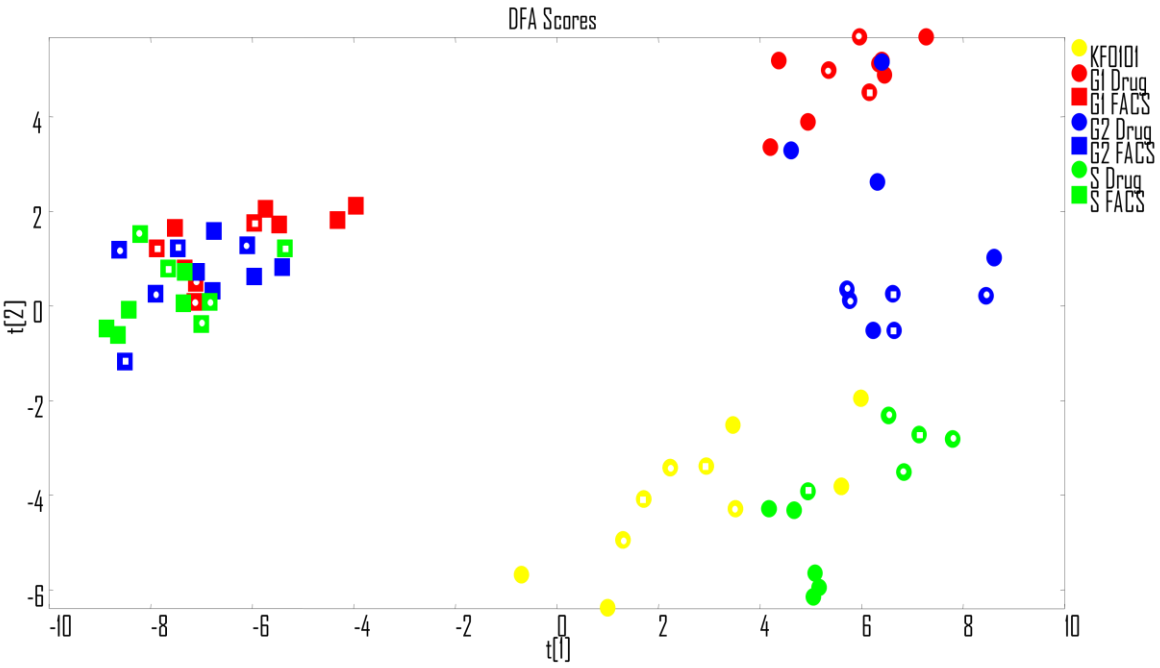

Figure 6.8. DFA scores plot for negative FACS sorted and drug treated cells using 14 principal components. Points with a white centre are the test set.

S-phase data for the FACS sorted cells was then directly compared to that of KF0101 to further identify the chemical influences of the drug (figures 6.9 and 6.10).

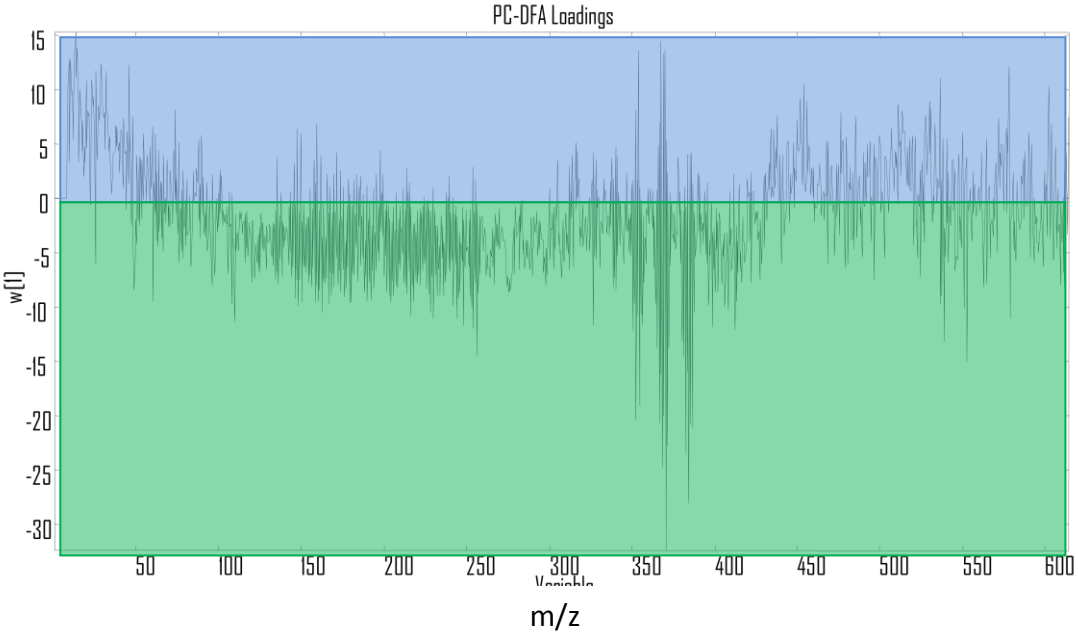

Figure 6.9. DFA loadings plot for positive S-phase FACS (blue) and KF0101 (green) data.

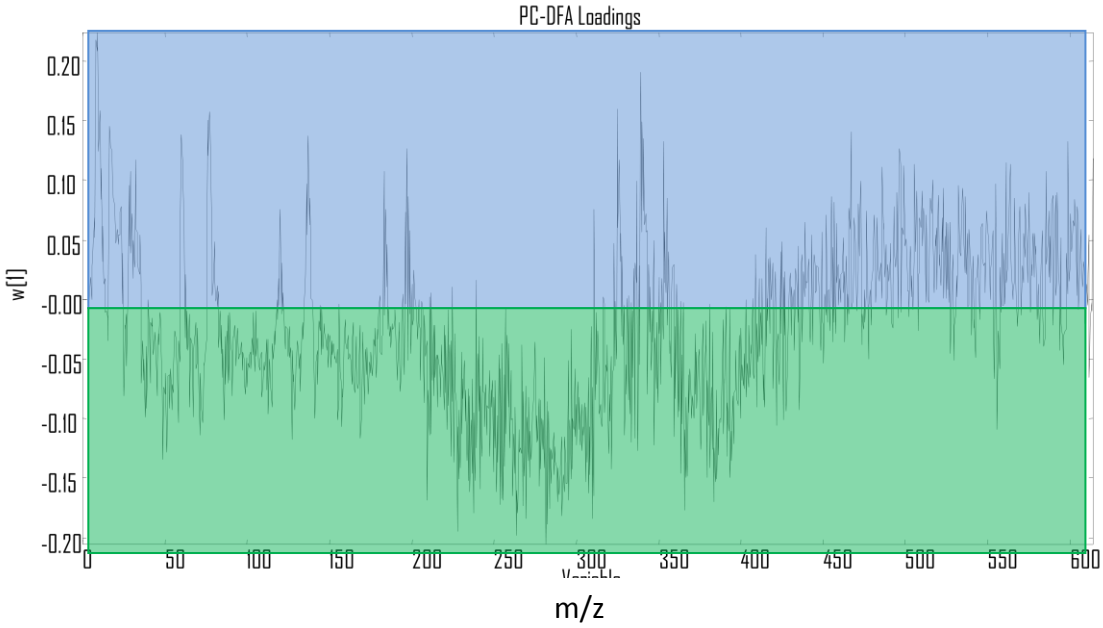

Figure 6.10. DFA loadings plot for negative S-phase FACS (blue) and KF0101 (green) data.

As in chapter 5 the differences highlighted by the loadings plots are complex. Previously, the cell cycle was characterised through a series of peaks, most of which are also present in figures 6.9 and 6.10. To observe the drugs effect on the natural changes that occur during proliferation, relative ion yields for these masses were calculated for KF0101 and compared to those for drug treated and FACS sorted cells in S-phase (figures 6.11, 6.12, 6.13 and 6.14). Interestingly, there were no clear signatures for the drug present, however this is not surprising as the drug is probably located within the cells in very low concentrations and SIMS is a surface analysis technique. This is compounded further by the fact that in SIMS typically <1% of the material sputtered off the cell is ionised.

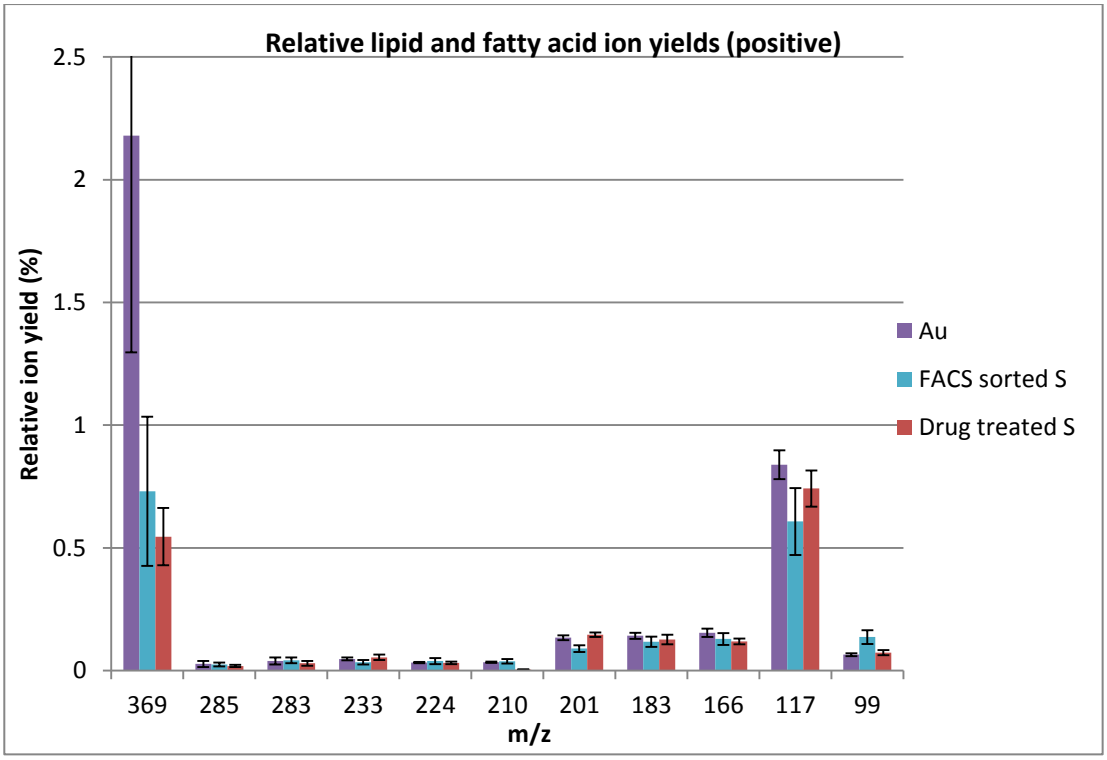

Figure 6.11. Positive lipid and fatty acid relative ion yields. The data are presented as means ± s.d (n=10).

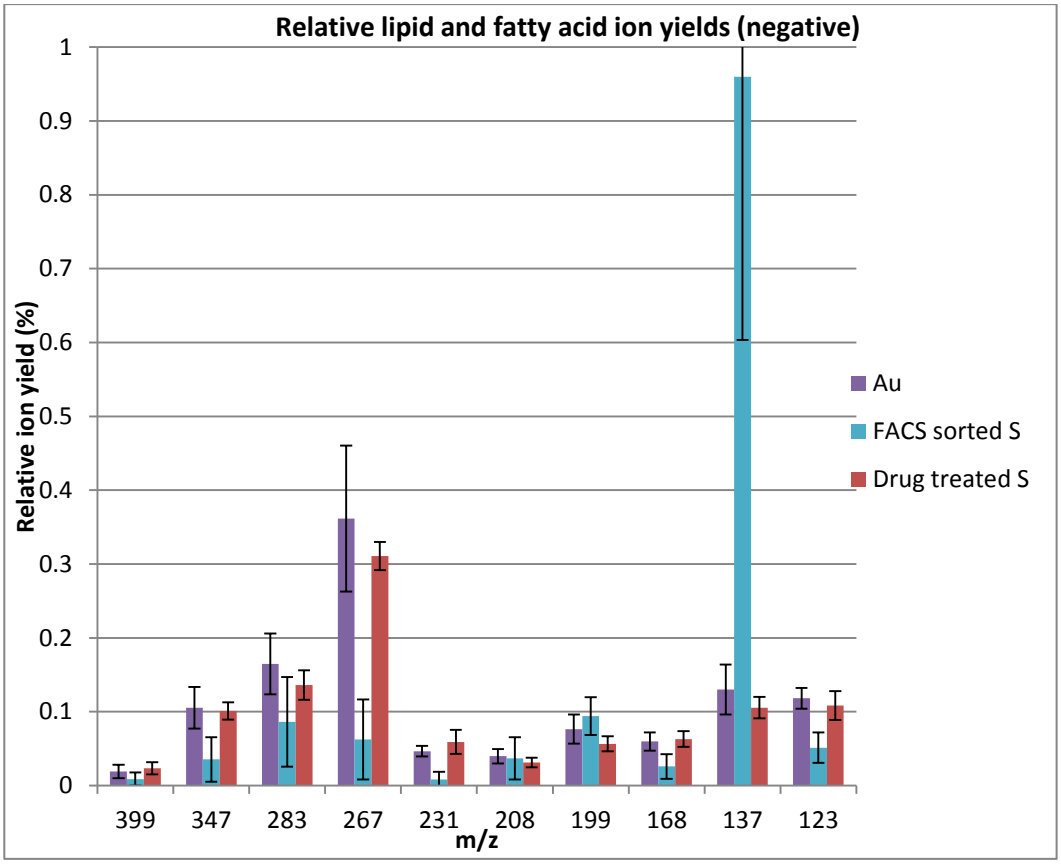

Figure 6.12. Negative lipid and fatty acid relative ion yields. The data are presented as means ± s.d (n=10).

The positive relative ion yields for the three groups appear to be very similar, apart for an apparent large increase in yield of cholesterol (m/z 369). The negative data suggests a massive drop in DPPC (m/z 137), however the opposite is seen for the other DPPC fragment at m/z 123. Again this could be due to matrix effects, induced by the drug, or chemical changes brought about by its action as these could have different effects on positive and negative ion generation. Interestingly, in both figures 6.11 and 6.12, the lipid and fatty acid yields (positive m/z 369, 201, 183, 166, 177 and negative m/z 399, 347, 283, 267, 231, 168, 123) of the KF0101 and drug treated data appear to be generally higher than those for the FACS sorted cells.

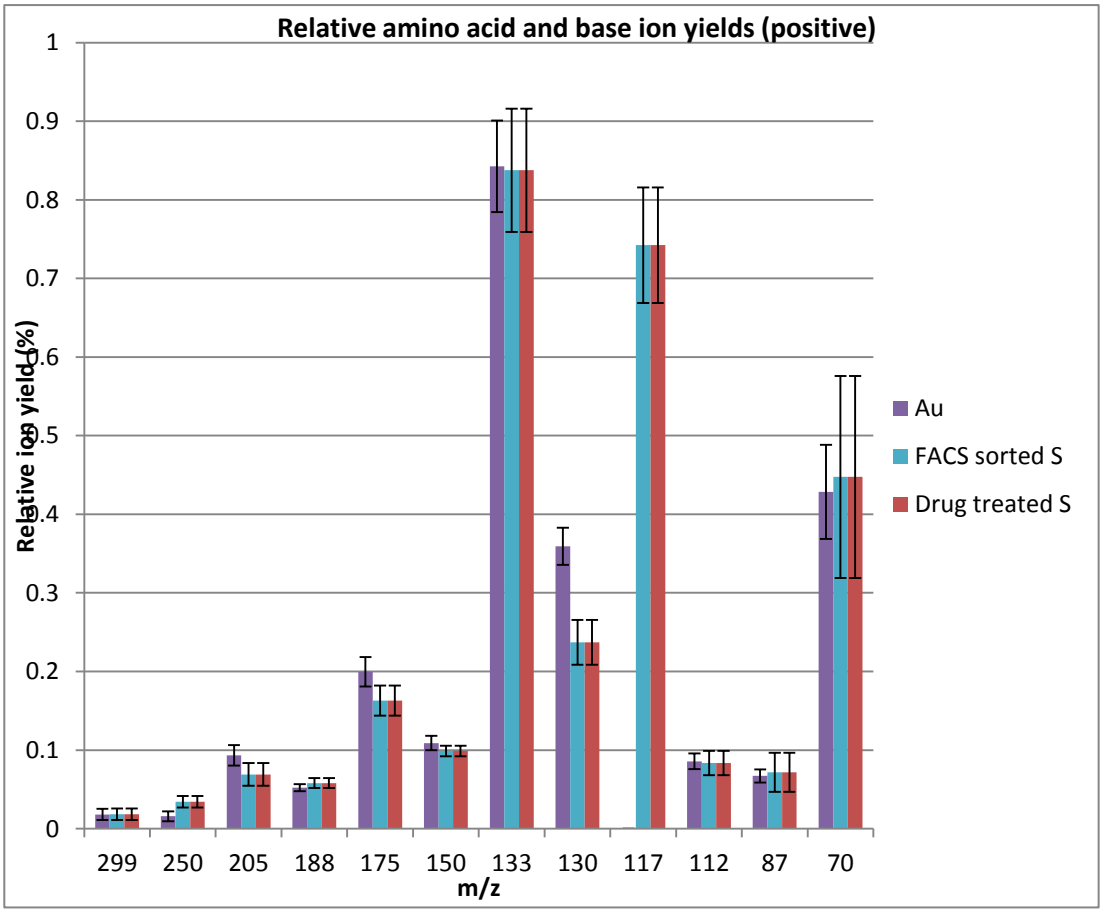

Figure 6.13. Positive amino acid and base relative ion yields. The data are presented as means ± s.d (n=10).

The majority of the amino acid and base yields for the positive data (figure 6.13) appear to be relatively similar. However, the yields of certain amino acids and bases (m/z 131, 148, 173 and 203) are much lower for the KF0101 data than for the other two sample sets (figure 6.14). The other significant difference is the complete lack of any signal from m/z 117 in positive ion mode and a lower yield of m/z 250 both related to the nucleoside cytidine, which is found in RNA. This is reflected in figure 6.14 for the negative data as a lower yield of m/z 226. As discussed earlier a change in RNA content was also observed using FTIR so it is likely to be an effect of the KF0101 drug.

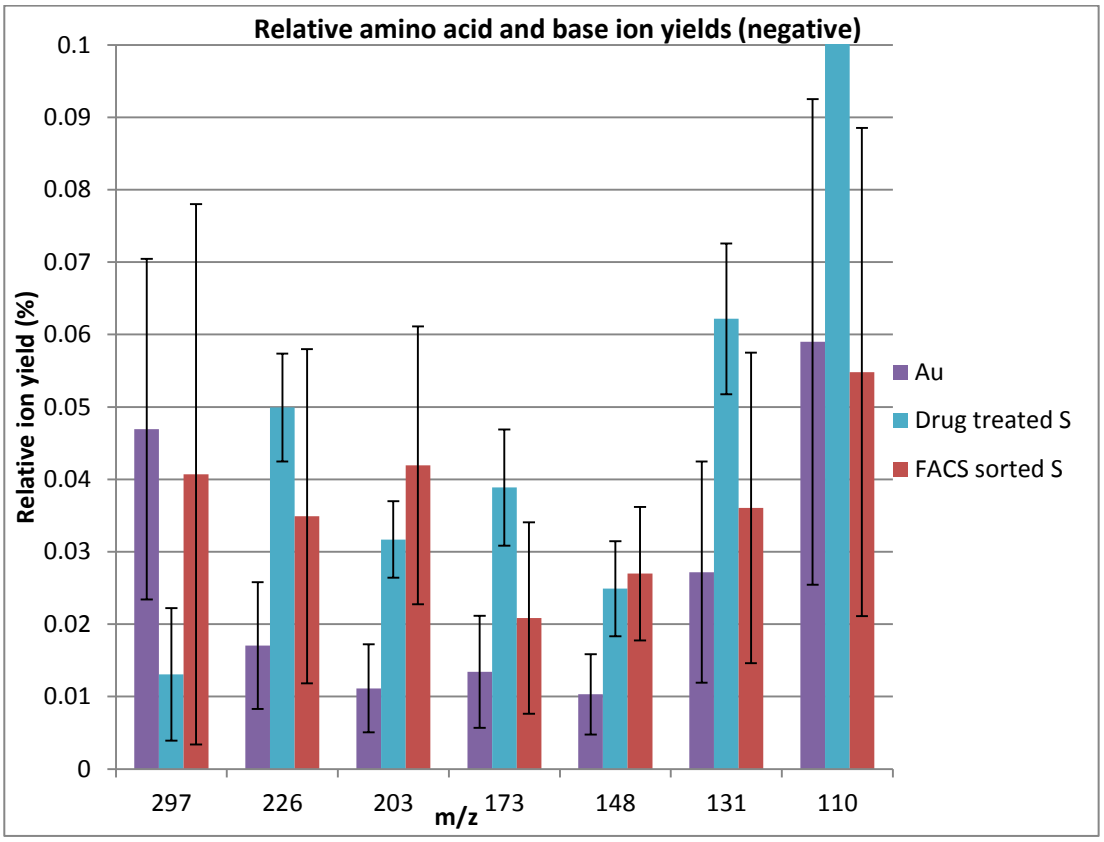

Figure 6.14. Negative amino acid and base relative ion yields. The data are presented as means ± s.d (n=10).

6.2 Conclusions

In summary, both FTIR and ToF-SIMS showed clearly the KF0101 drug was acting in S-phase of the cell cycle. Furthermore, it was causing cells to produce similar chemical responses to those treated with methotrexate. To attempt to investigate this further the KF0101 treated cells were directly compared to the

FACS sorted cells in S-phase. Both ToF-SIMS and FTIR data suggests the drug has an influence on RNA and membrane structure.

The data presented in this chapter shows that it is possible to characterise a novel anticancer agent using prior knowledge of the cell cycle for the cell line in question. Inferences have been made as to the chemical influences of the drug however this is purely a proof of concept study and although successful, it is clear further investigation is warranted. Finally, the methodology used in this chapter is not intended to fully describe the mode of action of drug. It is hoped that it may become more of a guide through which further investigations can be targeted, thus saving time and resources.

References

[1] J. Sule-Suso, D. Skingsley, G.D. Sockalingum *et al. Vibrational spectroscopy.* 38 (2005) p179-184

[2] R. Gasper, J. Dewelle, R. Kiss, T. Mijatovic and E. Goormaghtigh. *Biochimica et biophysica acta*. 1788 (2009) p1263-1270

[3]R. Gasper, T. Mijatovic, R. Kiss, E. Goormaghtigh. *Spectroscopy*. 24 (2010) p45-49

[4] F. Draux, P. Jeanesson, C. Gobinet, J. Sule-Suso, J. Pijanka, C. Sandt, P. Dumas, M. Manfait and G.D. Sockalingum. *Analytical and Bioanalytical Chemistry.* 395 (2009) p2293-2301

[5] K.R. Flower, I. Khalifa, P. Bassan, D. Demoulin, E. Jackson, N. P. Lockyer, A. T. McGown, P. Miles, L. Vaccari and Peter Gardner. *Analyst*. In press.

Chapter 7: Final conclusions and future works

The research carried out in this thesis has demonstrated the efficacy of a combination of FTIR and TOF-SIMS to analyse single cancer cells. This robust approach has provided important biochemical information about model cancer cells.

This final chapter will address each of the results chapters in the light of the aims and objectives set out initially. Any limitations of the investigations carried out will be identified and possible future work will be described.

7.1 A systematic evaluation of cytospinning as a novel technique for the preparation of cells for ToF-SIMS analysis

As previously discussed, biological SIMS, until now, has mainly focussed on cell cultures grown on SIMS compatible substrates [e.g. 1] or on tissue sections [e.g. 2]. Due to concerns as to the effects of growing cells on these substrates [3,4] a methodology was sought to bypass these issues. Cytospinning, was investigated and validated as a potential alternative to existing protocols for the preparation of biological cells for ToF-SIMS analysis. Furthermore, for those samples not amenable to cytospinning, washing with ammonium formate was shown to be beneficial. This wash was found to be slightly less important for cytospun samples as most of the extracellular fluid and associated contaminants such as Na^+, is removed during the cytospinning step. Most importantly, the cytospinning methodology developed is directly compatible with other complementary techniques, such as FTIR. Moreover, as there is no need to culture cells on substrates, non-adherent cell lines are now amenable to analysis.

A novel future application of cytospinning would be to investigate non-adherent cancer cell lines, for example the K562 myelogenous leukaemia cell line [5]. These cells grow naturally in suspension so there is no need for the use of trypsin to remove them from their growth flask. This again is a further step towards analysing cells as close to their natural state as possible.

7.2 The combined application of ToF-SIMS and FTIR in the spectral investigation of the cancer cell cycle

After developing a suitable preparatory methodology FTIR and ToF-SIMS were used to examine the cell cycle. The molecule specific information from ToF-SIMS supported by the global information from FTIR, in conjunction with multivariate statistics has provided a novel, robust method for investigating the chemistry of the cell cycle. A general increase in the levels of certain cellular constituents prior to mitosis has been detected. Attempts were made to tentatively identify certain peaks found in SIMS; however, this is difficult due to the possibility of several parent ions. This would benefit from further investigation with increased mass resolution or, possibly, MS/MS. Previous work in this area has only studied a small part of the full FTIR spectral range due to problems with spectral artefacts [6,7,8]. This investigation was more robust as the majority of results seen in FTIR were backed up by SIMS data. This has also validated the use of the new correction algorithm for such a study. It should be noted, however, that although FACS sorting was a high throughput readily available technique, it is not the perfect technique for separating cells due to the use of propidium iodide and an RNAse enzyme used to digest extranuclear RNA. No easily identifiable spectral features were detected from these chemicals but they may have caused other subtle chemical changes. The best method would be to use centrifugal elutriation as no chemicals are required to aid the separation [9].

Overall, the results indicate that FTIR, and importantly, ToF-SIMS are sensitive enough to detect global (FTIR) and surface (ToF-SIMS) biochemical changes induced by the cell cycle. This suggests that the cell cycle could influence the classification of different cell types and should be taken into consideration in such an investigation. As discussed earlier there has, until now, been no SIMS investigations into the cell cycle and very little is known about the changes in the cell surface chemistry during cell proliferation. Furthermore, as the cell membrane is the first point of contact for the cell, and anticancer drugs mostly work by inhibiting cellular proliferation, it is important to understand this chemistry.

7.3 FTIR and ToF-SIMS based characterisation of a novel anticancer agent.

Characterising the cell cycle using FACS sorted and drug treated ovarian cancer cells produced results which showed interesting similarities and differences. It appeared that they were similar in terms of cycle phase, but different due to the chemical influence of the drug. Using this data as the training set for discriminant function analysis allowed for the identification of the cycle phase, in which, a novel, gold-based anticancer agent was causing arrest. No spectral signatures of the drug were seen so it was not possible to comment upon the drugs localisation.

Whilst it was beyond the scope of this investigation to completely elucidate the mechanisms of the novel anticancer agent, it is hoped the information provided has formed an important starting point for more targeted investigations. For example, it is clear cells treated with the drug are arrested in S-phase therefore possibly ruling out any biological processes occurring in G2 and M phase. Future work into this area could use these methods to characterise the spectral signatures for many different types of anticancer agents e.g. alkylating agents, anti-metabolites, plant alkaloids and terpenoids, topoisomerase inhibitors and antineoplastic agents etc. This would then start to produce a library of signatures specific to each drug type, again providing a more detailed starting point for other investigations into drug mechanisms. To extend this further, to aid the identification of drug actions, the effects of different dosing levels of the drug could be investigated. Cells could be doped at the IC_{30}, IC_{50} and IC_{70} values for a particular drug. These IC values refer to the concentration of the drug, at which cell growth is inhibited by 30% (IC_{30}), 50% (IC_{50}) and 70% (IC_{70}).

7.4 Future work

Another possible use of the methodologies developed could be to look at the physiological differences between renal cancer cell lines. Preliminary work on three cell lines derived from primary renal resections (2245R, 2246R and 2247R) showed promise but due to time constraints was not taken further. These cell

lines are interesting as one of them (2247R) has a more aggressive phenotype than the others. This cell line proliferates at a much greater rate and previous investigations have characterised certain differences thought to be concomitant with increased aggression [10]. However, the differences reported may just be due to the natural differences between cell types. Continuing along the theme of cell proliferation it would be interesting to characterise the chemistry of the cell cycle for each of the cell lines, using the previously described method. In doing so, it may be possible to discover a larger range of biomarkers specific for each stage of the cell cycle. Furthermore, as the cell membrane is the first point of contact for the cell, a good understanding of this chemistry through combined SIMS and FTIR analysis will also provide vital information on membrane changes that facilitate increased aggression and mobility. It is also possible that this type of information could aid future anticancer drug development.

7.5 Outlook

ToF-SIMS and FTIR are clearly capable of exploring exciting new areas of cell biology. The unique advantages of each technique combined allow for more robust analyses than would be possible alone. Having reviewed the literature for both techniques it is clear, however, that FTIR is much further ahead in terms of becoming a clinically relevant technique than ToF-SIMS. This is almost certainly because it is less complex and more high throughput than SIMS, which is still in its infancy in comparison. However, it should be reiterated that SIMS has the potential for far superior specificity. Despite this gap, some studies involving the two techniques alone are already describing healthy and diseased states, however, it is personally believed that more investigations into the fundamental aspects of cellular analysis are required and spectra for “normal” cells must first be completely understood.

Finally, these techniques combined with powerful multivariate statistics and well-designed methodologies will no doubt eventually form an important role in - the increasingly popular - evidence-based medicine and hopefully will help to close the “bench to bedside” gap.

References

[1] M.J. Baker, M.D. Brown, E. Gazi, N.W. Clarke, J.C. Vickerman and N.P. Lockyer. *The analyst.* 133 (2008) p1-6

[2] E. Gazi, J. Dwyer, N. Lockyer, P. Gardner, J.C. Vickerman, J. Miyan, C.A. Hart, M. Brown, J.H. Shanks and N. Clarke. *Faraday discussions*. 126 (2004) p41-59

[3] B.G. Keselowsky, D.M. Collard and A.J. Garcia. *Applied biological sciences*. 102 (2005) p5953-5957

[4] A.D. Meade, F.M. Lyng, P. Knief and H.J. Byrne. *Analytical and bioanalytical chemistry*. 387 (2007) p1717-1728

[5] E.Klein, H. Ben-Bassat, H. Neumann, P. Ralph, J. Zeuthen, A. Polliack and F. Vanky. *International Journal of Cancer* 18(4) (1976) p421-431

[6] S. Boydston-White, T. Chernenko, A. Regina, M. Milikovic, C. Matthaus and M. Diem. *Vibrational spectroscopy*. 38 (2005) p169-177

[7] S. Boydston-White, M. Romeo, T. Chernenko, A. Regina, M. Milikovic and M. Diem. *Biochmica et biophysica acta*. (2006) 908-914

[8] H.N. Holman, M.C. Martin, E.A. Blakely, K. Bjornstad and W.R. McKinney. *Biopolymers (biospectroscopy)*. 57 (2000) p329-335

[9] D. Gillespie and C. Henriques. *Reviews and protocols in DT40 research.* (2006) p359-361

[10] C.Hughes, P.Bassan, M.D. Brown, R.D. Snook, N. W. Clarke and P. Gardner. (2010) *Unpublished*.

Appendices

1. PC-DFA loadings plots for TOF-SIMS

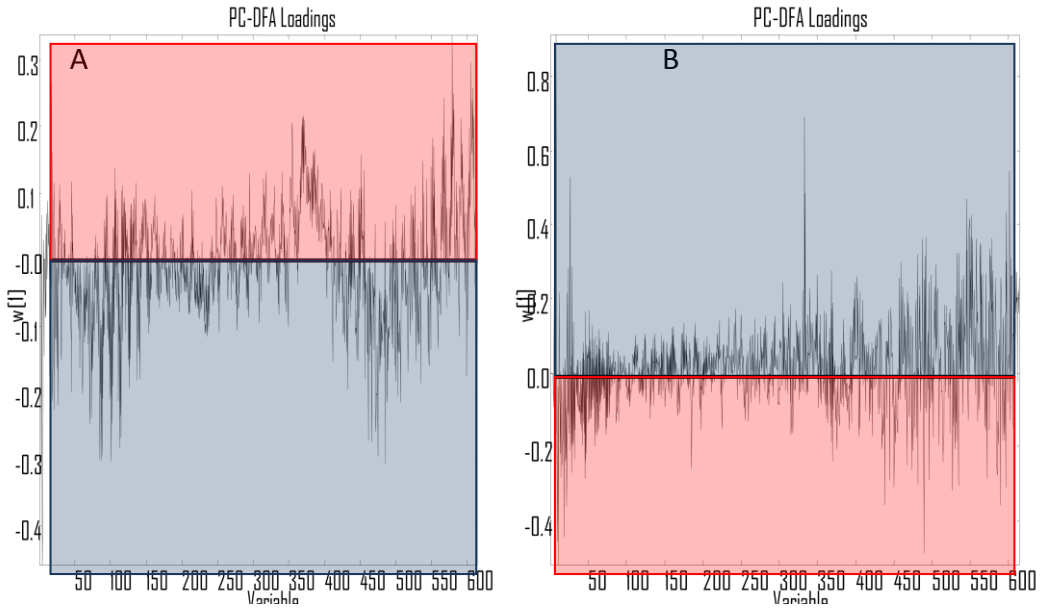

Figure A.1.1. Loadings plots for positive G1 (blue) and G2 (red) drug treated (A) and FACS (B) cells.

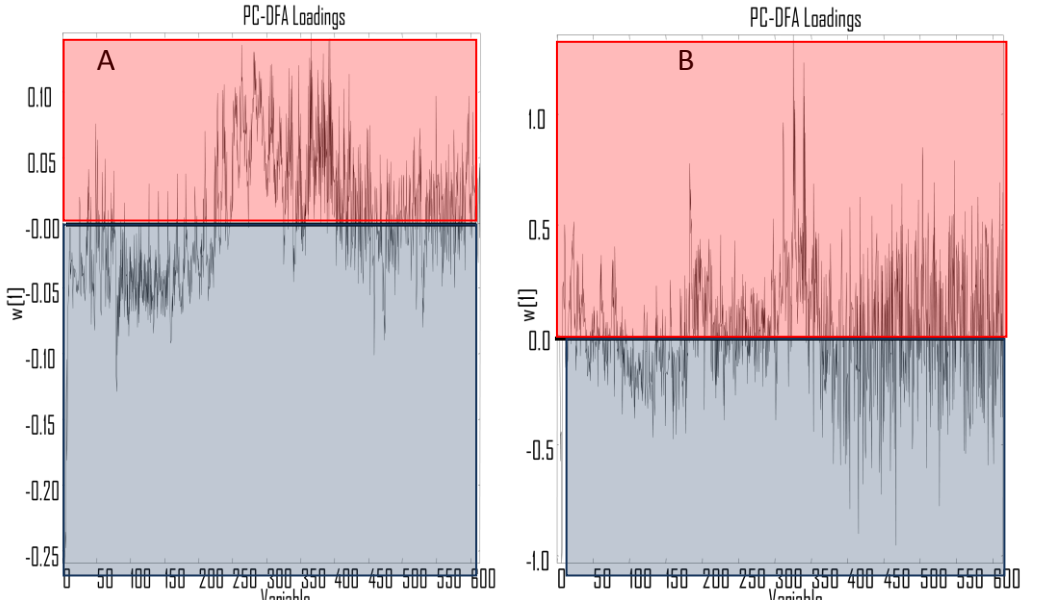

Figure A.1.2. Loadings plots for negative G1 (blue) and G2 (red) phases of drug treated (A) and FACS (B) cells.

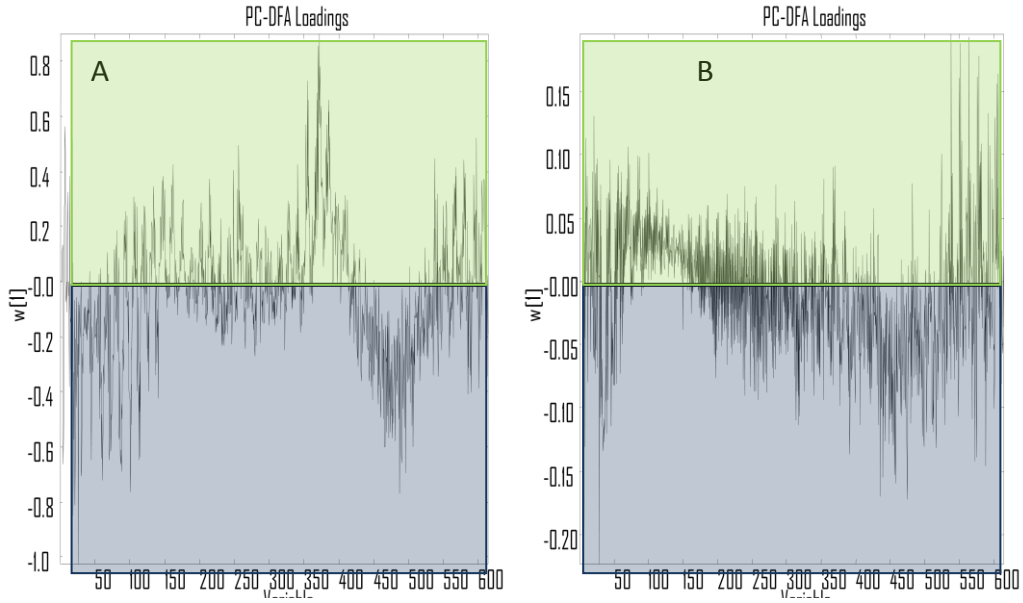

Figure A.1.3. Loadings plots for positive G1 (blue) and S (Green) phases of drug treated (A) and FACS (B) cells.

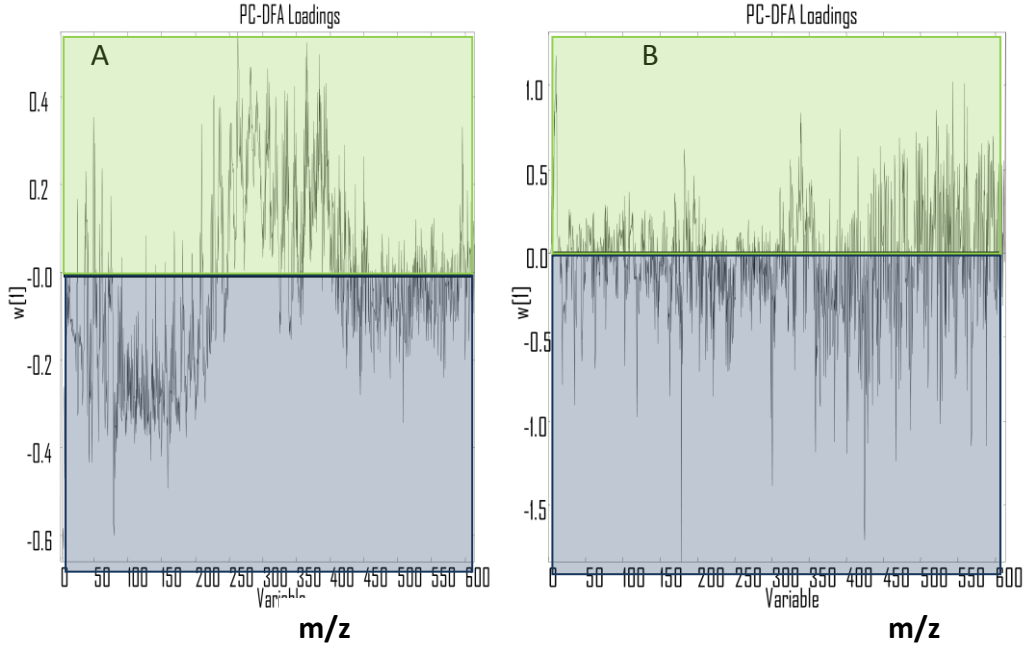

Figure A.1.4 Loadings plots for negative G1 (blue) and S (green) phases of drug treated (A) and FACS (B) cells.

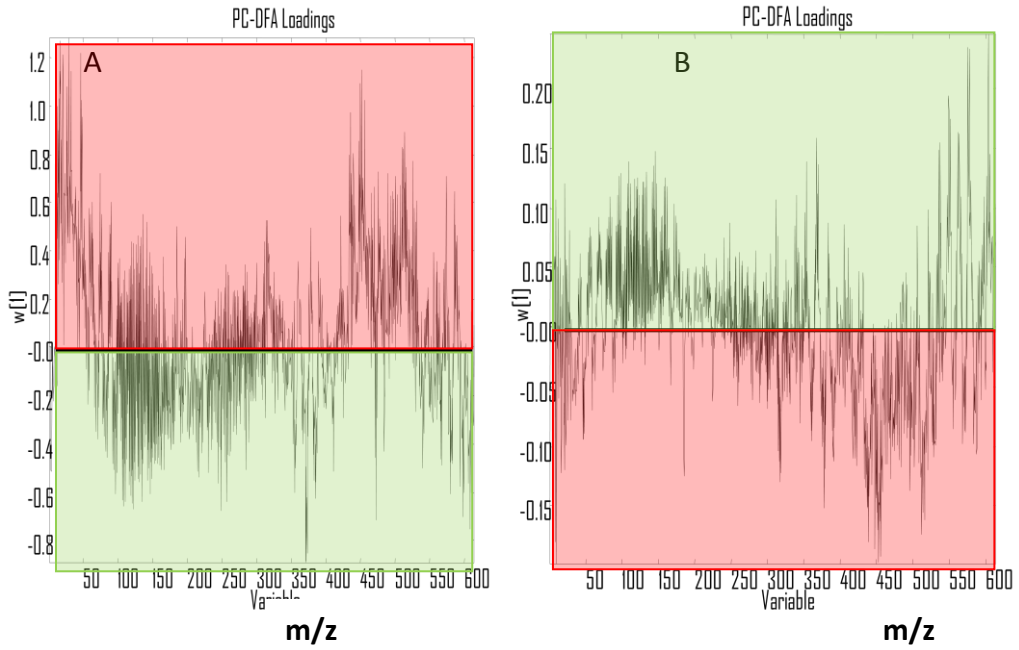

Figure A.1.5. Loadings plots for positive G2 (red) and S (green) phases of drug treated (A) and FACS (B) cells.

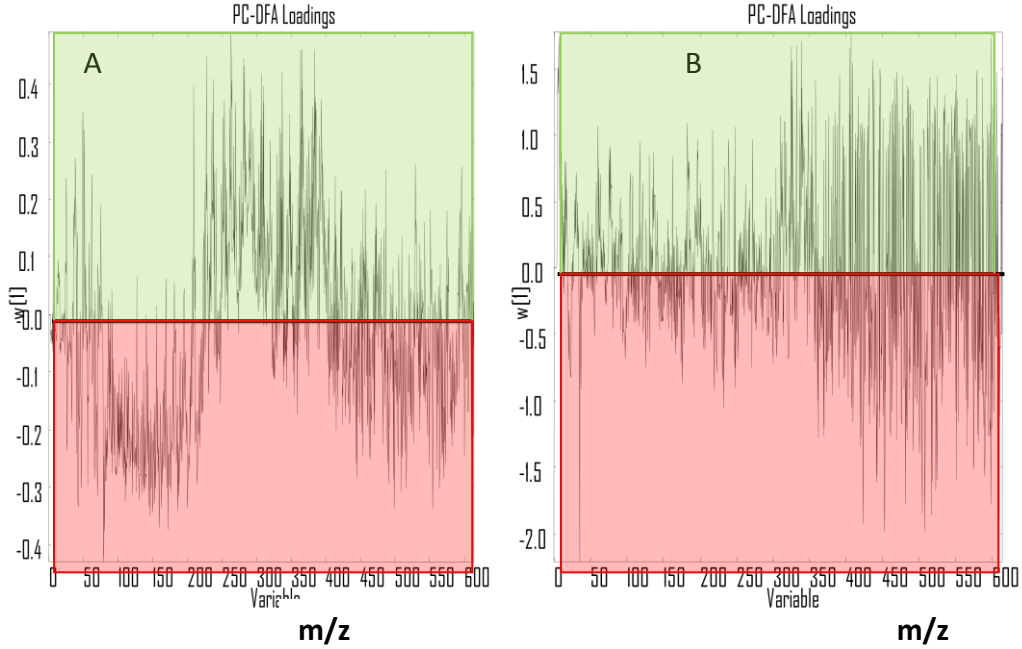

Figure A.1.6. Loadings plots for negative G2 (red) and S (green) phases of drug treated (A) and FACS (B) cells.